Aus dem Institut für Neuroanatomie
der Medizinischen Fakultät Mannheim
Zentrum für Biomedizin und Medizintechnik Mannheim
(Direktor: Prof. Dr. med. Christian Schultz)

Subcellular distribution of peroxisomes and endoplasmic reticulum in hippocampal neurons

Inauguraldissertation

zur Erlangung des

Doctor scientiarum humanarum (Dr. sc. hum)

der Medizinischen Fakultät Mannheim

der Ruprecht-Karls-Universität

zu Heidelberg

vorgelegt von

Yunhong Wang

aus

Anhui, China

2018

1 TABLE OF CONTENTS

2 LIST OF ABBREVIATIONS

3D	3 dimensional
ABCD1	ATP binding cassette subfamily D member 1
ACBD5	acyl-CoA binding domain containing protein 5
AcD	axon-carrying dendrite
AIS	axon initial segment
AP	action potential
ATP	adenosine triphosphate
BSA	bovine serum albumin
CA1	*Cornu Ammonis* area 1
CNS	central nervous system
CO	cisternal organelle
DLP1	dynamin-like protein 1
DRP1	dynamin-1-like protein
E18	embryonic day 18
SKL	serine-lysine-leucine sequence
ER	endoplasmic reticulum
ERGIC	ER-Golgi intermediate compartment
ERMES	ER-Mitochondria encounter structure
FFAT	two phenylalanines in an acidic tract
Fis 1	Fission factor 1

GABA	gamma-aminobutyric acid
GABA$_A$Rα2	gamma-aminobutyric acid receptor A containing α2 subunit
HBSS	Hanks' Balanced Salt Solution
Kv	voltage-gated potassium channel
MAP2	microtubule-associated protein 2
Mff	mitochondrial fission factor
MSP	major sperm protein domain
Myc-ACBD5	myc tagged acyl-CoA binding domain containing protein 5
Nav	voltage-gated sodium channel
NF186	neurofascin 186
PAEZ	pre-axonal exclusion zone
PBD	peroxisomal biogenesis disorder
PEI	polyethylenimine
Pen/Strep	penicillin/streptomycin
PFA	paraformaldehyde
PM	plasma membrane
PMP	peroxisomal membrane protein
PO	peroxisome
PTPIP51	protein tyrosine phosphatase interacting protein 51
PTS	peroxisome target signal
RER	rough endoplasmic reticulum

ROS	reactive oxygen species
rpm	rounds per minute
RT	room temperature
SA	spine apparatus
SER	smooth endoplasmic reticulum
SERCA	sarco/endoplasmic reticulum Ca^{2+}-ATPase
SP	synaptopodin
STED	Stimulated Emission Depletion
VAPB	vesicle-associated membrane proteins-associated protein B
VGAT	Vesicular GABA Transporter
VLCFAs	very-long-chain fatty acids
w/o	without
WT	wildtype

3   LIST OF FIGURES

4 INTRODUCTION

4. 1. General aspects of neuronal compartmentalization

4. 1. 1. Structural basis of neuronal polarity

Cellular morphological and functional asymmetry is crucial for the correctly developing and functioning of many polarized cells, among which neuron is the most polarized one. Neurons have to establish and maintain their unique morphological features to form complex functional neuronal networks through the lifetime for organisms. Such sophisticated neuronal polarity is constituted by many different neuronal compartments both structurally and functionally (1). As it has been well known for many years, the fundamental neuronal structural compartments comprise a central cell body also referred to as soma, which holds the nucleus and subcellular organelle majority in the same way as other non-polarized cells, emanating a single long axon and multiple shorter branched dendrites to build up a structural basis of neuronal network for the directional information flow in nervous system **(Figure 1)**.

The axon is typically several times longer than dendrites and maintains a consistent diameter which varies in different type of neuron from 0.2 to 10 μm as it extends to send signals (2). Although thinner at the starting point comparing to dendrites, axon branches mostly in obtuse angle many times before it ends and those branches decrease very little in diameter, so as to transmit signals with a comparable and consistent conductivity to other neurons through synaptic terminals. Dendrites are thicker at the starting point but shorter in length and taper readily as they branch in acute angles extensively to form a tree-like structure (2, 3). Those branched minor dendrites contain numerous dendritic spines enriched in neurotransmitter receptors to receive signals from other neurons. Thus these mosaic-like morphologically distinct neuronal domains-soma, axon, dendrites-provide a structural basis for the functional polarization of a neuron.

The compartmentalization of axon, dendrites and soma, as the basic constituents of a neuron, relies on the distinct arrangement of cytoskeletons, which include microtubules and actin filaments (4). Both axon and dendrite are built on a central core that contains microtubules and neurofilaments surrounded by actin-rich cortex (5). The initial specification of the axon which is normally considered as the start of

neuronal polarization requires local dynamic instability of actin and stabilization of microtubules (6). Microtubules in the axon are all oriented plus-end pointing outward of soma, whereas dendrites and soma contain microtubules of both plus-end and minus-end mixed polarity and pharmacological stabilization of microtubules is sufficient to induce axon formation (7). The differential distribution of some cytoskeleton-associated proteins and local differences in phosphorylation reflect polarization of axon and dendrites as well. For example, the high molecular weight form of the microtubule-associated protein MAP2 is present in the soma and dendritic domain but is absent from axons. Neurofilaments, although their abundance varies, are present in both dendrites and axons, but their highly phosphorylated forms are restricted to axons (8). Furthermore, the polarized cytoskeleton also provides the basis for selective trafficking and retention of subcellular components in the coming stages for the further polarization of neuronal compartments (9).
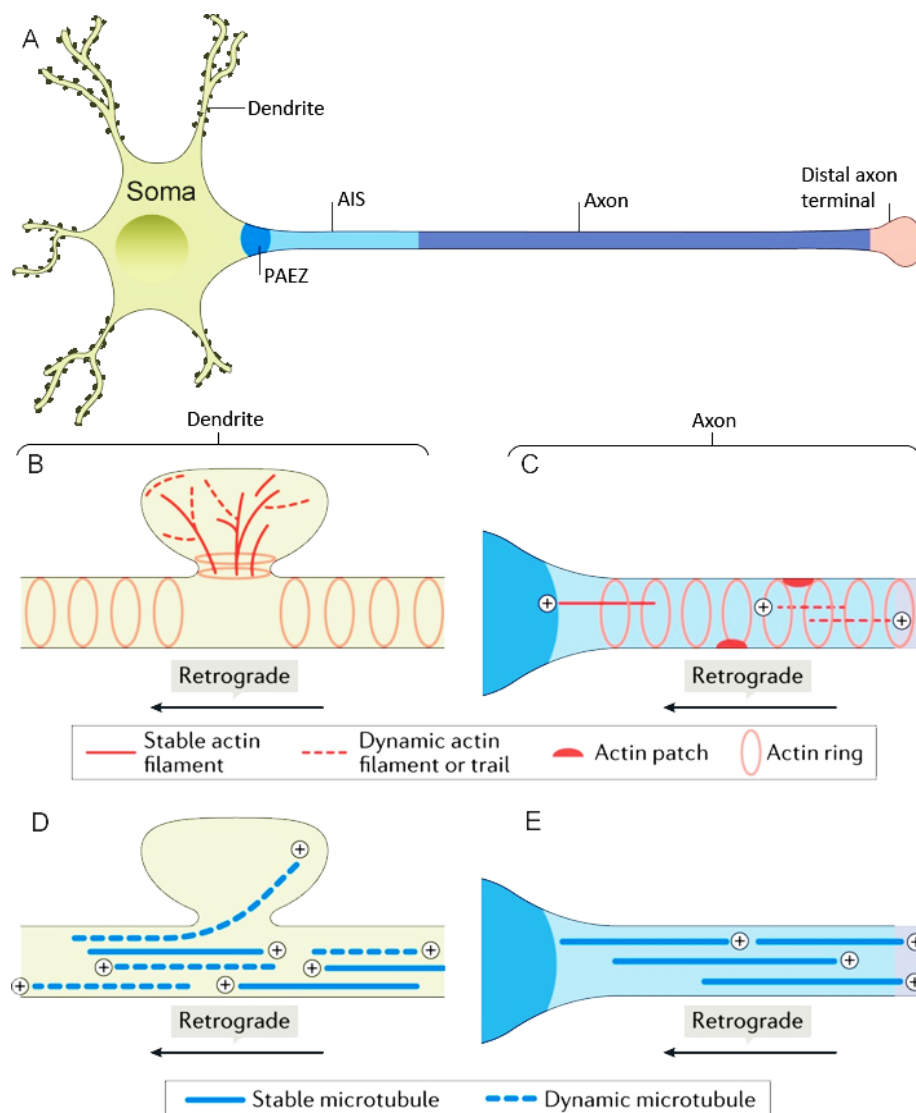
Figure 1. Polarized morphology of a neuron

(A) Principle neuronal compartments include the soma (cell body), dendrites, pre-axonal exclusion zone (PAEZ), axon initial segment (AIS), axon shaft and distal axon terminal. **(B)** Dendritic spines are enriched in a network of stable and dynamic F-actin. Actin rings are present in dendrites (10). **(C)** Actin rings are also found along the axon shaft which are known to be associated with ankyrin B and βII spectrin (11, 12). Other actin-related structures in axons include actin patches and dynamic actin trails (13). **(D)** Microtubules along dendritic shafts are organized with mixed polarity whereas a more uniform plus-end-outwards polarity is found in distal dendrites (14). Dynamic microtubules can invade dendritic spines (15, 16), possibly placing motors or cargoes in this compartment. **(E)** Microtubules in the axon are almost uniformly plus-end-outwards and tiled into overlapping arrays (14). Modified from (17).

4. 1. 2. Boundary between axonal and somatodendritic domain

However, in addition to the three basic neuronal compartments, an individual neuron usually can be viewed as a combination of axonal and somatodendritic domains, based on their distinct cytoskeletal features and functional polarity. These two fundamental domains are isolated and maintained by two subdomains, pre-axonal exclusion zone (PAEZ, which was referred to as axon hillock before) and the axon initial segment (AIS), which are usually considered as cytoplasmic boundary inside of a neuron **(Figure 1)** (18). PAEZ and AIS both play critical roles in maintaining neuronal polarity between axonal and somatodendritic domains attributing to their topological and functional properties.

Generally, newly synthesized proteins need to be sorted before being transported to specialized neuronal compartments by selective incorporation into specific populations of vesicular transport carriers. Such polarized sorting of transport vesicles occurs at the PAEZ, in which the somatodendritic markers are excluded, as somatodendritic vesicles budding from the Golgi complex fail to enter the axon at the PAEZ. PAEZ is closely related to the affinity of the vesicles to an appropriately directed microtubule-based motor protein, where these vesicles move to their corresponding neuronal domains along cytoskeletal tracks subsequently (9). This structure, however, excludes not only somatodendritic vesicles but also larger

organelles, such as the Golgi complex and the rough ER, thereby closely involved in constituting the cytoplasmic boundary for the somatodendritic and axonal domains (18, 19).

Another major structure in bounding between the somatodendritic and axonal domains locates at the AIS, a specialized region of the proximal axon, and typically emerges directly after PAEZ from the soma; occupies the first 20–50 µm of axonal length which varies from neuron to neuron (20). The AIS comprises a high concentration of surface voltage-gated ion channels and cell-adhesion molecules that are anchored by a submembranous assembly of ankyrin G (AnkG) and βIV spectrin **(Figure 2)**. The voltage-gated ion channels perform the main function of the AIS, which is the generation of action potentials in response to synaptic inputs. Additionally, the highly ordered structure of the AIS constitutes a barrier for the plasma membrane proteins and lipids between the somatodendritic and axonal domains. This vesicle-sorting function of the AIS was shown to depend on a network of polarized actin filaments that act as a physical barrier for the entry of somatodendritic vesicles (21) or as tracks for myosin-Va-dependent retrieval of somatodendritic vesicles that enter into the AIS (22, 23). This dynamic sorting along the PAEZ-AIS continuum can thus explain the polarized distribution of cytoplasmic components between the axonal and somatodendritic domains.
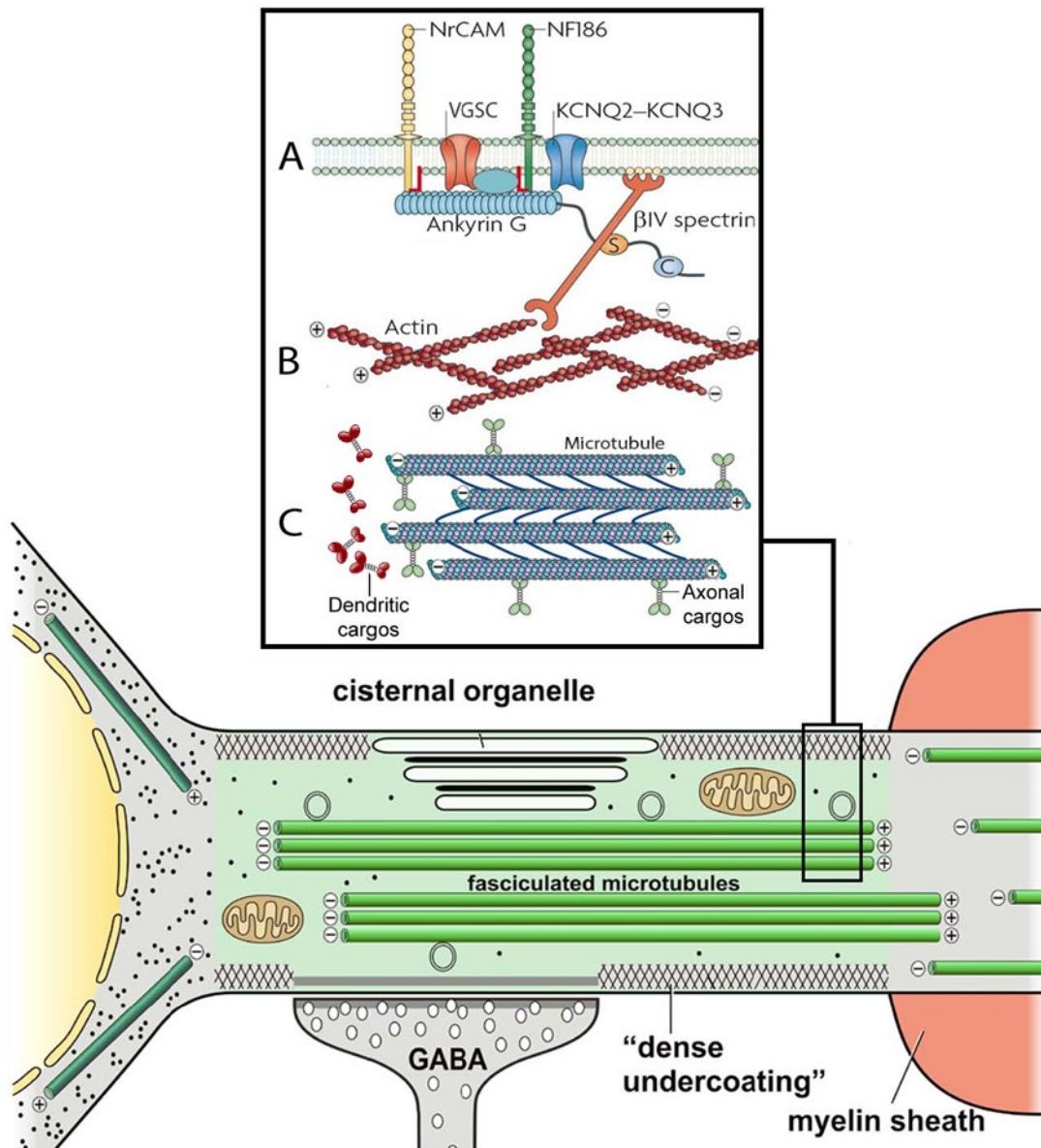
Figure 2. The subcellular and molecular characteristics of the AIS

The AIS is contacted by GABAergic axoaxonic synapses and contains the cisternal organelle, fascicles of uniformly polarized microtubules, and the dense-undercoating which lies beneath the axolemma. **Inset: (A)** The membrane adaptor protein Ankyrin G is linked to the actin meshwork by βIV spectrin. Ankyrin G itself anchors voltage-gated sodium channels (VGSC), potassium voltage-gated channels (KCNQ2/3), neuronal cell adhesion molecule (NrCAM), neurofascin 186 (NF186). **(B)** Actin meshwork comprised of mixed dynamic actin trails. **(C)** Fasciculated microtubules connected by cytoplasmic bridges. Transported compartment-specific vesicles/cargos are highlighted in red and green. Axonal microtubules exhibit a

uniform orientation with plus-ends pointing to the distal axon. Inset modified from (24).

However, the precise location and length of the AIS differ not only in different neurons but also in the different developmental stage of a neuron and in response to different neuronal activities, which are now considered as part of the neuronal plasticity (25, 26). This plasticity of the AIS morphology is finely tuned to adapt to physiological or pathological cellular changes, either in short-term (seconds to minutes) or long-term (hours to days) (27). During development, the AIS shortens or lengthens depend on different neuronal types studied (28, 29). Deprivation of external stimuli results in AIS lengthening, while elevated neuronal excitability leads to a distal shift along the axon (30, 31), which demonstrate that the location and length of the AIS have a significant impact on neuronal activities.

Regarding the spatial layout of the PAEZ-AIS continuum in a neuron, diversity exists in addition to the common neuronal topology that AIS should be localized independent from dendrites. It has been found that dendritic origin of axons exist in a subset of GABAergic interneurons for years (32), while axons of CA1 pyramidal cells have been thought to originate from the soma until recently, Thome et al. found that axons of rodent hippocampal pyramidal neurons frequently stemmed from a basal dendrite instead of from soma especially in central CA1 (33). Furthermore, those axon-carrying dendrites manifested a "privileged" channel for synaptic inputs as axon-carrying dendrites produced output action potentials at a lower voltage threshold as measured at the soma (33). The authors referred to the pyramidal neurons with dendritic axon origin as "AcD" neurons, and those with somatic axon origin as "nonAcD" neurons, hence established the existence of diversity with regard to the topological organization of the AIS in hippocampal pyramidal cells, also highlighted the profound impact of this structural diversity on CA1 pyramidal neuron electric signal transformation (34) **(Figure 3)**.
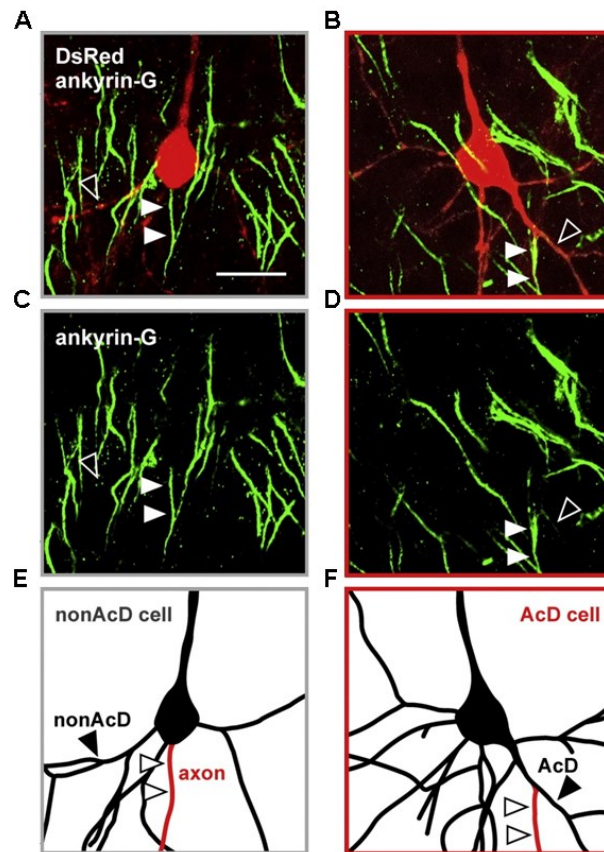
Figure 3. Morphology of AcD and nonAcD neurons

(A, C, E) show a nonAcD cell with the axon emanating from the soma. **(B, D, F)** show an AcD cell with the axon emanating from a dendrite – the so-called axon-carrying dendrite (AcD). Scale bar represents 20µm and applies to all figures. (A–D) Maximum intensity projection of confocal images of the CA1 pyramidal with soma and proximal dendrites labeled by DsRed (black arrowheads mark a proximal basal dendrite). Axon origin is identified by AIS-specific marker ankyrin G (green; white arrowheads). **(E, F)** Reconstructions of the nonAcD and AcD cell morphology (axon in red). Taken from (33).

4. 1. 3. Membrane protein compartmentalization in AIS

The neuronal polarity reflects also on the distribution of the membrane proteins in neurons, especially in the AIS. Most membrane proteins are not uniformly distributed along axons and dendrites but are instead restricted to specific subdomains, such as AIS, nodes of Ranvier or postsynaptic sites. After sorting and reaching the correct destination on the plasma membrane, the maintenance of the polarized membrane

proteins is accomplished by anchoring those membrane proteins to submembraneous scaffolding proteins keeping them away from moving to a different domain by lateral diffusion within the membrane. For example, sodium channels are restricted to AIS through their interaction with ankyrin G, βIV spectrin and the cortical actin network. It is striking that different members of the same family often have different distributions. This is particularly obvious in the case of the voltage-gated Na^+ and K^+ channels, and it applies to calcium channels as well (20). One reason for the remarkable diversity of channel types may be to allow channels with different functional characteristics to be targeted to different cellular domains (2) **(Figure 2)**.

The AIS serves as a key site for action potential (AP) initiation and separates neuronal input and output domains. Several proteins, including Na^+ channels, the scaffolding proteins ankyrin G and βIV spectrin, and the cellular adhesion molecule neurofascin 186, form a protein-dense segment of approximately 20-50 μm in length, located near the soma as described before (25, 35). Na^+ channels provide the main transient inward current responsible for the rapid depolarizing phase of the AP. Morphological studies indicate that Nav1.6 is the main Na^+ channel isoform found in the AIS of neurons in the adult CNS. The Nav1.1 subtype is also found in the AIS of GABAergic interneurons, retinal ganglion cells, and spinal cord neurons (36-38). Nav1.2 is primarily expressed in the AIS early in development and in unmyelinated axons of adults (39), but has also been reported in the proximal part of the AIS of pyramidal neurons of the cortex and hippocampus (40). The AIS is known to express various types of K^+ voltage-gated (Kv) channels. The predominant K^+ channel in the AIS of most neuronal types is the low-threshold Kv1 subtype. High levels of antibody staining for Kv1.1 and Kv1.2 channels are found in the AIS of most neuronal types (20, 41-43). Both Kv1 and Kv7 have low-voltage-activation characteristics and can directly affect the AP threshold, thus contribute to the repolarization of single action potentials and modulate action potential duration and frequency. In this regard, it is plausible to speculate that the elongation of the AIS increases the K^+ current in the axon, which may counterbalance the increase in the Na^+ current and reduce the excitability of the neurons. Besides, a long AIS usually can decrease the membrane excitability in some neurons (44, 45), which links Kv tightly to the structural plasticity of the AIS.

The structural plasticity of the AIS, however, depends on the activity of voltage-gated calcium channels and results in an adjusted threshold for AP firing homeostatically (46). It has long been recognized that organelles sequestering Ca^{2+} are localized to the AIS of pyramidal neurons of the neocortex and hippocampus (47). These ER(endoplasmic reticulum)-like organelles termed as cisternal organelle (CO) **(Figure 2)** are positioned close to the cell membrane, contain Ca^{2+} ATPase-type Ca^{2+} pumps (48, 49), and are thought to be equivalent to the spine apparatus (SA), another ER-like structure located in a subset of mature dendritic spines (50). One obvious function of these organelles would be sequestering calcium that locally enters the AIS via voltage-gated Ca^{2+} channels. Consistent with this idea, P/Q-type Ca^{2+} channels are present in the AIS of cerebellar Purkinje (51) and neocortical pyramidal neurons (which also contains N-type Ca^{2+} channels), whereas the AIS of GABAergic interneurons from the dorsal cochlear nucleus contains R and T type Ca^{2+} channels (52).

In addition to being critical for intrinsic excitability, the AIS of some neuronal types receives inhibitory synaptic input (53). In cortical pyramidal neurons this input is exclusively GABAergic **(Figure 2),** originating from a specific set of interneurons called chandelier or axoaxonic cells (54). These terminals are found in the neocortex and hippocampus, where they align to postsynaptic GABA receptors containing α2 subunits and are thought to provide inhibitory control over AP initiation (55). GABA α receptors containing α1, α2, or α3 subunits are found enriched at synapses, while α4, α5, and α6 are found primarily extrasynaptically (56). Of the synaptic α subunits, α2 subunits are enriched at the AIS, few of GABA α receptors at the AIS contain the α1 subunit (57, 58).

4. 1. 4. Polarized organelle distribution in neurons

As part of neuronal polarity, the distribution of intracellular organelles presents a far more complex picture when compared to that of membrane proteins. Unlike nonpolarized cells, neurons have a soma, dendrites, and axon with different organelle compositions. Although some organelles are widely distributed throughout the neuronal cytoplasm, others are segregated to either the axonal or somatodendritic domains **(Figure 4)**. Recent findings show that organelle segregation is largely established at the PAEZ (see sections above) (59). Polarized sorting of cytoplasmic organelles at the PAEZ is proposed to depend mainly on their

selective coupling with different microtubule motors and moving along different microtubule tracks. Therefore, it is the distinct properties of microtubule tracks in different neuronal domains that determine the specificity and direction of organelle movement by corresponding microtubule motor proteins (60).
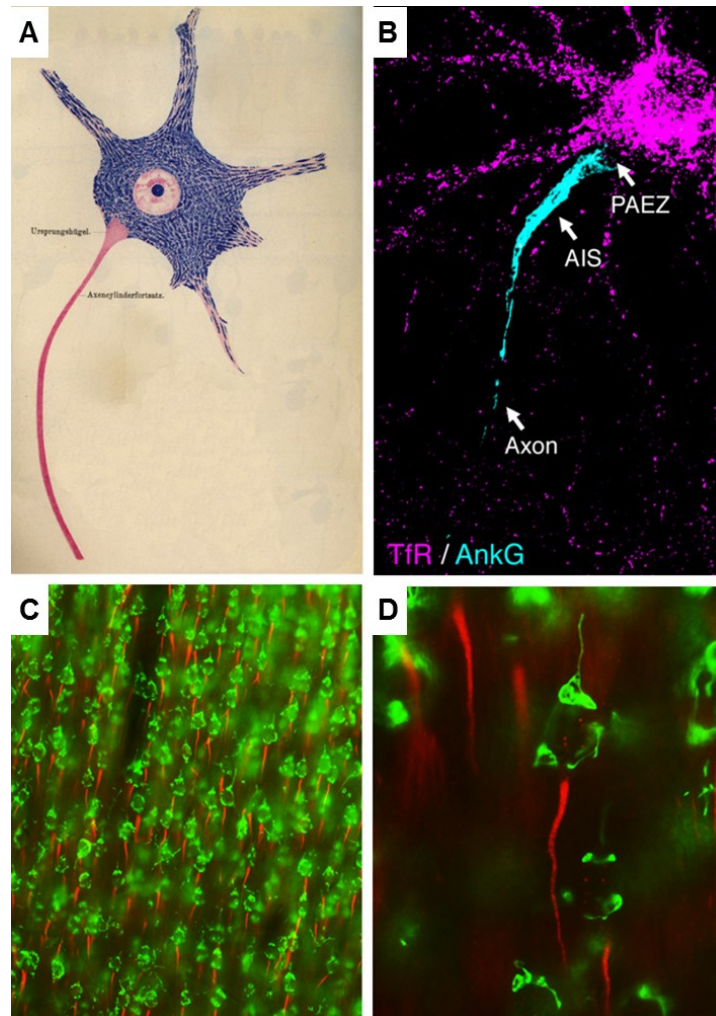
Figure 4. Polarized distribution of neuronal organelles

(A) Illustration of spinal cord motor neurons showing exclusion of Nissl bodies (rough ER) from the proximal axon, modified from (61). (B) Transferrin receptor (TfR; magenta)-containing somatodendritic vesicles (most of them are classical early and recycling endosomes) are excluded from the axon at the level of the PAEZ, proximal to the AIS (cyan) in cultured rat hippocampal neurons, taken from (19). (C, D) Exclusive localization of Golgi apparatus (GM130; green) in soma and proximal dendrites and devoid from axon (pIkBa AIS marker; red) of cortical neurons in rat. Modified unpublished data from C. Schultz.

In neurons, the rough ER, ribosomes and the Golgi complex, where membrane proteins are synthesized and processed, are all largely prevented from entering the axon (18)**(Figure 4)**. The Golgi complex, in particular, has a characteristic distribution: in addition to the familiar juxtanuclear cisternae found in most cell types, small Golgi outposts are found near dendritic branch points, and even more substantial Golgi stacks are observed in larger dendrites but never in the axon at the level of PAEZ and AIS continuum (62, 63). Cargo vesicles containing transferrin receptors (TfR), which are considered as classical early and recycling endosomes mostly, are transported directly to the somatodendritic domain and excluded from the axon in the cultured rat hippocampal neurons (64). In contrast, other organelles, such as the smooth ER, mitochondria, peroxisomes (52), autophagosomes etc., are more ubiquitously distributed in neurons, but still mostly concentrated in the soma and present in discrete puncta along both the dendrites and the axon (18, 60, 65).

4. 2.   Morphology and function of neuronal ER

Among all those polarized cytoplasmic organelles in neurons, ER is one of the most striking owing to their large size and heterogeneous morphology. ER is a highly conserved organelle in eukaryotic cells for its vital importance in many cellular processes (66). As in other eukaryotic cells, neuronal ER also appears as a continuous single membrane organelle that extends from the nuclear envelope in the soma into distal dendrites, axon growth cones and synaptic terminals, as well as plasma membrane (PM) forming ER-PM contacts, which is of particular importance in regulation of intracellular Ca^{2+} dynamics and signaling, lipid traffic and homeostasis (67). Although the shape of ER is highly heterogeneous and varies from different cell types to developing stages, ER can be generally divided into three domains: the nuclear envelope, rough ER sheets studded with polyribosomes and smooth ER (SER) tubules with few ribosomes (68). Most of the ER sheets, which are cisternal structures with two closely apposed membranes, appear in the perinuclear region. ER tubules, which typically form a reticular interconnected network, exist in both the perinuclear and peripheral regions (69).

The subcellular distribution of ER sheets and tubules in neurons is tightly controlled as ER plays a crucial role in many neuronal activities, such as the membrane expansion that occurs during dendrite and axon formation, presynaptic and postsynaptic signaling pathways. Compared to other cells, the integrity of ER network

is more vulnerable to functional impairment in neurons (70). As already been outlined above, the neuronal RER is abundant in the soma and the proximal dendritic regions **(Figure 4)**, mostly involved in the massive protein synthesis, quality control, and trafficking. Neuronal SER, however, extends lengthwise into axon and distal dendrites forming a network of longitudinal tubules, connecting regions and some specialized cisternal structures, which are associated with lipid synthesis and Ca^{2+} sequestrations beneath the plasma membrane (71, 72) **(Figure 5)**.

In particular, the continuity of SER in neurons is important for the propagation of Ca^{2+} signals over long distances and the transport of lipids and proteins (73). Topologically, the ER in dendrites and axon is located in the cortex of the cytoplasm with thin branches traversing the opposite side (74), also appears to anchor at perisynaptic sites via cytoskeletal elements or by tethering ER components to the postsynaptic density (75). The complexity of dendritic ER within the dendritic shaft area correlates with not only the local density and maturation stage of excitatory synapses but also the sites of dendritic branch formation (76), linking ER morphology to the changes in synaptic organization and dendritic morphogenesis (77, 78).
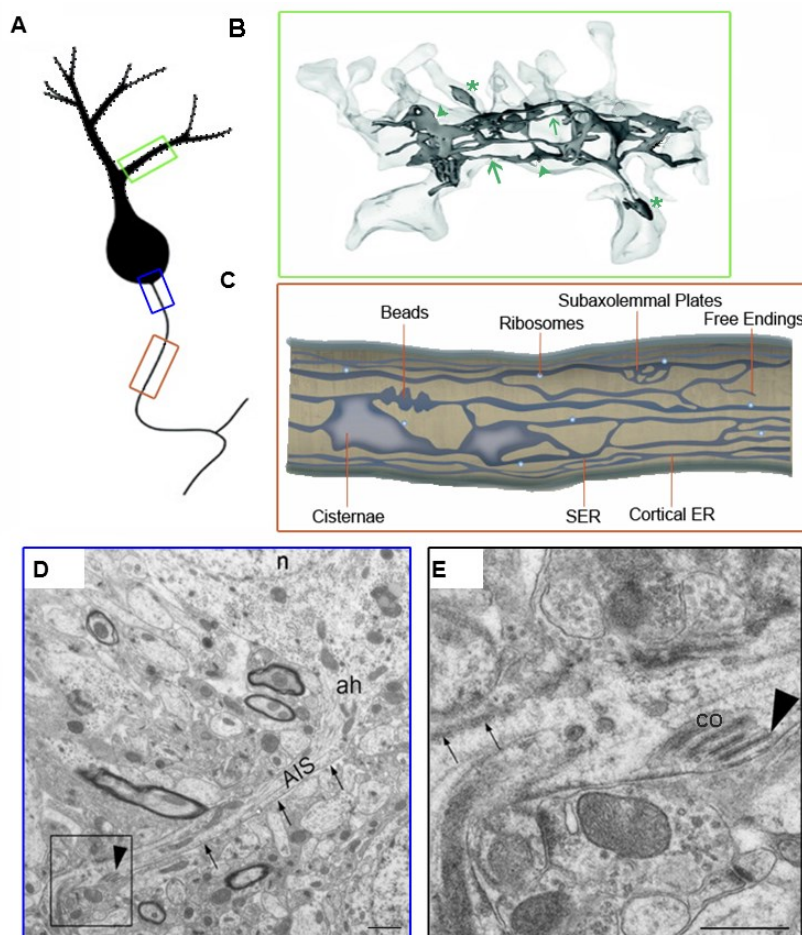
Figure 5. ER morphology in neurons

(A) A schematic neuron with multiple dendrites and one axon. Colored boxes indicate dendritic (79) and axonal (orange) regions. **(B)** Schematic magnification of the dendritic box showing a 3D reconstruction of the SER network with flat regions (arrowheads), thin tubules (arrows), and spine apparatus (asterisks). Figure adapted from Figure adapted from (74). **(C)** In axons, the SER is composed primarily of a three-dimensional longitudinal network of tubules and larger interconnected cisternae. The network is associated with sparse ribosomes, contains occasional subaxolemmal plates, free endings, beaded areas and in some regions runs close to the plasma membrane. Adapted from (66). **(D)** An electron micrograph of a CA1 pyramidal neuron in the mouse hippocampus. The AIS (arrows) can be followed from its origin at the axon hillock (ah) over a distance of approximately 10 μm. The framed area is shown at higher magnification in E. It contains a cisternal organelle (CO, arrowhead). **(E)** Higher magnification of the framed area in D. The CO consists of stacked cisterns of ER interdigitated by electron-dense material (arrowhead). The AIS-typical dense undercoating is indicated (small arrows). n, nucleus. Scale bar: 1 μm in D; 0.5 μm in E. Modified from (50).

Some specialized neuronal ER arrangements, SA and CO, both are essentially stacked ER situated in mature dendritic spines and the AIS, have been found to impact primarily on Ca^{2+} signaling and both co-localized with the actin-binding protein, SP, which is essential for their establishments. Due to the its abundance of dendritic spines in neurons, SA has been studied much more extensively than CO. SA has been proposed to play a key role in the modulation of synaptic plasticity, as mice deficient in SP lacking spine apparatus showed deficits in long-term potentiation and spatial learning (80, 81). CO, although been limited studied, has been suggested to regulate membrane excitability at the AIS, possibly via coupling surface membrane depolarization to release Ca^{2+} which may, in turn, regulate GABA α receptor signaling and AIS plasticity (82). Taken together, the close proximity of the ER to inhibitory postsynaptic sites in AIS and a subset of excitatory dendritic spines implicate a role of neuronal ER in the modulation of synaptic transmission (76, 83).

It is evident that ER contacts with other organelles constantly and frequently given its large and diffuse volume (84). ER network may act as a highway supporting the translocation of other organelles and structure, such as mitochondria, peroxisome and Golgi complex (85). The ER contacts other organelles at discrete sites, where

lipid transfer and calcium exchange occur. Various aspects of organelle dynamics, including fission, maturation and positioning, are also regulated by formation of contacts with the ER (70). The ER interaction with other organelles is highly dependent on the microtubule cytoskeleton. Also the ER network itself keeps a constant remodeling by several distinct mechanisms, such as ER tubule extension along microtubules to contribute various cellular tasks, especially protein trafficking to post-ER compartments and transport of ER-resident proteins from soma (86). Although still mechanistically unclear, ER dynamics is undoubtedly coupled to protein trafficking in neurons, and contributes to the modulation of morphogenesis and synaptic function (75). When ER morphology or dynamics is perturbed, organelle contacts, membrane trafficking and other ER functions are affected, and neurodegenerative diseases may result. These insights have increased interest in ER morphology changes associated with the development of neuronal axons and dendrites as well as their integration with synapse signaling pathways. A number of proteins involved in shaping and distributing the ER network are mutated in neurological disorders, particularly the hereditary spastic paraplegias, emphasizing the importance of proper ER morphology for the establishment and maintenance of neuronal compartmentalization (72, 87).

4. 3.   Role of PO in neurons

4. 3. 1. General aspects of PO function

Comparing to neuronal ER, neuronal POs appear to be simpler in morphology and subcellular distribution, which is closely relevant to the contacts with the ER network. (9, 65, 88). Generally, POs are dynamic, multifunctional and essential organelles that are present in all eukaryotic cells, performing a wide range of crucial functions involving in cellular metabolism, signaling and viral defense which are essential to the health and viability of the organism (89). POs are characterized morphologically by a protein-dense matrix surrounded by a single membrane about 0.1-1 µm in diameter and biochemically by a unique set of proteins, containing one or more H_2O_2-generating FAD-dependent oxidases and the prototypical H_2O_2-decomposing catalase (90). They play a critical role in a variety of cellular catabolic and anabolic metabolic pathways, including fatty acid β-oxidation, and plasmalogen and bile acid synthesis etc. In order to obtain such functional versatility, POs dynamically respond to the cellular environmental stimuli or internal metabolic demands by changing in

number, size, structure, protein composition and metabolic functions (91). Accordingly, the control of peroxisome abundance should be achieved through a tight regulation of PO biogenesis and degradation also known as pexophagy, a type of autophagy-specific for POs (92, 93).

PO formation and proliferation primarily rely on the growth and asymmetric division of pre-existing POs in a series of consecutive, partially overlapping processing, which include elongation and constriction of the pre-peroxisome, final membrane scission and separation. Then comes the growth and maturation of the newly formed POs, via the insertion of PO membrane proteins (PMPs) and lipids through ER-derived vesicles and matrix protein import (94-97). Additionally, *de novo* formation, whereby pre-peroxisomal vesicles bud from the ER, has been proposed as a supplementary mechanism for PO biosynthesis (98-101) **(Figure. 6)**.
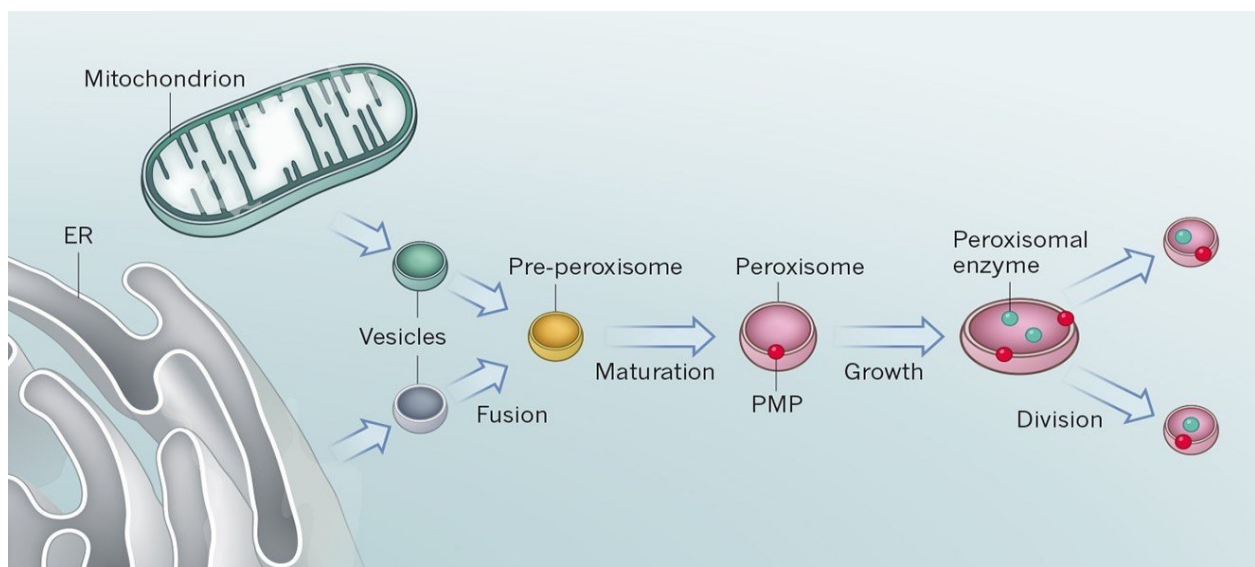
Figure 6. Peroxisome formation

Peroxisomes can arise through the growth and division of existing POs or through *de novo* formation. The organelle-derived membrane vesicles from the ER fuse with mitochondrially derived vesicles (MDVs) to form a pre-peroxisome which matures into a fully functional peroxisome by the acquisition of other components including peroxisomal membrane proteins (PMPs) and enzymes [93]. These newly formed peroxisomes replicate by growth and division. Taken from (102).

Peroxisomal membranes contain PMPs, which are primarily metabolite transporters and peroxins. Peroxins encoded by PEX genes are involved in various aspects of PO

biogenesis, including PO formation, fission, as well as matrix and membrane protein import (100). Peroxisomal matrix proteins are post-translationally targeted to POs from the cytosol by peroxisomal targeting signals (PTSs) (95). Defects in genes encoding peroxisomal proteins lead to a variety of diseases termed as peroxisomal disorders that can be grouped into single peroxisomal enzyme deficiencies (PEDs) and peroxisomal biogenesis disorders (PBDs). The clinical phenotype of peroxisomal disorders is often dominated by pathologies in nervous systems. The affected PO function or biogenesis contributes to the developmental defects of the brain caused by demyelination, loss of axonal integrity, neuroinflammation or other neurodegenerative processes, which could lead to a group of severe developmental brain disorders that can be lethal during childhood (103) and some slowly progressing neurological disorder as well (104-107). It has been found that the abnormality of α-synuclein, which is the major constituent of Lewy bodies, the pathological hallmark of Parkinson's disease, and lipid metabolism defects were also present in PBD mouse models (108). Besides, the level of PO proliferation in hippocampal neurons has been reported to be correlated with the protection from β-amyloid neurodegeneration, which is linked to Alzheimer's disease (109). These data, together with the emerging roles of POs in cellular aging (110), highlight the importance of understanding PO physiology for human health and their roles in the development and treatment of neurological disorders.

4. 3. 2. Motility and positioning of PO

It has been extensively studied that POs are abundant and distribute normally homogeneously throughout the cytoplasm to protect cells from toxic substrates that can be metabolized by POs. PO motility, which contributes to each specific subcellular positioning of POs, allows the communication with other subcellular compartments and fulfillment of multiple cellular functions (111). It has also been studied in cultured mammalian cells that PO motility is microtubule-based bidirectional movement and mediated by kinesin, dynein motor proteins and dynein activator complex dynactin (112-115). POs' movement can be classified as static, short-range motions and long distance saltations in all possible directions (116). Computational analysis and modeling showed that only a small percentage 10-15% of fast long-distance movement of POs facilitate a uniform positioning of the organelles with optimal energy consumption (117, 118). The maximal speed of PO

moving over a long distance was estimated as 10 μm/s, while the average speed was ranging from 0.1 to 1 μm/s in those cells(111, 119). It has also been suggested that bidirectional movement of PO is due to the binding of PO transferred from one motor protein to the other, which are turned on and off alternatively during the back-and-forth movement of the PO. It also appears that several kinesins or dyneins can work together to speed up the moving of PO (115). Although the motility of POs has been studied frequently in cultured neurons, most of the studies are microtubule-associated cargo trafficking centered, with very little focus on the association of PO motility and PO positioning in highly polarized neurons. According to some previous studies, neuronal POs accumulate preferentially in axon terminals during early postnatal development (120), but devoid in the axons of mature protection neurons (121). A detailed PO population and distribution in different neuronal compartments and its molecular mechanism in the individual neuron is still lacking experimental data.

To highlight this, it has been suggested that neurodegeneration of Zellweger patients characterized by PO deficiency in cells and Morbus Alzheimer patients are partly resulting from the uneven subcellular distribution of POs (122, 123). Furthermore, loss of DLP1 which is a shared fission factor between PO and mitochondria, has been linked to the neurodegeneration in brain, suggesting that improper organelle distribution in neuron resulted from the blocked PO and mitochondria division contributes to the neuronal pathologies (124-126).

4. 3. 3. Contacts between PO and other subcellular compartments

Apart from the microtubule-dependent PO motility, the contacts between PO and other subcellular compartments including themselves are also contributing to the PO distribution in neurons. In order to optimize their multiple cellular functions, POs must communicate and cooperate with other organelles including themselves. For many years electron microscopy (EM) images of POs from mammals, have demonstrated that peroxisomal membranes are juxtaposed to other organelles, mainly the ER, lipid droplets (LDs) and mitochondria (127), suggesting that contact sites form between two organelles. A common way of communication between POs and other organelles is through physical membrane contact sites where tethering complexes are formed, facilitating close-range interactions such as transport of small molecules, intracellular signaling, organelle trafficking etc. (128, 129). These tethering structures can be

assembled by the defined protein partners on the opposing membranes or by protein-lipid interactions, which can keep the two membranes in close range while disenabling membrane fusion (129).

Recently it has become evident that POs and mitochondria form even more tight relationship than it could be predicted previously (127, 130). This tight cooperation of PO and mitochondria includes β-oxidation of fatty acids (131) to maintain lipid homeostasis and metabolism of reactive oxygen species (ROS) (132). In humans, very-long-chain fatty acids (VLCFAs) are degraded in POs by β-oxidation and then shuttled to mitochondria for further oxidation and ATP production, where a carnitine shuttle system and membrane pores are required (133). Additionally, mitochondria were found to export referred to as mitochondria-derived vesicles (MDVs) carrying mitochondria-anchored protein ligase (MAPL) targeted to POs (134).

Furthermore, both POs and mitochondria contact ER tightly and share some organelle fission factors (135, 136), implying a coordinated biogenesis of PO and mitochondria under certain physical conditions. These shared components include dynamin-like GTPase DLP1, Fis 1 and Mff. DLP1, recruited from cytosol, assembles in ring structure surround the membrane constriction during division in a GTP-dependent manner. While Fis 1 and Mff are tail-anchored outer membrane proteins and act as receptors for DRP1 at the organelle membrane in mammalian cells (137, 138). Depletion of those shared division factors inhibits both peroxisomal and mitochondrial fission and causes accumulation of elongated organelles (96). Additionally, POs and mitochondria were reported to cooperate in anti-viral signaling and defense (139, 140).

Therefore, it is not surprising that mitochondria are defective in some peroxisomal disorders (141). Although still not much is known about PO-mitochondria contact sites in mammalian cells, recent studies have shed light on possible contact sites between the two organelles. ATP binding cassette subfamily D member 1 (ABCD1) located to the peroxisomal membrane, whose loss of function causes X-linked adrenoleukodystrophy, and enoyl-CoA delta isomerase 2 (ECI2) have been proposed to be PO-mitochondria tethering partners (142). Pex34 and Fzo1 have also been suggested to play a role in PO-mitochondria tethering by a systematic analysis of cellular organelle contacts (143).

POs are frequently found juxtaposed to the ER-mitochondria contact sites and pyruvate decarboxylase complex in mitochondrial matrix (144, 145), which probably reflects an efficient transporting of metabolites by shortening the distance between the two organelles (146), suggesting a three-way junction **(Figure. 7)**. This connection between POs and mitochondria is formed at least partially by the tethering partner Pex11, a peroxisomal protein, and Mdm34, a subunit of mitochondrial localized ER-Mitochondria encounter structure (ERMES) (145, 147).
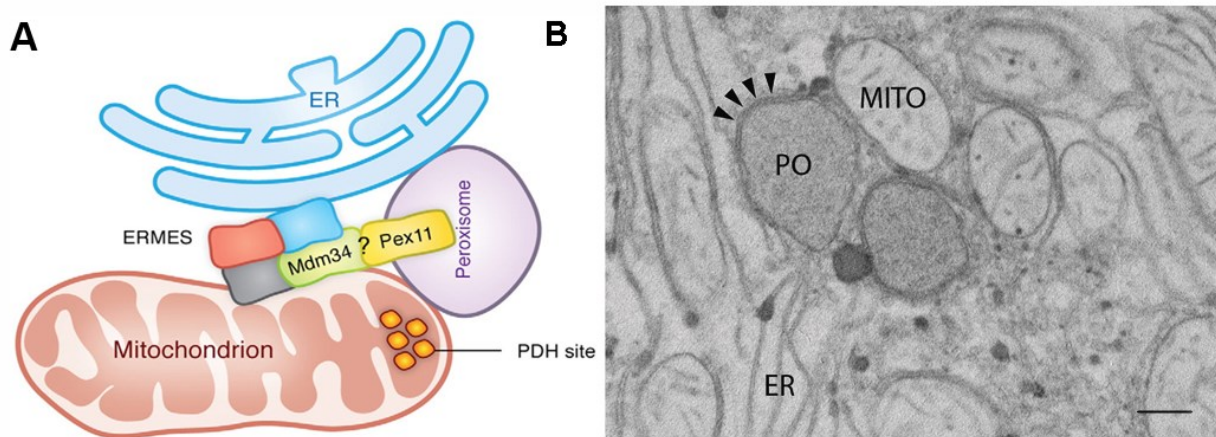
Figure 7. Three-way junction of PO, ER, and Mitochondria

(A) Schematic PO-ER-Mitochondria (Mito) contact site. Peroxisomes can be localized adjacent to a specific mitochondrial niche near the ER-mitochondria contact site. This three-way junction lies proximal to the pyruvate dehydrogenase (PDH) complex. The PO-Mito tether has been suggested to be mediated by Pex11, a key protein involved in peroxisome proliferation, and Mdm34, one of the proteins creating the ER-mitochondria tether (ERMES, ER-Mito encounter structure). Taken from (148). **(B)** Electron micrograph of PO juxtaposed to mitochondria and tubular ER in rat liver. Arrowheads indicate the contact sites of PO and ER. Taken from unpublished data of M. Islinger. Scale bar: 0.5 µm.

PO-PO contacts, however, have been observed in various organisms (114, 149). POs displayed either transient or long-term contacts, separating and re-connecting before movement resumed several times during a live-imaging course (118, 150). In mammalian cells, mature POs do not fuse and exchange membrane or matrix marker proteins (118), which exclude the possibility of molecular exchange through PO-PO connecting. Even though the physiological role of these contacts is still elusive, the

formation of small PO clusters and PO-PO contacts may represent functional units of POs and signal the cells so as to maintain the equilibration of PO populations (127).

4. 3. 4. ACBD5 as a mediator for PO-ER contacts

It has been known for years that POs and ER form tight structural connections, as shown in the ultrastructural studies decades ago that POs were often found in close proximity to ER (151). POs were often found apposed to ER tubules even wrapped by ER and short electron-dense intermembrane were interposed between associated POs and ER (152-154). Furthermore, the dynamic behavior of PO and the adjacent ER has been observed to be correlated as POs align with and follow the movement of neighboring ER tubules (155), which suggested intimate physical contact sites exist between the two organelles. Indeed, it has been proved that many cellular processes depend on such close cooperation between POs and ER, including lipid metabolism, phospholipid exchange, metabolite transport, signaling, and PO maturation, proliferation, inheritance, dynamic (156).

POs assemble from ER-derived precursor vesicles as described in both modes of PO formation (99, 157), and many peroxisomal membrane proteins are either dually localized to the ER and POs (158) or traffic through the ER en route to POs (159). POs co-work with the ER so extensively in the biosynthesis of ether-phospholipids and polyunsaturated fatty acids that defects in these pathways lead to neurodegenerative disorders (127, 160, 161). For example, one of the first steps in the synthesis of plasmalogens, which is the main materials of myelin sheath lipids in nervous system, is the formation of an ether bond, a process that occurs exclusively in POs. Then, the produced metabolite must be shuttled to the ER for further enzymatic modification, leading to the formation of plasmalogens (162). Although so many either functional or structural association evidence have been reported between the two organelles, to date, only two bona fide physical contact sites between POs and ER have been identified in yeast (163, 164) and mammalian cells respectively(165, 166).

In mammal cells, two independent research groups recently identified the same PO-ER tethering complex through different experimental approaches (165, 166). The tethering partners include the peroxisomal membrane protein ACBD5 (acyl-CoA binding domain protein 5) and ER-resident vesicle-associated membrane proteins

(VAP)-associated protein B (VAPB) **(Figure 8)**. Their tethering depends on the major sperm protein (MSP) domain in the VAP proteins and a two phenylalanines in an acidic tract (FFAT) motif in ACBD5. VAPs are tail-anchored membrane proteins and known to be residents of contact sites on ER to interact with proteins containing FFAT motif through their MSP domain (167-170), which play a critical role in contacting between ER and mitochondria or late endosomes (171, 172). The binding between MSP domain and FFAT motif occurs when the two are present and anchored to opposing membranes of organelles. ACBD5, as a FFAT motif containing protein, thus is important for the PO-ER binding in mammalian cells.
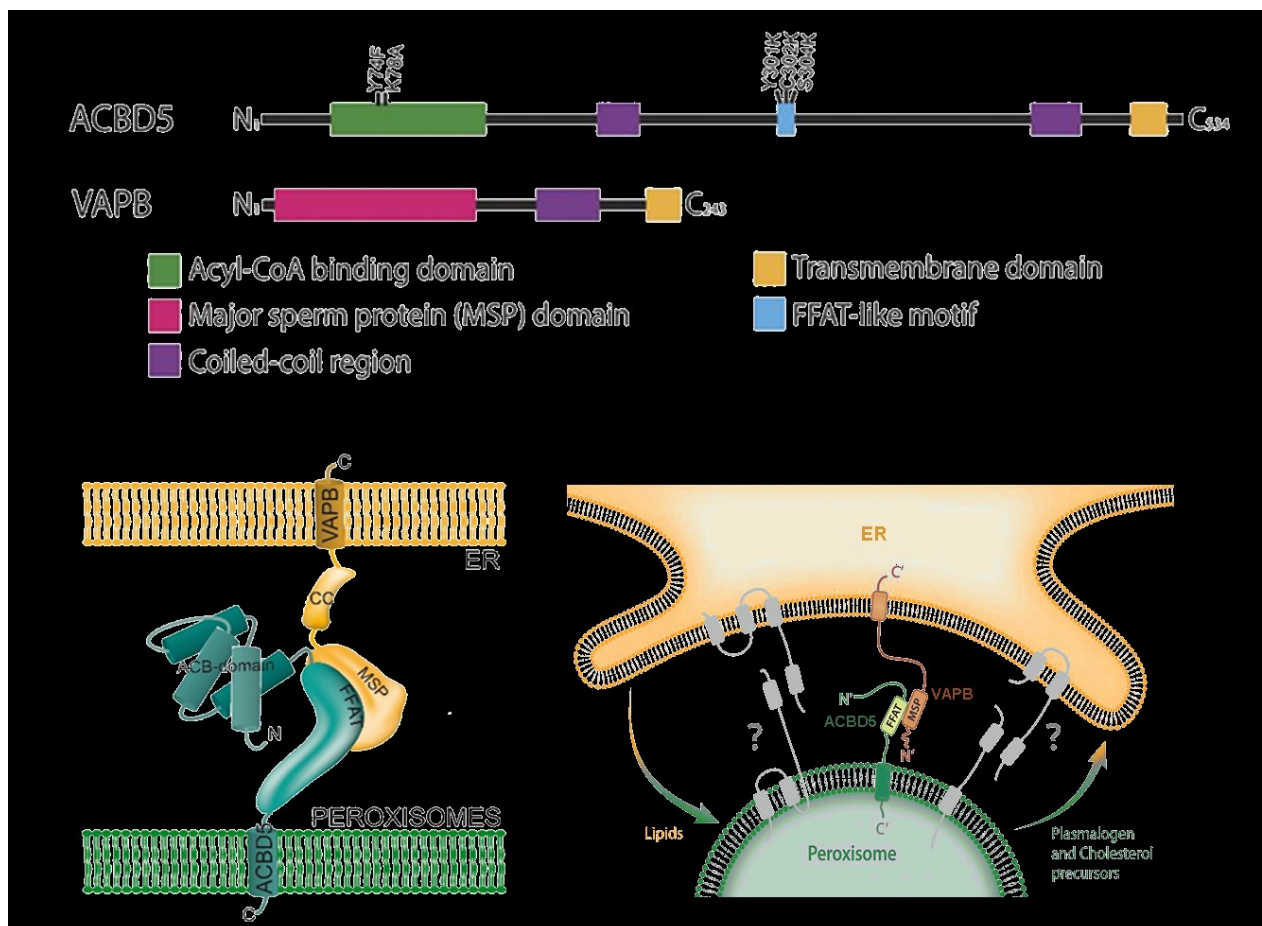
Figure 8. Schematic diagram of ACBD5 and VAPB

(A) Domain structure of VAPB and ACBD5. Mutations in acyl-CoA binding and FFAT-like motifs are indicated. **(B)** ACBD5–VAPB interaction is mediated through the FFAT motif of ACBD5 and the MSP domain of the VAPB protein. Taken from (165). **(C)** ACBD5 and the VAPB proteins are anchored to the PO or to the ER membrane, respectively, through a transmembrane domain localized at their C' termini, whereas their N' termini face the cytosol.

This contact may enable ER-to-PO transport of lipids, required for elongation and growth of the PO membrane, as well as PO-to-ER transport of plasmalogen and cholesterol precursors. Additional tethering complexes (proteins marked in gray) remain to be discovered. Modified from (173).

ACBD5, which is an acyl-coenzyme A binding domain-containing protein, was previously suggested as a lipid transfer protein for very-long-chain fatty acids (VLCFAs) (174). This family of ACBD proteins plays a role in the sequestration, transport, and distribution of long chain acyl-coenzyme A in cells (175). As long chain acyl-CoAs are intermediates in lipid metabolism and can be signaling molecules in gene regulation, a role of ACBD5 was suggested in mediating lipid metabolism(176-178). However, acyl-CoA binding domain of ACBD5 is not a necessity for PO-ER binding but might suggest a role in modulating the tethering (165). Additionally, a yeast ortholog of ACBD5, Atg37 (autophagy-related protein 37) was recently found to be specifically required for the formation of phagophore, the isolation membrane for autophagy, during pexophagy process (179). Previous studies revealed that ACBD5 was enriched in highly purified PO fractions and identified its exclusive localization in POs (179-181). Following that, ACBD5 was found predominantly localized at the spherical structure domain of PO membrane, which was then further studied in ACBD5 silenced cells shown that the remaining ACBD5 was localized at the globular domains of elongated POs (165, 182).

Since mutations in VAPB could cause a dominantly inherited amyotrophic later sclerosis (183), it is tempting to speculate that perturbation in PO-ER tethering may cause some pathological features of ALS or other neurodegenerative diseases. Study on ACBD5 may implicate certain role of PO-ER association in the progression of these neurodegenerative disorders. So far, mutation in ACBD5 was identified in four patients, all of whom presented retinal dystrophy (174, 184, 185). ACBD5 was completely absent from these 4 patients who also showed a notable accumulation of VLCFAs, which are exclusive substrates of peroxisomal β-oxidation, indicating a compromised PO functioning in the absence of ACBD5. It may because ACBD5 recognizes and recruits ER-derived cytosolic VLCFAs to POs for degradation (175). However, whether the impaired VLCFAs metabolism was caused by the loss of ACBD5 tethering with ER or by the loss of VLCFAs binding function of ACBD5 itself, is still unclear.

In cultured mammalian non-neuronal cells, disruption of ACBD5-VAPB tethering was found to alter PO-ER binding and impeder the growth of peroxisomal membrane, along with an increased PO motility, This suggests a leading role of ACBD5-VAPB tethering complex in PO-ER binding in mammalian cells (165). In view of this, it would be of interest for the study of PO motility and distribution in neurons through modulators of ER-PO binding, such as ACBD5. As POs cooperate with ER in so many cellular functions in neurons, it is tempting to speculate that ACBD5 might play multiple roles in PO maintenance and motility in neurons.

To summarize, as highly polarized neurons, although diversity exists in the axon origins (AcD and nonAcD neurons), their polarity reflects not only on their distinct mosaic-like morphology but distinct molecular structure beneath the plasma membranes of neuronal subdomains as well. Such as the GABAergic receptor α2 enriched in the AIS, specialized ER enriched in the AIS and mature dendritic spines. It is the positioning of the polarized neuronal organelles and membrane proteins that build up and maintain the functional polarity of each individual neuron, which is critical for overall neuronal network functioning. To study the polarized organelle distribution and influencing factors of that in neurons, the distribution of GABAergic synapses at the AS, maturation of specialized ER—CO in the AIS; POs positioning and motility, and the impact of ER-PO binding modulator—ACBD5 on that of POs, were examined and described in this study.

4. 4.   Objectives

Distribution of GABAergic axoaxonic synapses at the AIS of AcD and nonAcD neurons in hippocampus

The first aim of this study was to examine the distribution of GABAergic synapses at the AIS of AcD and nonAcD neurons in mouse hippocampal neurons. As described above, AcD and nonAcD neurons show distinct electrophysiological properties raising the questions whether the number of GABAergic synapses at the AIS could be relevant to such discrepancies of electrophysiological properties between AcD and nonAcD neurons in hippocampus.

Maturation of specialized ER–cisternal organelle (CO) in the AIS of AcD and nonAcD neurons

The maturation of CO, which usually is located in proximity to GABAergic terminals in the AIS was analyzed attempting to elucidate the formation of this putative Ca^{++} store in the AIS of AcD vs. nonAcD neurons. Specifically, the number and volume of CO during the development of AcD and nonAcD neurons were measured and analyzed at different development stages of cultured primary neurons.

Spatial associations between neuronal ER, PO, and mitochondria

In addition to the analysis of the specialized axonal ER-CO in the AIS, the polarized distribution of local ER and its associated subcellular organelles, such as POs and mitochondria, was also examined. Such insights into the spatial associations between these organelles would be required for the subsequent analysis on the impact of organelle contacts on the polarized distributions of organelles - especially of POs in neurons.

Molecular mechanisms regulating motility and distribution of neuronal POs

To study the neuronal PO distribution, among all those influencing factors, maintenance of PO-ER contacts could be one of the major factors underlying the distribution of PO in such highly polarized neurons. Altered expression of ACBD5, as a modulator of PO-ER binding, has been reported to impact the changes of PO in other non-neuronal cells. Therefore, whether the expression of ACBD5 in neurons could lead to similar alterations in neuronal PO proliferation or motility, which can further affect the distribution of neuronal POs, was examined in the current study.

5   MATERIALS AND METHODS

Unless described otherwise, the exact manufacture information and model types of the equipment used in the experiments can be found in the appendix.

5. 1. Experimental animals

All mice required in the experiments were sacrificed in accordance with the Germany Government Commission of Animal Care and the guidelines on the care of laboratory animals of the Heidelberg University, Medical Faculty Mannheim Animal Research Board. Pregnant wildtype C57BL/6JRj were purchased at embryonic day 11(E11) from Janvier Labs, France. Thy1-GFP reporter mice, which were provided from SFB project 1134 (Functional Ensembles), were established and produced in-house. All animals were kept on a normal laboratory diet (food and water were provided ad libitum) and housed under an inverted 12 hours light/dark cycle (light from 8 pm – 8 am) at a temperature of 22±2 °C and a relative humidity of 45 – 65%. All efforts were made to minimize the number of animals and their suffering.

5. 2. Plasmids and antibodies

All plasmids were cloned and amplified using DH5α™ Competent Cells (Invitrogen, Cat. No. 18265-017) with the provided protocols of the products. EGFP-SKL, myc-ACBD5(human), FLAG-ACBD5(human)-FFAT^{mut} and FLAG-ACBD5(human)-WT were generated as described in a previous publication (186). mCherry2-C1, mPlum-N1, and mCherry-Mito-7 were gifts from Michael Davidson (Addgene plasmid # 54563, #54629, # 55102) (187).

All the antibodies applied in the thesis were listed as follows:

Target	Source	Immunogen	Dilution	Host species	Use
ACBD5	Sigma HPA012145	Acyl-CoA-binding domain-containing protein 5 recombinant protein	1:500	rabbit	ICC
GABA$_A$Rα2	synaptic systems 224104	Synthetic peptide corresponding to AA 29 to 37 from rat GABA-A receptor α2		guinea pig pAb	IHC
GFAP	synaptic systems 173002	Recombinant protein corresponding to AA 1 to 432 from human GFAP	1:1000	rabbit pAb	ICC
GFP	chemicon/millipore MAB3580	Green Fluorescent Protein	1:1000	mouse mAb	ICC/IHC
MAP2	synaptic systems 188004	Recombinant protein corresponding to AA 2 to 314 from human MAP2-4 hu	1:1000	guinea pig	ICC
Myc	cell signaling 2276s	Synthetic peptide corresponding to residues 410-419 of human c-Myc	1:2000	mouse mAb	ICC
Pex14	ProteoGenix in-house		1:1000	guinea pig	ICC
RFP	chromotek	Red fluorescent protein (5FB)	1:1000	rat mAb	ICC
SERCA2 ATPase	Thermo Scientific MA3-910	Purified canine cardiac sarcoplasmic reticulum (IID8)	1:500	mouse mAb	ICC

Target	Source	Immunogen	Dilution	Host species	Use
Synaptopodin	synaptic systems 163004	Recombinant protein corresponding to AA 331 to 452 from mouse Synaptopodin	1:500	guinea pig pAb	ICC
TOMM20	Sigma HPA011562	Mitochondrial import receptor subunit TOM20 homolog recombinant protein	1:1000	rabbit pAb	ICC
VAPB	Sigma HPA013144	Vesicle-associated membrane protein-associated protein B/C recombinant protein;	1:200	rabbit pAb	ICC
VGAT	synaptic systems 131006	VGAT cytoplasmic domain	1:1000	chicken pAb	IHC
β4-spectrin	BioTrend in-house		1:500	rabbit pAb	ICC/IHC

Table 1 List of primary antibodies

Tabular list of primary antibodies used in the thesis. mAb: monoclonal antibody; pAb: polyclonal antibody; ICC: immunocytochemistry; IHC: immunohistochemistry.

Conjugated molecule	Source	Dilution	Reactivity	Use
Alexa Fluor® 488	Invitrogen A32723	1:1000	goat anti mouse IgG	ICC/IHC
Alexa Fluor® 488	Invitrogen A11034	1:1000	goat anti rabbit IgG	ICC
Alexa Fluor® 568	Invitrogen	1:1000	goat anti chicken IgG	IHC

Conjugated molecule	Source	Dilution	Reactivity	Use
	A11041			
Alexa Fluor® 568	Invitrogen A11011	1:1000	goat anti rabbit IgG	ICC/IHC
Alexa Fluor® 568	Invitrogen A11036	1:1000	goat anti rat IgG	ICC
Alexa Fluor® 514	Invitrogen A31558	1:500	goat anti rabbit IgG	IHC
Alexa Fluor® 647	Invitrogen A21450	1:500	goat anti guinea pig IgG	ICC/IHC
Alexa Fluor® 647	Invitrogen A32733	1:500	goat anti rabbit IgG	ICC

Table 2 List of secondary antibodies

Tabular list of secondary antibodies used in the thesis. ICC: immunocytochemistry; IHC: immunohistochemistry.

5. 3. Cell culture and transfection

Briefly, all the primary hippocampal neuronal cultures were prepared from E18 embryonic C57/BLRj mice using the previously described protocol (188) with certain modifications. The culture transfections with calcium phosphate precipitation method were conducted after 7 to 9 days in vitro, which are then fixed and immunostained or used for time-lapse imaging under live condition after 24 hours of plasmids' expression. The collected fixed images and time-lapse images through confocal microscopy were used for the afterward morphology and motility analysis respectively.

Before the culture preparation and transfection, a number of solutions need to be prepared and sterilized before experiment day:

➢ **70 % ethanol**, diluted by milliQ water

➢ **0.1 % polyethylenimine (PEI)**, diluted by sterile water

➢ **Dissection solution:** HBSS w/o Ca^{2+}, Mg^{2+}; ice cold

➢ **7.5% BSA**, prepared in PBS

➢ **Digestion solution:** papain enzyme (100 units per ml, Worthington, Biochemical Corp.), prepared in Neurobasal medium®

➢ **Seeding medium:**

1. 1% B27®

2. 1% Horse serum

3. 1% Glutamax®

4. 0.5% Pen/Strep (10,000 units/ml)

5. Neurobasal medium®

➢ **Feeding medium:**

1. 2% B27®

2. 1% Glutamax®

3. 0.5% Pen/Strep (10,000 units/ml)

4. Neurobasal medium®

5. 3. 1. Preparing of coverslips

Working under the fume hood, certain amount of Ø 12mm # 1.5 glass coverslips were immersed by 37% HCl in Erlenmeyer flasks, in which the flask bottom area with the given volume is large enough for all the coverslips to spread well and get contacts with HCl. After a total immersion time of at least of 2 hours in room temperature (RT) on a shaker, HCl was removed and the coverslips were flushed first by tap water for 3 minutes continuously. Then, coverslips were rinsed with the following reagents sequentially: milliQ water, 70% ethanol (diluted from 99% ethanol with milliQ water), 99% ethanol. Each rinsed for 5 minutes 3 times. The cleaned coverslips were then stored for long-term as soaked and sealed in a sterilized glass bottle containing certain amount of 99 % ethanol. Before the dissection day, under the cell culture hood, the coverslips were transferred as leaned against the wall of each well into 24-well plate piece by piece with clean forceps. Soon, the plate without lid was left in the cell culture hood for about 1 hour and then shaken slightly with the

lid on to let the coverslips fall down and cover the bottom of the plate horizontally when the coverslips were entirely dried. 24-well plate containing coverslips can then be kept back into its package and sealed at 4 °c for the later use.

5. 3. 2. Coating of coverslips and/or Petri dishes

Firstly, the coating solution 0.1 % polyethylenimine diluted by sterilized water was prepared and sterilized through 0.22µm filter. The day before the culture preparation, depending on the usage of the culture, certain volume of 0.1% PEI is added into each well or dish to immerse the bottom surface of the vessels completely. PEI was removed after about 2 hours of incubation under cell culture hood, plates or dishes were rinsed 3 times by sterilized water before replaced by distilled PBS in the end. Coated plates or dishes containing PBS were then placed into the incubator at 37 °C for the coming culture preparation day. At the preparation day, the PBS in the wells or dishes was replaced by certain volume of seeding medium at least one hour before the seeding of the dissociated neurons. Then the plates or dishes were kept back into the incubator and ready for use.

5. 3. 3. Dissection of embryonic hippocampi

All the required dissecting instruments have to be sterilized at 180°C for one hour before dissections:

- ➢ 2 dissecting scissors

- ➢ 2 dissecting tweezers

- ➢ 1 spatula rounded tip

- ➢ 1 microdissecting scissors

- ➢ 2 microdissecting tweezers with 45° angled tip

The dissection area needs to be sprayed with 70 % alcohol before using. Except for dissection solution which has to be ice cold during the entire session of dissection, the digestion solution and seeding medium have to be pre-warmed at 37°C water bath before the experiment.

Pregnant mouse (E18) was euthanized by isoflurane anesthesia followed by cervical dislocation. Then, the mouse's abdomen was disinfected by a spray of 70 % ethanol and opened up to expose the uterus by sterile dissecting scissors and tweezers. All the embryos inside of amniotic sac were removed and transferred into sterile 100 mm × 15 mm Petri dish.

Embryonic mice were then taken out from amniotic sacs and euthanized by decapitation, and the embryonic heads were placed into another new sterile dish containing ice-cold dissection solution.

By using dissecting tweezers, the embryonic mice heads were held and the whole brains were then exposed by cutting along the midline of the scalps using microdissecting scissors (Figure 9A-C). Then, the brains were carefully shoved out of the skull by spatula with a round end and placed into another new dish with ice-cold dissection solution.

With one microdissecting tweezer positioned at the cerebellum to hold the brain, the cerebral hemispheres were separated by carefully nudging them away from the midbrain. Holding the cortex with microdissecting tweezers, the meninges were then gently peeled off from the edge of the cerebral hemisphere on the lateral side to the inner side edge, where the hippocampus was located. After cleaning away the meninges thoroughly, the hippocampus was then dissected out from the cerebral hemisphere using microdissecting scissors (Figure 9D-E) and collected in Ø35mm Petri dish with ice-cold dissection solution.

5. 3. 4. Dissociation of hippocampal neurons

All the hippocampal tissues were pipetted into 50 ml conical tube and rinsed with certain volume of dissection solution. Later, when the hippocampal tissues settle at bottom of the tube, the pre-warmed digestion solution (2 ml) was added into the tube after removal of supernatant. The tissues were then incubated inside of a thermos mixer at 37°C for 20 minutes (Figure 9G, H).

After 20 minutes, under the cell culture hood, the conical tube containing the digested hippocampal tissues was kept in rest for 3 minutes to settle the tissues at the bottom. Soon the digestion solution was replaced by 2 ml of fresh seeding medium. By using 1 ml size of pipette tips (blue tips), the digested tissues with the medium were

triturated through pipetting in and out about 30 times while avoiding introducing air bubbles into the medium. A total of 3 times of trituration were required, each time after trituration followed by 2 minutes of settling time, the supernatant containing the dissociated cells were pooled into another conical tube.

After rinsing the 40 µm cell strainer with 1 ml fresh seeding medium, the collected cell suspension was strained through the cell strainer to remove some large undigested tissue clumps. In order to get rid of the cell debris generated during trituration for a homogenous cell suspension, the strained cell suspension is aliquoted evenly into several 15 ml conical tubes (usually one tube per 4~6 hippocampi). Then, the same amount of pre-warmed 7.5% BSA with higher density was pipetted carefully beneath the layer of cell suspension for each tube. With a centrifugation of 1000 rpm for 5 minutes at RT, the supernatants containing the cell debris were carefully aspirated. All cell pellets were then resuspended by seeding medium and pooled into another conical tube.

5. 3. 5. Seeding and maintaining of neuronal culture

The dissociated hippocampal neuron density was determined by using a hemocytometer with trypan blue solution. Depend on the size of surface area of different vessels and experimental approaches, which serve for different purpose of the experiments, the dissociated hippocampal neurons were seeded into wells or dishes either with high density ~12000 cells/cm^2 for culture transfection or low density ~6000 cells/cm^2 for the routine immunostaining of neuronal culture. Cell suspensions with specific cell concentrations were added into the vessels dropwise in order to acquire a relatively homogeneous distribution of neurons on the coated substrate surfaces. For long-term maintaining of the culture, half of the medium was replaced every 2 or 3 times a week by feeding medium. Considering of evaporation of the medium, a small volume ~ 20 µl of medium was compensated each time for medium change.
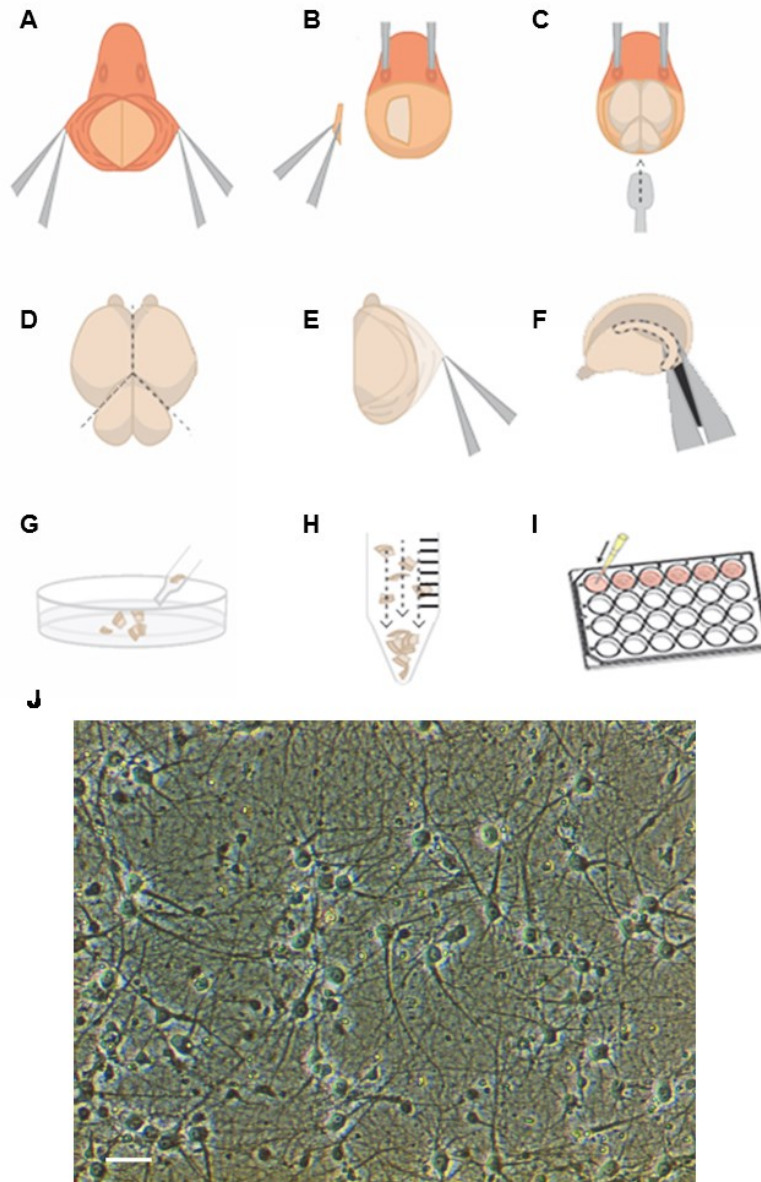
Figure 9. Hippocampal neuronal culture preparation

(A) The scalp of the sacrificed mice embryos was opened by forceps and scissors. **(B)** Bone fragments of skull were removed to expose the whole brain. **(C)** The brain was lifted and removed using a small spatula angled beneath the brain. The brain was placed in a petri dish containing ice-cold fresh dissection buffer. **(D)** After rinsing with cold fresh dissection buffer, under dissecting microscope, the freshly isolated brains were separated into two hemispheres. **(E)** Meninges were carefully peeled away from the outer surface of the hemisphere. **(F)** Hippocampi were isolated from the inner edge of cortices and collected into another petri dish with ice-cold dissection buffer. **(189)** Under laminar flow hood, all collected tissues were transferred into 50 ml conical tube, the dissection buffer was then aspirated from the tube. The prepared enzyme solution was then added for digestion. **(I)** After incubation and trituration of the tissues into the cell suspension, the dissociated neurons

were seeded into coated plate or dishes with corresponding cell density. **(J)** Phase contrast image of cultured dissociated hippocampal (10 days in vitro). Note well-developed network of neurites. Scale bar: 20μm.

5. 3. 6. Transfection of primary neuronal culture

The cultures were transfected using the calcium phosphate precipitation method at DIV 7 to 9 as described before (190) with slight modifications regarding the reaction volume.

Before transfection, several solutions were required for the precipitation of calcium phosphate in the neuronal culture:

> ➢ $CaCl_2$ (125mM);

> ➢ 2x HBS solution: 137 mM NaCl, 4.75 mM KCl, 7.5 mM glucose, 21 mM HEPES, 0.7 mM Na_2HPO_4, pH is adjusted to 7.05;

> ➢ Plasmids with determined concentrations.

> ➢ Sterile water for adjusting total volume

Specifically, at the transfection day, the medium in the culture was replaced by fresh feeding medium to incubate for at least 20 minutes before adding the reaction volume for transfection. The reaction volume has to be prepared freshly on the day before the transfection. Depends on the different requirement of the plasmids designed for the transfection experiment, the exact volume of each solution constituted for the reaction volume has to be calculated precisely every time for the experiment. Moreover, because of the different concentrations of different plasmids amplified previously, sterile water was used to adjust the final reaction volume to the exact total reaction volume for each culture target of transfection.

Take transfection for 4 wells in 24-well plate for example, 27.5 μl of transfection volume was required for each well containing 500 μl of medium, thus a total of 110 μl reaction volume had to be prepared before the experiment. To prepare a 110 μl total reaction volume, 55 μl of 2x HBS was aliquoted into a sterile EP tube, adjusted volume of sterile water, 6.88 μl of 125 mMCaCl₂ and calculated amount of plasmids (6~12 μg in total) were mixed with a total volume of 55 μl into another clean tube. To

maximize the mixing of the two tubes of solution, each time 1/8 volume of 2x HBS solution was added into the solution Ca^{2+}/DNA mixture step by step followed by 8 seconds of vortexing. After mixing, the final 110 µl reaction volume was incubated at RT for 15 minutes, and then can be added into the 4 wells with a volume of 27.5 µl for each one. After one hour of incubation at 37 °C, the transfection mixture was then washed out of the culture using pre-warmed HBSS before the culture continues the daily maintaining.

5. 4. Immunofluorescence and microscopy

In principle, immunohistochemistry was conducted for the analysis of GABAergic synapse at the AIS of hippocampal neurons, which include mouse perfusion, brain frozen section preparing and the immunofluorescent staining to visualize the synapsed located at the AIS in vivo; while immunocytochemistry was implemented for the various morphological analysis of neuronal compartments at the subcellular level.

5. 4. 1. Preparation of mouse brain sections

First, mouse perfusion was completed with the help from colleague Corinna Corcelli in our laboratory. Briefly, Thy-1 GFP transgenic mice were shortly anesthetized by isoflurane and then perfused with cold NaCl (0.9 %) and PFA (2%) for 5 minutes in between with ventricular perfusion method. The brains were then taken out from the heads after perfusion, and immersed in a serial of sucrose with ascendant concentrations from 5 % to 30 %, each concentration of sucrose immersing overnight to dehydrate the brain tissues gradually. The dehydrated brain tissues were then frozen by liquid nitrogen rapidly with embedding media into a home-made plastic cubic container with a proper size.

Before the immunostaining of tissue or cell culture, **blocking buffer** (1% BSA, 0.2% fish skin gelatin, 0.1% Triton X-100) has to be prepared sufficiently beforehand.

5. 4. 2. Immunohistochemistry

With equipment cryostat, the brain tissues were sliced on coronal planes including areas of hippocampus with a thickness of 12 µm and mounted onto the glass slides. Then, the brain sections were rinsed in PBS and the residual liquid was removed from the slides by a self-made vacuum pump. A special marking pen was used to

draw a hydrophobic circle around the brain sections on the slides to keep the liquid pooled in a single droplet. After that, the sections were blocked and permeabilized with the blocking buffer for one hour, usually ~100 µl for each section, followed by PBS washing. After preparing the antibody incubating solution (antibodies diluted proportionally by the blocking buffer), the tissues were incubated overnight for primary antibodies and one hour for secondary antibodies, each followed by PBS washing. Then cover glasses were then mounted on the surface of the tissues containing drops of immersion medium before a short drying of the slides with a vacuum pump. The immunostaining slides were then ready for imaging after a couple of days of the medium hardening. All immunostaining procedures were performed at RT and with PBS washing (5 minutes, repeat for 3 times) of the slides between each step.

5. 4. 3. Immunocytochemistry

Neuronal cultures grown on glass coverslips were fixed 24 hours after transfection by pre-warmed 4% paraformaldehyde (PFA) in PBS for 10 minutes, followed by one hour combined blocking and permeabilization step with blocking buffer. Cells were then incubated in primary antibodies overnight and secondary antibodies for another one hour. The coverslips with the stained neuronal cultures were shortly rinsed in ddH$_2$O and then mounted upside down onto glass slides with immersion medium. All immunostaining procedures were performed at RT and with PBS washing (5 minutes, repeat for 3 times) of the coverslips between each step.

5. 4. 4. Confocal imaging

Confocal images were collected using a Nikon 90i upright microscope mounted with Plan Apo 100×/1.45 NA oil objective (Nikon). Argon 488 nm and He 543 nm 633nm laser lines were used. Each image focused on one neuron in the center with good signal to noise ratios for all channels. Imaging parameters include 1024*1024 pixels, fixed 0.08 µm pixel size, z-stacks with 4-7 µm depth and 0.3 µm scanning thickness. STED imaging of neuronal PO, mitochondria, and ER in neurites were completed with the instruments and technique support of Drs. K.H. Körtje and D. Schroth, Microsystems CMS GmbH, Mannheim.

5. 5. Time-lapse imaging of neuronal PO and mitochondria

In general, time-lapse imaging is used to analyze the motility of neuronal PO and mitochondria in response to ACBD5 expression, which could interfere with the organelle contacts between PO and ER in this study. Specifically, neurons cultured in Ø35 mm imaging dishes with polymer coverslip bottom compatible for laser scanning were co-transfected at DIV 7 to 9. Cultures were divided into two groups. One was transfected by fluorescent PO marker EGFP-SKL, the mitochondria marker mCherry-Mito-7 and with myc-ACBD5 while the other group was transfected without the latter plasmid. Because the expression of myc-ACBD5 without any fluorescent tag in the culture cannot be visualized under live conditions, a pre-experiment to evaluate the efficiency of the co-transfection of myc-ACBD5 with the other two plasmids was conducted (Figure 17). Immunostaining by anti-myc, anti-GFP and anti-RFP on the fixed culture 24 hours after transfection with the 3 kinds of plasmids was performed. The results showed that co-expression efficiency of EGFP-SKL, mCherry-Mito-7, and myc-ACBD5 was quite considerable as 80~90% of transfected neurons carried all 3 kinds of expression from the plasmids, which made the analysis of PO motility with myc-ACBD5 overexpression feasible under live conditions.

For each Ø35 mm imaging dish 55µl of transfection mixture was used containing the different DNAs with an equal ratio. After 24 hours of expression, neurons were imaged using Leica SP5 inverted confocal microscope equipped with 63×/1.4 oil objective (Leica) and resonance scanner to provide a scanning speed up to 8000 Hz. Physiological environment was also controlled with temperature 37°C, gas: 95% O_2, 5% CO_2, and humidity supplied. Argon 488 nm and He 561 nm laser lines were used during the imaging session. Time-lapse images focus on each individual transfected neuron with two channels were simultaneously acquired every 4 seconds with 1024*1024 pixels, z-stacks of about 4~6µm with 0.4µm step size, and a total imaging time for about 8 minutes. A maximum imaging time for each dish was controlled under half an hour for the sake of culture viability.

5. 6. Morphological analysis

Morphological analysis in this study includes the measurement of GABAergic synapses and CO located at the AIS, cellular distribution of neuronal POs. All the analysis was based on confocal images with high resolutions of fixed immunofluorescence staining of hippocampal brain sections or neuronal cultures.

5. 6. 1. Measurement of GABAergic synapses

After confocal imaging of hippocampal sections stained by antibodies against VGAT, $GABA_ARα2$, β4-spectrin, and GFP, the documented z-stacks of images were deconvoluted in 3D by using AutoQuant X3® model of Imaris® software to optimize the visualization of synaptic components at the AIS of individual neurons. With correctified optic parameters settings for each confocal image, the 3D deconvolution was carried out with the major parameter settings including a selection of theoretical PSF (point spread function) and 20 times of iterations. After deconvolution, the quality improved images were then transported into Imaris® software to start the 3D reconstruction of the synapses at the AIS and its surrounding areas. In principle, the procedure of the reconstruction was conducted following the instructions of surface reconstruction function of the software including local background subtraction, various adjustments of different thresholding values and removing irrelevant objects from the final reconstructed images. To evaluate the number of synapse at the AIS, a criterion to identify a synapse was made for this study as follows: 1. At least half volume of a single $GABA_ARα2$ object is situated inside of the AIS volume; 2. $GABA_ARα2$ objects should be contacting the surface of the AIS and cannot be completely embedded inside of the AIS; 3. VGAT objects should have a comparable size with the contacting $GABA_ARα2$ objects; 4. The two reconstructed synaptic objects should be close enough that the overlapping volume of the two must be considerable for a tight binding. Eventually, the reconstructed component of GABAergic synapses together with reconstructed volumes of the AIS and part of neuron were verified and the numbers of synapses were counted for a comparison between AcD and nonAcD neurons in hippocampus.

5. 6. 2. Cisternal organelle measurements in AIS

Neuronal culture at different developing stages (DIV7, 14 and 21) was fixed to visualize CO in the AIS of primary hippocampal neurons by immunostaining of SP (CO marker), β4-spectrin (AIS marker) and MAP2 for the morphology of neuron on the cultures, and later imaged through confocal microscopy. All the images neurons were divided into AcD and nonAcD groups both including 15 neurons at the different stages according to their different AIS origins. A few steps of pre-processing in ImageJ, which include brightness/contrast and contrast enhancement to facilitate the following segmentation for CO and AIS in each channel, were conducted before the

measurements. To begin the analysis of CO development in the AIS, the total volume (area, μm^2) of AIS was measured first for each neuron. Later, with the outline of AIS volume, all the segmented SP puncta outside of the AIS outline were removed from the SP channel, and then the number and area of SP puncta of the given AIS can be measured and documented. Self-written plugin codes in ImageJ macro language (Script 1, included in Appendix) was used to implement all above mentioned analysis procedures. The number and area of CO and AIS of each imaged neuron were documented separately for the comparison between AcD and nonAcD groups.

5. 6. 3. PO distribution measurements

Neurons co-expressing EGFP-SKL or myc-ACBD5 as PO marker and cytoplasmic mCherry used to track the neuron morphology were immunostained with anti-GFP, anti-myc and anti-RFP antibodies, respectively. Moreover, to visualize the total PO in the culture as a positive control, anti-Pex14 as a generally applied peroxisomal marker was used to complete a triple-labeling of the culture. After the confocal imaging, the collected images including 59 imaged pyramidal-type neurons for the EGFP-SKL control group and 77 for myc-ACBD5 group were pre-processed including brightness/contrast adjustment and background subtraction to facilitate the upcoming channel segmentation by Fiji (ImageJ, National Institutes of Health). The neuron soma area was first delineated manually then subtracted from the thresholded and segmented mCherry channel which defined the focused neuron area to obtain the neurite area outline from the image. Subsequently, the segmented PO particles were determined within the outlined soma and neurite area respectively. A semi-automatic user-defined plugin written by ImageJ macro language (Script 2, included in Appendix) was used to implement all above mentioned analysis procedures. The number and area of POs of each imaged neuron including soma and neurite area were for comparison documented separately for the two groups.

5. 7. Motility analysis

Motility analysis in this study include the analysis of PO and mitochondria movement in the neurites in response to ACBD5 expression in cultured hippocampal neurons, among which the measurement of mitochondria motility and customized image analysis source codes in Python was completed with the tremendous help from Josiah Passmore, Jeremy Metz etc. from University of Exeter, UK.

PO and mitochondria motility measurements

After 24 hours of expression, two cell culture groups that were co-transfected by EGFP-SKL and mCherry-Mito-7 with and without myc-ACBD5 were imaged under live conditions. Neurons that co-expressed EGFP-SKL and mCherry-Mito-7 emitting the fluorescence with acceptable intensity were selected for time-lapse imaging. A total of 20 neurons were collected for each group. The images were then brightness/contrast adjusted individually by Fiji image software. The neurites where the POs located relatively sparsely were preferentially used to generate kymographs for the PO motility analysis. The trajectories of the detected PO and mitochondrial movements were obtained first by adding up all the frames of each time-lapse image, through which segmented line tools were used to draw lines along the neurites to cover the organelle trajectories. The line width was adjusted to cover the maximum size of the organelle in the neurite of interest. Next, kymographs were generated from the line-selected neurites by kymograph plugin using Fiji (ImageJ, written by J. Rietdorf and A. Seitz). After image enhancing and inverting of the kymograph, segmented line tool was used to draw lines along the intensity lines, which represent the excursions of either static or moving POs in the time space. Velocities and traveled distances of the captured organelles were read out through these lines by using a slightly modified version of the ImageJ "velocities" macro from the plugin above. The contacts of PO and mitochondria were counted only in neurite area manually by using the similar method as described for PO distribution analysis. All the first frames of each time-lapse image were collected for the analysis. First, the soma area of each neuron was delineated and removed from both PO and mitochondria channels. Then the two channels indexed by distinct colors were merged after thresholding with Otsu method and binarizing. The total number of POs and POs that are free from mitochondria were measured respectively. The compiled data, absolute number of POs that contact mitochondria (Total number of POs minus PO without contacts with mitochondria), % of PO-mitochondria contacts, were then used for the comparison between the two groups.

To generate more objective quantitative data on the PO statistics and mitochondria motility analysis, a custom image analysis pipeline written in Python (written by Josiah Passmore, Jeremy Metz etc. from University of Exeter, UK) was used. In brief, neurons were segmented from the maximum projection of both channels (PO and mitochondria) and all time points of data. This was done by first running a multi-scale

Frangi ridge filter (191) over the image, followed by non-maximal suppression, double threshold, and hysteresis tracking; in this way the neurite tracing algorithm can be seen as a modification to the standard Canny edge detection algorithm (192), adapted to detect ridges. Once the neurites have been detected using the aforementioned approach, a scale-space Difference of Gaussian filter (193) was applied to detect the soma, identified as the largest detected object, was subtracted from the neurite mask to avoid detecting POs in the soma region. Using the neurite masks obtained from the neuron segmentation, detection of the organelles was a greatly simplified task and was achieved by blurring each frame with a Gaussian filter (sigmas 1 and 2 for PO and mitochondria respectively). Next, an automated threshold was calculated using Otsu's algorithm applied to only filtered pixel values with the neurite mask region. This threshold was used to binarize the image into organelle and non-organelle regions. Lastly, these regions were grouped using a connected component labeling algorithm. The detected organelle regions were then tracked using a global nearest neighbors algorithm applied to centroid positions, which links nearby objects in adjacent frames in a globally optimal manner. These linked object positions, or trajectories, were the basis of all subsequent analysis. Each PO's and mitochondria's maximum and average speeds (µm/s), total traveled distance (µm), as well as the net traveled distance (µm) were collected for each group and compared between the two groups. Furthermore, the movements of POs and mitochondria were assigned to three categories according to the different traveled distances over the entire imaging session of each organelle: static (< 5 µm), short-range movement (≥ 5µm, < 10µm), long-range movement (≥ 10 µm). The percentages of PO and mitochondria with different types of movement were compared as well.

5. 8. Statistical analyses

To determine the statistic difference of measured data between AcD and nonAcD group, or ACBD5-transfected and control group, unless otherwise mentioned, one-tailed, unpaired t-test was used as major analysis method (*$P < 0.05$; **$P < 0.01$; ***$P < 0.005$; ****$P < 0.001$; ns: not significant) in SigmaPlot®. Sample sizes of different kinds of data were indicated under the corresponding data collecting methods. All the quantitative data were collected from at least three independent experiments and presented as mean ± S.E.M.

6 RESULTS

6. 1. Different distributions of GABAergic axoaxonic synapses at the AIS of AcD and nonAcD neurons in hippocampus

Since the axon-carrying dendrites from hippocampus produce output action potentials at a lower threshold as compared to at soma (33), the distribution of GABAergic synapses at the AIS of AcD and nonAcD neurons might reflect this discrepancy of electrophysiology properties. To test this hypothesis, immunofluorescence staining on the hippocampal brain sections of transgenic mice with a Thy1-GFP construct were conducted to quantify the number of GABAergic synapses at the AIS of each type of neurons **(Figure 10)**. As shown in **figure 10(A-E, H-L)**, the immunofluorescence images with four different markers were acquired and pre-processed first to facilitate the three-dimensional recreation of GABAergic synapses in the AIS of the corresponding neurons. Those identified GABAergic synapses at the AIS in surface-created 3D view **(Figure 10F, G, M, N)** were then counted manually and recorded for the subsequent comparison between AcD and nonAcD neurons. Slightly increased GABAergic synapse number was detected in those AcD neurons, which was 19 ± 1.17 synapses, while 14.8 ± 1.51 synapses locates at the AIS of nonAcD neurons **(Figure 10O)**. Such differentially distributed GABAergic synapses at the AIS implying a relatively enforced inhibitory control on those AIS origin from dendrites.
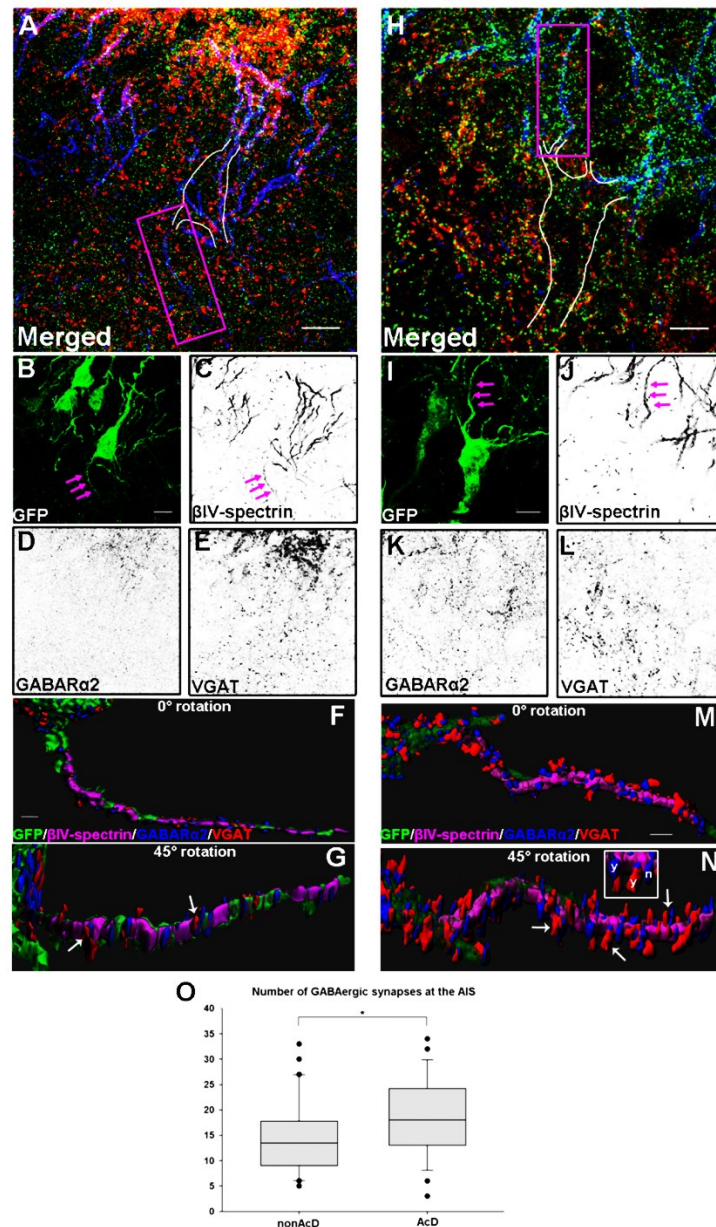
Figure 10. Quantitative distribution of GABAergic axoaxonic synapse at the AIS of AcD vs. nonAcD neurons in hippocampus

Immunofluorescence confocal images of nonAcD (A-E) and AcD (H-L) neurons in hippocampus of Thy1-GFP transgenic mice. Neuron morphology was presented in GFP-expressing as shown in (B, I. green) with arrows indicating the location of AIS, which was marked by β4-spectrin in (C, J. gray). Assembled GABAergic synapses were marked by clustering of $GABA_ARα2$ (green in A and H, gray in D and K) and VGAT (red in A and H, gray in E and L). Note that the somas and proximal neurites were outlined with white lines in A and H, and the whole AIS and surrounding areas were enclosed with magenta rectangular boxes which were cropped afterward for the 3D recreations (F, G, M, N) in Imaris software®. Scale bar: 10 μm. (F, M): Surface recreated proximal parts of nonAcD neuron (green, F, G)

and AcD neuron (green, M, N), AIS (magenta), AIS-located $GABA_ARα2$ (blue) and $GABA_ARα2$-binding VGAT (red). Scale bar: 2 μm. (G, N): Rotated view of about 45° in x-z plane from (F, M) displayed a few numbers of verified synapses (arrows). Inset in (N) exemplified two verified synapses (y, binding of blue and red surfaces) and one non-synapse (n, blue surface only). (O): Box plots of GABAergic synapse numbers at the AIS of nonAcD and AcD neurons. Significance test showed an increased number of GABAergic synapses in AcD neurons (n = 26) compared to nonAcD neurons (n = 40), one-tailed t-test, *p* = 0.014.

6. 2. Maturation of CO in the AIS of AcD and nonAcD neurons

A certain number of specialized stacked ER referred to as cisternae organelles (CO) locate in the AIS. Although still little is known about how is this organelle formed and matured, several studies have suggested that CO is involved in Ca^{2+} regulation and locates in proximity of GABAergic receptors in the AIS which may regulate GABA α receptor activities and AIS plasticity (48, 50, 82, 194). Synaptopodin (SP), an actin-binding protein, which is essential for the COs' establishment, usually is used as a marker for COs in the AIS. Considering its AIS excitability relevance, the analysis of CO number and volume in the AIS of nonAcD vs. AcD neurons during the development of cultured hippocampal neurons, was implemented to examine whether there is a difference of CO maturation between nonAcD and AcD neurons. To do so, the COs in the AIS of cultured hippocampal neurons at DIV7 (Figure 11A, B), DIV14 (Figure 11C, D) and DIV21 (Figure 11E, F) were detected by SP (79) co-stained with β4-spectrin (red) and MAP2 (blue) for AIS and neuron visualizations respectively (Figure 11A-F). After confocal image acquisition and pre-processing, imaged neurons were grouped into nonAcD (Figure 11A, C, E) and AcD neurons (Figure 11B, D, F) which were then analyzed separately. As shown in Figure 11G-I, there was no significant difference in SP volume or the ratio of SP volume to AIS volume (area) between nonAcD and AcD neurons at different stages of the AIS. Only an increase in the AIS volume (37.6 ±1.98 $μm^2$) of AcD neurons compared to that of nonAcD neurons (31.7 ± 1.57 $μm^2$) was detected with significance indicating a larger volume of AIS in matured AcD neurons (Figure 11G). In figure 11J-L, nonAcD and AcD neurons were combined together for each stage of development to compare the maturation of CO in the AIS of cultured hippocampal neurons in general. The analysis results showed, that AIS volume increased from 27.86 ± 1:42 $μm^2$ at DIV7 to 40.67 ± 1:9 $μm^2$ at DIV14 and then slightly dropped off to 34.69 ± 1:33 $μm^2$ at DIV21

(Figure 11J), while CO volume in the AIS surged from $0.04 \pm 0.01 \mu m^2$ at DIV7 to 3.28 $\pm 0.57 \ \mu m^2$ at DIV14 and then stay stable at a similar level at DIV 21 (Figure 11K). With the percentage of CO volume in the AIS, results also showed a sudden rise from $0.14 \pm 0.05\%$ at DIV7 to $7.14 \pm 1.1\%$ at DIV14 and then developed into DIV21 with only small fluctuations (Figure 11L). Visualization of CO in the AIS also displayed a trend of elongation longitudinally of the organelle in this particular neuronal compartment during developments (arrowheads in figure 11C-F). Taken together, the analysis of CO maturation indicated a late development of CO in the AIS. Specifically, CO begins to be established in the AIS of cultured mouse neurons after one week of growing and reaches to the maximum level within one week. Then the volume of CO is stabilized with a slight decrease at the third week thus comes to a maturation stage.
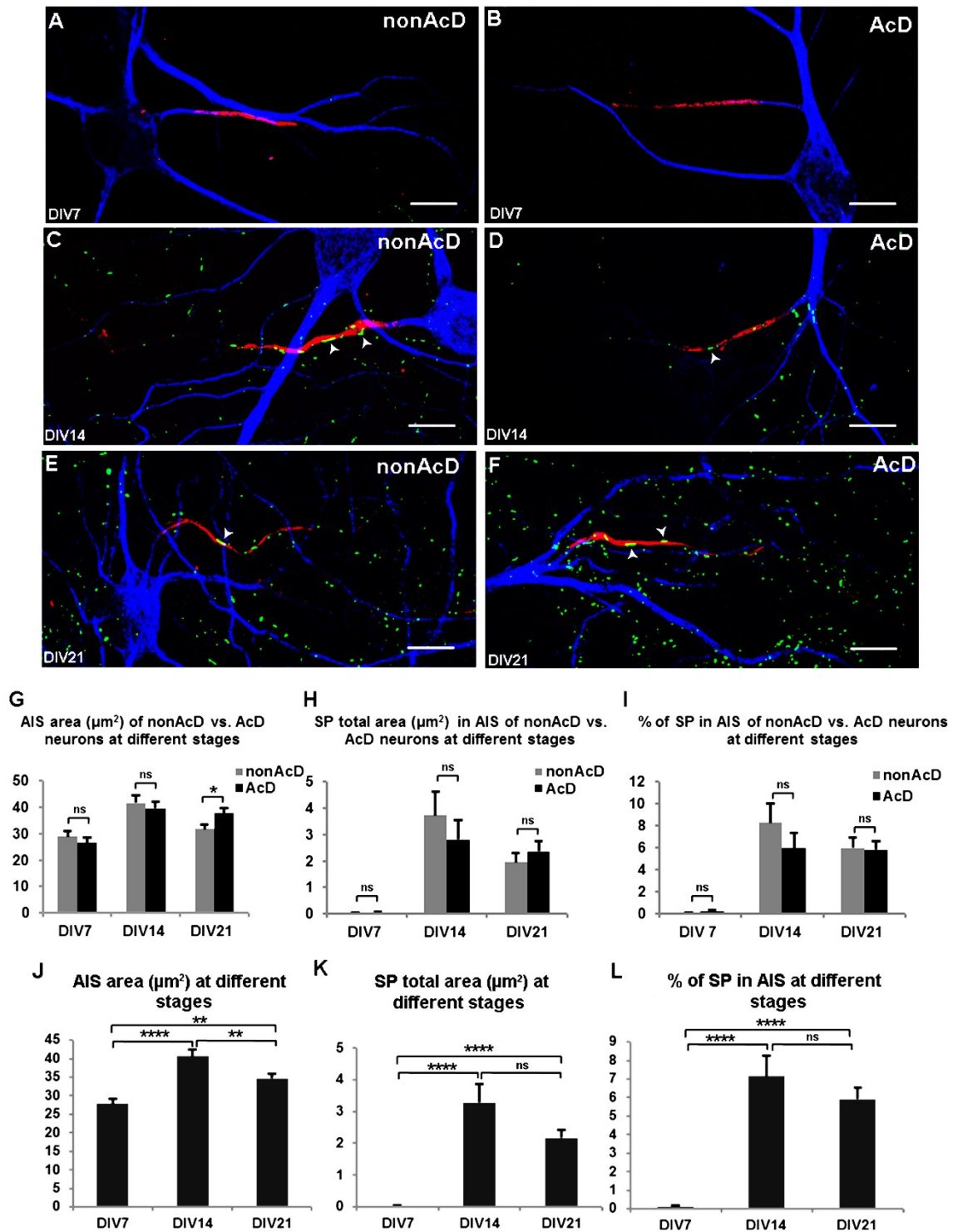
Figure 11. Maturation of CO in AIS of AcD and nonAcD neurons

Confocal images of nonAcD neurons (A, C, E) and AcD neurons (B, D, F) at DIV7 (A, B), DIV14 (C, D) and DIV21 (E, F). Neurons were immunostained by synaptopodin (SP; green), β4 spectrin (red) and MAP2 (blue). Arrowheads in (C-F) denote the elongated SP in the AIS as compared to SP in dendritic spines. Comparison of AIS area (μm^2) (G), SP total area (μm^2) (H) and percentage of SP in the AIS (I) between nonAcD and AcD neurons at DIV7,

DIV14 and DIV21. Comparison of AIS area (µm2) (J), SP total area (µm2) and % of SP in the AIS of combined nonAcD and AcD neurons at different developing stages. *: p < 0.05; **: p < 0.01; ****: p < 0.001; ns: not significant. One-tailed t-test in(G). Mann-Whitney method in (H, I). one way ANOVA in(J-L).

6. 3. Association of CO with SERCA in AIS

After the study CO maturation in the AIS, the potential function of CO in the AIS was then tested. Relatively matured hippocampal culture at DIV19 were immunostained by antibodies against SP and SERCA (sarco/endoplasmic reticulum Ca^{2+}-ATPase), which pumps cytosolic Ca^{2+} into ER or sarcoplasmic reticulum. β4-spectrin was co-stained as well for the morphology of the AIS. Two representative confocal images were presented in Figure 12, showing that CO (79) was largely co-localized with SERCA (red) in the AIS. Such extensive co-localization of CO and SERCA in the AIS emphasized again that CO serves as Ca^{2+} storage places in the AIS.

Figure 12. Association of CO with SERCA

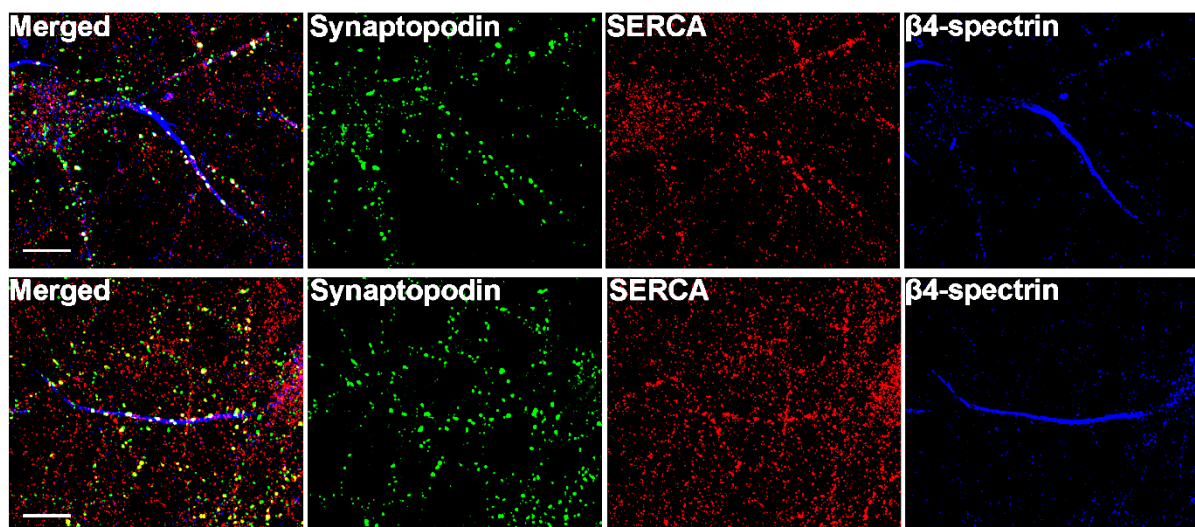Two representative confocal images of hippocampal culture immunostained by synaptopodin (SP, green), sarco/endoplasmic reticulum Ca^{2+}-ATPase (SERCA, red), and β4-spectrin (blue), with separated channels demonstrated on the right, respectively. Note that SP was highly co-localized with SERCA in the AIS (labeled by β4-spectrin). Scale bar represent 10 µm.

6. 4. Relationship of ER, mitochondria, and PO in neurons

The association between POs and ER, mitochondria can be intricate in terms of functioning and positioning, which is morphologically documented by close subcellular proximities implying the existence of physical contact sites between the different organelles (195, 196). A recent study in COS-7 cells using simultaneously expressed fluorescent marker for six subcellular compartments reported that > 90% of POs are in contact with the ER and around 20% in contact with mitochondria (197). Neurons with their long processes exhibit a highly specialized morphology and cellular polarity which require a tight control of the contacts between the main subcellular neuronal compartments and their distributions in neurons. To evaluate how neuronal POs distribute in relation to their major contacts with other organelles, two groups of cultured hippocampal neurons were co-transfected with plasmids expressing organelle marker proteins EGFP-SKL-PO and RFP-KDEL-ER, mPlum-Mito-3, respectively (Figure 13A, B). However, the high organelle density in the somatic area of the neurons significantly impedes light microscopy analysis of organelle contacts whereas the more flattened and extended morphology of the neurites allows the clear visualization of individual organelles (Figure 13C, E). As depicted in Figure 13D (enlarged rectangular area in Figure 13C), POs are regularly found embedded in a network of ER tubules in a confined space of neurites, making it unlikely to distinguish between real organelle contacts and merely arbitrary overlapped of fluorescent signals. Unexpectedly, a high proportion of PO was found in close proximity to mitochondria in the neurites (overview in figure 13B, arrowheads in Figure 13E,). Such contacts might reflect the functional relationship between these organelles, which e.g. have to exchange fatty acids generated in β-oxidation or their cooperation in the metabolism of reactive oxygen species (ROS) (90).
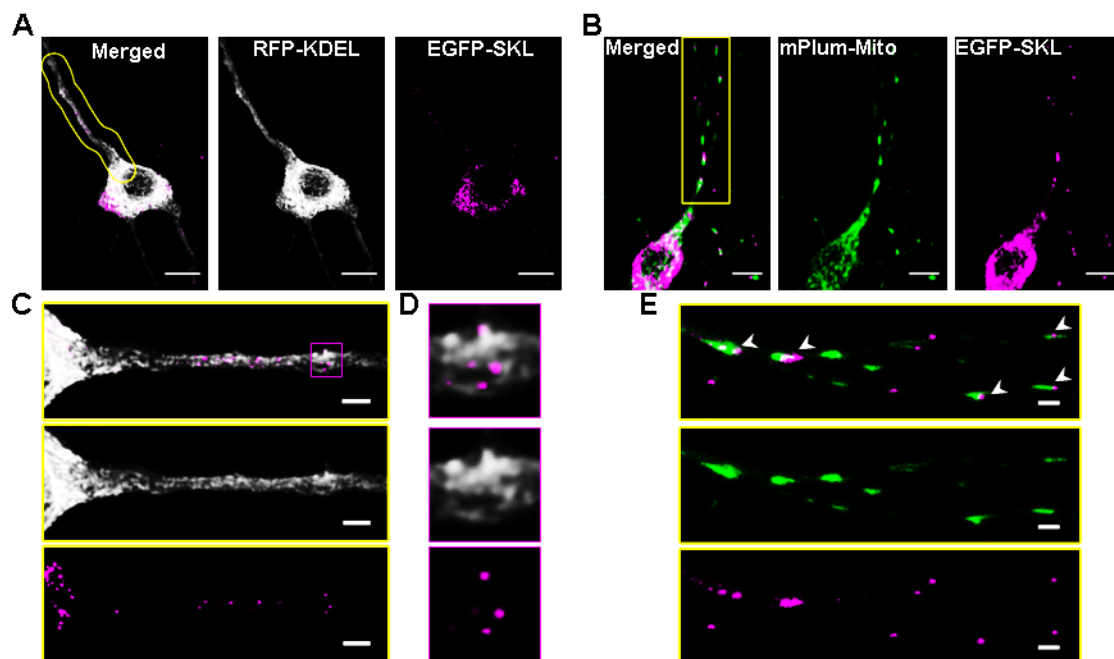
Figure 13. Peroxisomes are in close proximity to the ER and mitochondria in neurites of cultured neurons

(A) Confocal image of a fixed neuron with PO and ER marked by expression of RFP-KDEL (grey) and EGFP-SKL (magenta). Deconvoluted single plane from z-stack. Scale bars represent 10 µm. (B) Live confocal image of a neuron with PO and mitochondria marked by expression of mPlum-Mito (79) and EGFP-SKL (magenta). Maximum intensity projected from z-stack. Scale bars represent 10 µm. (C-E) Magnified and straightened areas outlined in yellow in A and B. (D) Magnification of magenta box in (C). Arrowheads in E indicate the close proximity of PO and mitochondria. Note that POs often appear in the close vicinity of the ER and mitochondria (Scale bars: 3 µm).

Since the resolution of conventional confocal microcopy (Figure 14B) could not distinguish that if these organelle proximities might be close enough to suggest real organelle contact sites (< 30 nm), STED microscopy was applied with a resolution of 20 nm/pixel using comparable sets of marker plasmids and antibodies. Unlike in conventional confocal microscopy, the fluorescent signals for the antibodies against Pex14 (a subunit of PO matrix protein import complex) and TOM20 (a subunit of the mitochondrial outer membrane import receptor) in STED or high resolution of confocal imaging do not represent the whole organelle structures but display the macromolecular organization of the organelle membranes. In this respect, Pex14 and the TOM20 fluorescent signals show the respective protein import complexes along

the organelle membrane of spherical or elongated membrane structures of POs and mitochondria, while the soluble ER marker RFP-KDEL distributed more homogenously inside the ER network (Figure 14A). Importantly, signals for Pex14 and TOM20 can be found in close proximities in the range of 20-40 nm (overview in Figure 14A, enlarged in Figure 14C, arrowheads and asterisks denoted the contact facets of POs and mitochondria). Therefore, the involved PO and mitochondrial membranes are situated in a distance which is characteristic for organelle contact sites (198). Similarly, the Pex14 and TOM20 signals are tightly surrounded by the dense ER network in the neurites of hippocampal neurons, implying physical contacts between the organelles. According to these observations correlating STED and confocal microscopy, it is concluded that the neurite regions of the hippocampal neurons principally not only allow the analysis PO motility and positioning but also monitoring their interaction with mitochondria and ER. It is therefore in this study focused on the neurite compartments of the hippocampal neurons, in order to investigate if the expression of the identified organelle combining structures like the ACBD5-mediated PO-ER tethering complex alters organelle communication networks and distributions in neuronal cells.
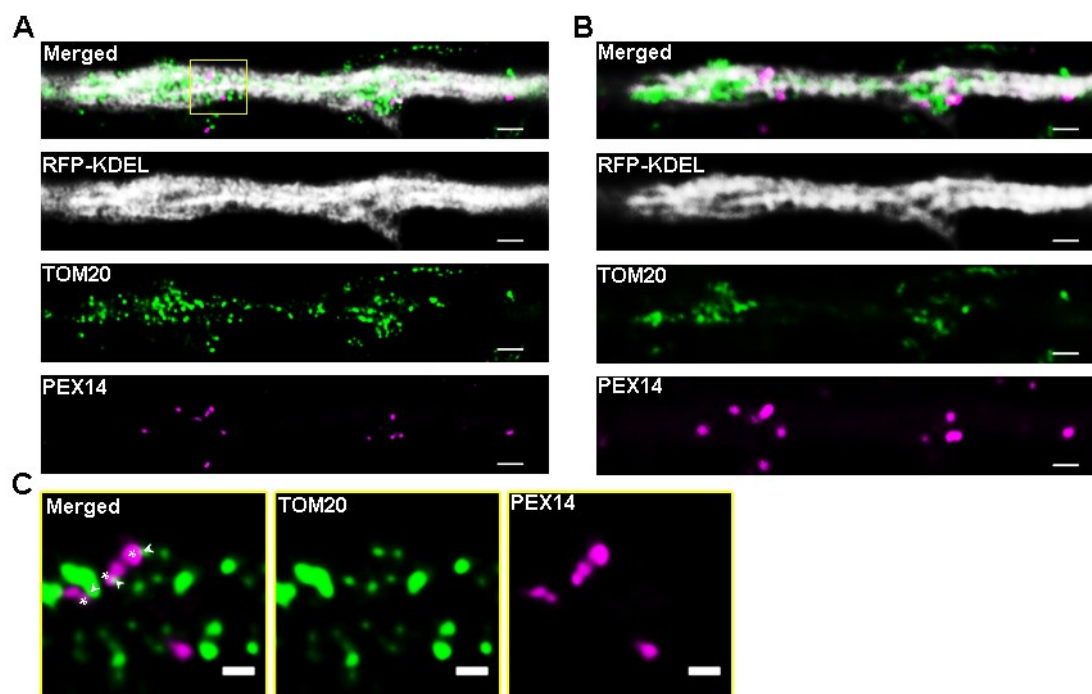

Figure 14. Comparison of STED and conventional confocal imaging and potential PO attaching to mitochondria.

(A) STED and (B) confocal image of the same length of neurite showing peroxisomal PEX14 (magenta) and mitochondrial TOM20 (79). The ER (grey) was marked by expression of RFP-KDEL plasmid (Scale bars: 1 µm). (C) Magnification of the area marked by a rectangle in (A), PEX14 (arrowheads) and TOM20 (asterisks) were labeled to display the extremely close proximity between the two. Maximum pixel resolution in the image is 20 nm, thus signals attached to each other are in the distance characteristic for organelle contact zones (Scale bar: 300 nm).

6. 5. POs and mitochondria exhibit comparable motilities in hippocampal neurons

The motility of POs, as described previously, is particularly important for subcellular positioning of POs in the extended dendrites and axons. Furthermore, the contacts of POs with other neuronal compartments influence profoundly the motility of POs. The newly identified PO-ER tethering partner ACBD5 has been studied, that expression of ACBD5 can alter the motility of POs in the non-neuronal cell such as fibroblasts. Based on this, the change of neuronal ACBD5 expression would be used to study the impact of PO-ER binding on the motility even the distribution of neuronal POs. To examine this, the movement property of PO and mitochondria in wild-type of cultured hippocampal neurons were first determined. To visualize PO and mitochondria movement in the neuronal culture, the primary hippocampal neurons at DIV7~9 were co-transfected with EGFP-SKL (PO marker) and mCherry-Mito (mitochondria marker) (Figure 15A). Then, the movements of PO and mitochondria in the transfected neurons were recorded about 8 minutes in a live condition. Subsequently, the velocities and traveled distances of POs and mitochondria in the neurites were determined by kymograph analysis. As exemplified by representative kymographs of neuronal PO and mitochondria (Figure 15B-D), PO generally showed no continuous movements and quite stable in one place. Most of the moving POs move in a very short range and change their moving direction very frequently shown as back-and-forth movements, and a few of them perform a restricted salutatory movement which could cover about 10 µm in 30 seconds and then again arrested (Figure 15B, C). Therefore, an averaged total traveled distance of those all analyzed neuronal POs during the recording time is relatively low value of about 5.57 ± 0.28 µm (Figure 16E) in the wild-type condition (WT). Comparing to POs, mitochondria appear to move more continuously along the neurites and show frequent fusion and fission events

(Figure 15D) although the averaged total traveled distance of mitochondria was found approximately 5 µm in the neurites as well (Figure 16F). As was described for other mammalian cells (113), according to their total travelled distance during the recording time, PO and mitochondria movements in the neurites were classified to static (moving distance < 5 µm), short-range movement (moving distance between 5 to 10 µm) and long-range movement (moving distance > 10 µm), which was applied to characterize the organelles' motility in this study. As were detailed in quantified and categorized PO and mitochondria movements through kymograph analysis (Figure 16A, B), with a proportion of 60.3 ± 7.3 % most POs did not show distinct moving but stayed at their original location, while short range and long range movements of PO constituted 30.2 ± 5.6 % and 9.5 ± 3.4 % respectively. Comparably, around 75 % of mitochondria were found to remain static, while 10 % and 15 % of mitochondria showed long and short-range respectively. Therefore, unexpectedly, the two organelles turned to show quite similar motilities with each other. Accordingly, it can be reasoned that the more dynamic appearance of mitochondria during the recording as was shown in S1 movie is merely caused by their higher total number in the neurites. Furthermore, the average speeds of all analyzed POs and mitochondria calculated were 12 nm/sec (Figure 16C) and 20 nm/sec (Figure 16D) respectively. Also, the maximal actual speeds for the two organelles were 0.1 µm/sec for the neuronal POs (Figure 16C) and 0.06 µm/sec for neuronal mitochondria (Figure 16D). These results point to a similar transport mechanism underlying the distribution of both organelles in neurons.
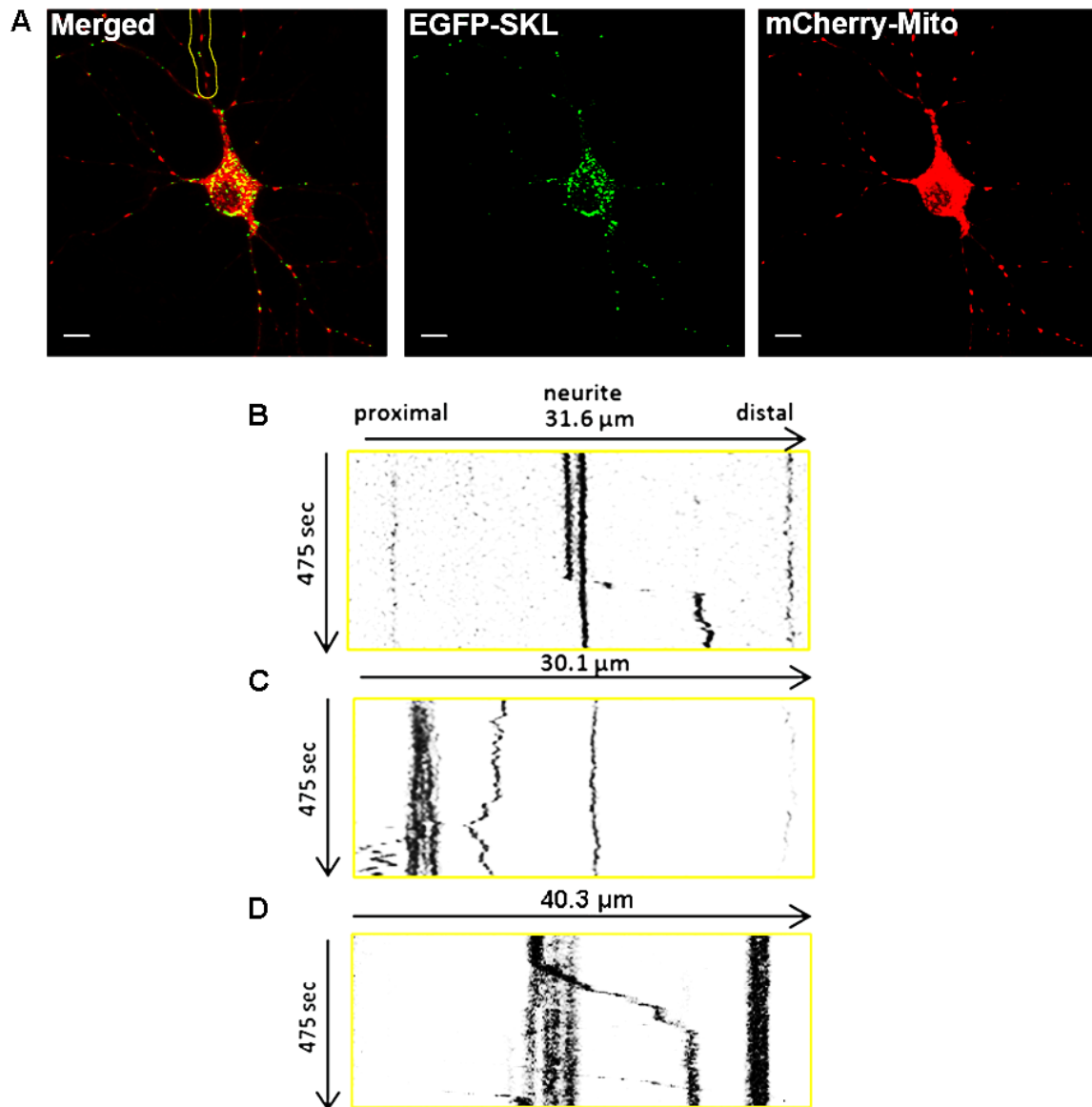
Figure 15. Live confocal imaging and kymograph analysis of PO and mitochondria in the neurites of hippocampal neurons.

(A) Live confocal images of PO and mitochondria, which were marked by expression of EGFP-SKL and mCherry-Mito, respectively. Maximum intensity projected from z-stacks. Scale bar: 10µm. (B-D) Representative kymographs of PO (B, C) and mitochondria (D) movements in neurites with the length of about 30-40 µm over a period of 8 min. Straight vertical lines show static organelles. (B) includes a rapid saltatory movement across approx. 10 µm. Typical back-and-forth movements of PO shown as jagged vertical lines in (C) were presented. Compared to PO movements, kymograph (D) shows relatively smooth moving of mitochondria in the neurites, but majority of the organelles stay static same as shown for POs.
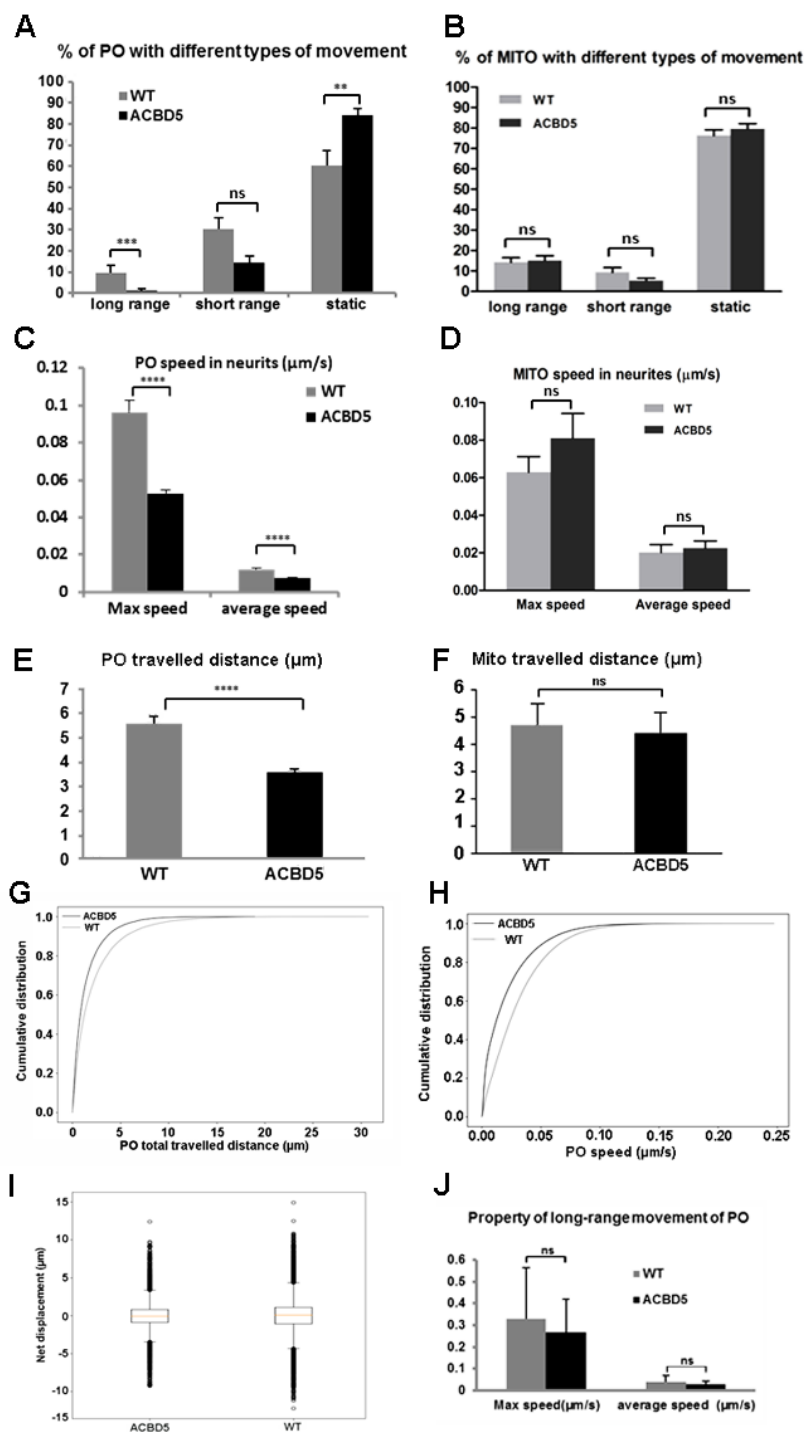
Figure 16. Quantitative assessment of PO and mitochondria motility in response to the expression of ACBD5

With measured total travelled distance during the analyzing time, PO (A) and mitochondria (B) motility was classified into long range movement (> 10 μm), short-range movement (> 5 μm, < 10 μm) and static PO (< 5 μm) in control neurons (WT) vs. myc-ACBD5 transfected neurons (ACBD5). Percentages of PO and mitochondria with different movements in each group were compared. Data showed that the percentage of PO with long range movement

was significantly decreased while static PO was increased in ACBD5-transfected neurons; no significant changes were detected for mitochondria movement types. Maximum actual and average speed (µm/s) of PO (C) and mitochondria (D) in the neurites for the two groups of neurons. Decreased speeds of POs in ACBD5-transfected neurons were found, while no change of speed for mitochondria was detected. Total traveled distance (µm) of measured POs (E) and mitochondria (F) in the neurites of the two groups of neurons. Data showed decreased distance of PO moving in ACBD5-transfected neurons, while the traveled distance of mitochondria was shown unchanged. Cumulative distribution of PO traveled distance (µm) (G) and speed (µm/s) (H) showed a similar decreased motility of PO in ACBD5-transfected neurons. Box plot of net displacement (µm) of POs (I) to examine the directionality and PO moving restrictions in the neurites of the two groups of neurons. Data showed that the proportions of anterograde (positive values) and retrograde (negative values) movements remain stable after expression of ACBD5, and the net displacements of PO in the neurites of ACBD5-transfected neurons were found more concentrated at 0 (µm) indicating more restricted PO movements in response to ACBD5 expression. The maximum and average speed of long-range traveling PO (µm/s) (J) for the two groups, shown an unchanged property of microtubule-based movement of PO.

6. 6. Expression of the peroxisome-ER tether ACBD5 alter peroxisome motility in hippocampal neurons

To investigate if the expression of the PO-ER tether ACBD5 alters PO motility in neurons, cultured primary hippocampal neurons were transfected at DIV7~9 with GFP-ACBD5 and EGFP-SKL as control, respectively. Plasmid coding for a mitochondria-targeted mCherry was co-transfected to monitor the mitochondrial motility as a reference. After twenty-four hours of expression, the motility of PO and mitochondria of the cultures were studied by confocal live imaging. Unfortunately, the significant difference in the signal morphologies of GFP-ACBD5 and EGFP-SKL could hamper a comparable PO identification for the two groups. To circumvent this problem, the two groups of hippocampal cultures were transfected with EGFP-SKL and Myc-ACBD5 + EGFP-SKL respectively, where POs were marked by EGFP-SKL for both groups (Figure 15A). The efficiency of co-expression of EGFP-SKL and Myc-ACBD5 was controlled by fixation and immunostaining of the cultures and was found to be about 88% (Figure 17). To test if PO motility would be altered in response to ACBD5 expression, kymograph plugin from ImageJ combined with a self-programmed automated organelle tracking code was applied to analyze PO motility

in the neurites of transfected neurons. Graphs describing the cumulative distribution of PO speed and PO traveled distance reveal that a higher number of PO remains more static after ACBD5 expression (Figure 16G, H). These findings are in line with the average and maximum speeds of the total PO population (Figure 16C). For a more detailed analysis, the different types of movements of POs and mitochondria in control and ACBD5 transfected neurons were grouped into static, short range and long range movements as described above. In the ACBD5 transfected neurons, the proportion of static PO increased to a value of 84% from 60% in control neurons, while those showing short and long-range movements decreased to 14% and 2% from 30% and 10% in control neurons, respectively (Figure 16A). Correspondingly, average speed and traveled distance of all analyzed PO decreased from 12 nm/sec to 7.5 nm/sec (Figure 16C) and 5.6 µm to 3.6 µm (Figure 16E) in the ACBD5-transfected neurons as compared to control groups, respectively. Of note, neuronal mitochondria motility remained unchanged in response to ACBD5 expression (Figure 16B, D, F), demonstrating that the observed changes are PO-specific and do not result from a generally decreased fitness of the ACBD5-transfected cells.
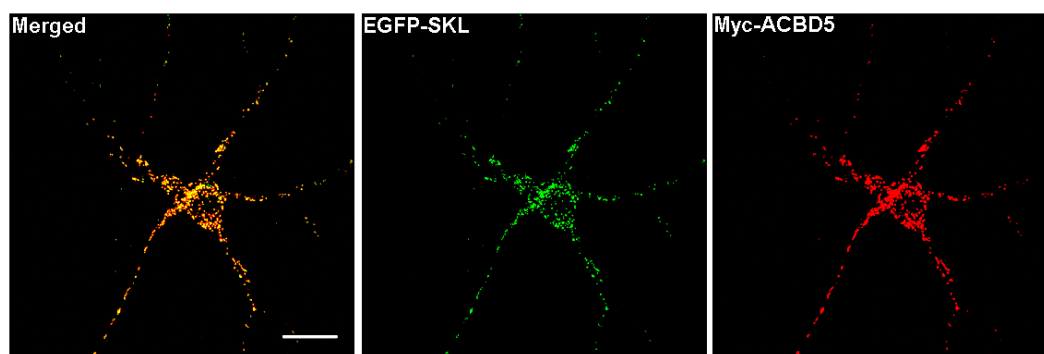
Figure 17. Sufficient co-expression efficiency of EGFP-SKL and myc-ACBD5 in the neuronal culture

Immunofluorescence images of neuron co-transfected by EGFP-SKL and myc-ACBD5. The efficiency, which reached up to about 88%, was sufficient enough to proceed with the subsequent live-imaging of PO motility of the two groups while using same PO indicator EGFP-SKL. Scale bar: 20µm.

Based on the observed reduced PO motility in neurons after ACBD5 expression, it might imply that the efficiency of the neuronal transport system was compromised by the ACBD5 expression. To evaluate this possibility, since long-range movements of

PO in higher eukaryotes have been shown to be microtubule-dependent (112, 113, 115), the speed of POs performing long-range movements were compared between the two groups, no significant differences were observed in either average or maximum speed of the moving PO (Figure 16J). With respect to the directionality of the transport, most PO movements did not result in a significant net anterograde or retrograde organelle translocation (Figure 16I). Within a time frame of about 8 min, most moving PO traveled back and forth along the axis of the neurites and exhibited net movement distances close to zero, while comparable amounts of PO were moving in an antero-/retrograde direction. Moreover, these parameters did not change in response to the ACBD5 overexpression. Thus, the observed data implies that the mechanics of the microtubule-based transport do not change in response to ACBD5 expression but merely the number of motile PO decreases.

6. 7. PO relocated to neurites and periphery of soma in neuron

Since the expression of ACBD5 was found to interfere with the transport of PO along the neurites of the hippocampal neurons, whether these changes in PO motility would affect the subcellular distribution of POs in neurons was investigated subsequently. To do so, cultured hippocampal neurons were transfected with EGFP-SKL and myc-ACBD5, respectively, at DIV7~9 and fixed after 24 hours. To identify the whole morphology of the neurons with different subdomains, cytosolic mCherry plasmid was co-expressed in either case (Figure 18A, B). After immunostaining and morphological analysis, major alterations in average PO size (μm^2), which may interfere with efficient transport in the neurons, was not detected (Figure 18C),. It is observed that the POs in the soma were preferentially located at the cell periphery in the vicinity of the plasma membrane in ACBD5 group (Figure 18B). By comparison, in the control group expressing EGFP-SKL, POs usually appeared in a juxtanuclear area (Figure 18A). To examine if these ACBD5-mediated PO redistributions are exclusively found in neurons, it was further analyzed the PO distribution patterns in EGFP-SKL or myc-ACBD5 transfected astrocytes in the same hippocampal cultures. It was found that a minor tendency of PO aggregation in the cytoplasm, however, a trend of a peripheral localization or an increase of PO in the astrocytic processes was not found (Figure 19A, B). Moreover, it is also not found such changes in PO distribution after ACBD5 expression in a variety of cell lines such as COS-7, HepG2 and human embryonic

fibroblasts (165). Therefore, the redistribution of POs in neurons appears to be cell-type specific.

To quantify PO positioning in neurons, the numbers and area of PO in the soma and in the proximal neurite area (proximal 30 µm of each neurite) were determined and compared between the two groups. In the WT (EGFP-SKL transfected) group, the number and volume (area) of POs in the soma were far higher than in the dendritic compartment (Figure 18D, G). The ACBD5 transfected neurons, in contrast, exhibited more or less equal PO numbers in the soma and the analyzed proximal region of the neurites (Figure 18D, G). When the percentage areas of PO in the soma and the neurites were compared, the total volume of POs in the soma decreased in response to myc-ACBD5 expression, while more POs were found in the neurites (Figure 18H, I). The increased PO quantity in the neurites might result from a PO proliferation. Hence, the total number of and area of POs in the soma and proximal 30 µm of all neurites were compared as well (Figure 18E, F). However, both values even decreased after ACBD5 transfection, such possibility hence excluded. Rather, the decreasing total number or area of POs in response to the ACBD5 expression may be associated to the fact that more POs are transported to even more distal neurites which are beyond the analyzed scope of this experiment.

The most straightforward explanation for this PO reorganization would be that the more POs are trapped at sites of ER subcompartments with a locally high VAPB concentration given the binding of ACBD5-VAPB. To test such hypothesis, primary hippocampal neurons were transfected with EGFP-SKL and myc-ACBD5 and immunostained with antibody against VAPB. As shown in Figure 20A and B, VAPB signals resemble a network-like staining pattern characteristic for the ER and concentrate in the somatic and the proximal dendritic area of the hippocampal neurons. In general, the staining is not only largely comparable to the signal pattern for other ER-marker plasmid such as RFP-KDEL (Figure 13A, Figure 14A, B), but reveal some particular focal concentrations, especially in the region surrounding the peri-nuclear Golgi apparatus. Unexpectedly, POs were not found to accumulate at sites with high local VAPB concentrations after ACBD5 expression, instead, POs were found to juxtapose along the cell membrane in the soma and dendrites of the hippocampal neurons – areas which were largely devoid of VAPB signals (Figure 20B). Therefore, it can be concluded that the ACBD5-VAPB interaction connecting

PO to the ER might not be responsible for this subcellular PO redistribution as described above.

To substantiate this assumption, wildtype of ACBD5 and ACBD5 with a mutated FFAT (2 phenylalanines in an acidic tract) motif were transfected and expressed in the neuronal culture. In general, FFAT domains can be found in a variety of VAPB interacting proteins and are required for effective binding between VAPB and the interacting proteins (170). As has been previously shown, this FFAT-mutant is unable to bind to VAPB using a pull-down approach (186). Thus, the PO distribution in those neurons transfected with FLAG-ACBD5 (human)-FFAT and FLAG-ACBD5 (human)-WT was compared. Remarkably, similar to WT ACBD5 expression (Figure 20D), POs redistributed towards the plasma membrane and into the neurites of FLAG-ACBD5-FFAT transfected neurons (Figure 20C). Additionally, higher magnifications reveal that many POs in the dendrites can be found in close proximity to the plasma membrane after expression of both ACBD5 variants (Figure 18B, Figure 20C, D).
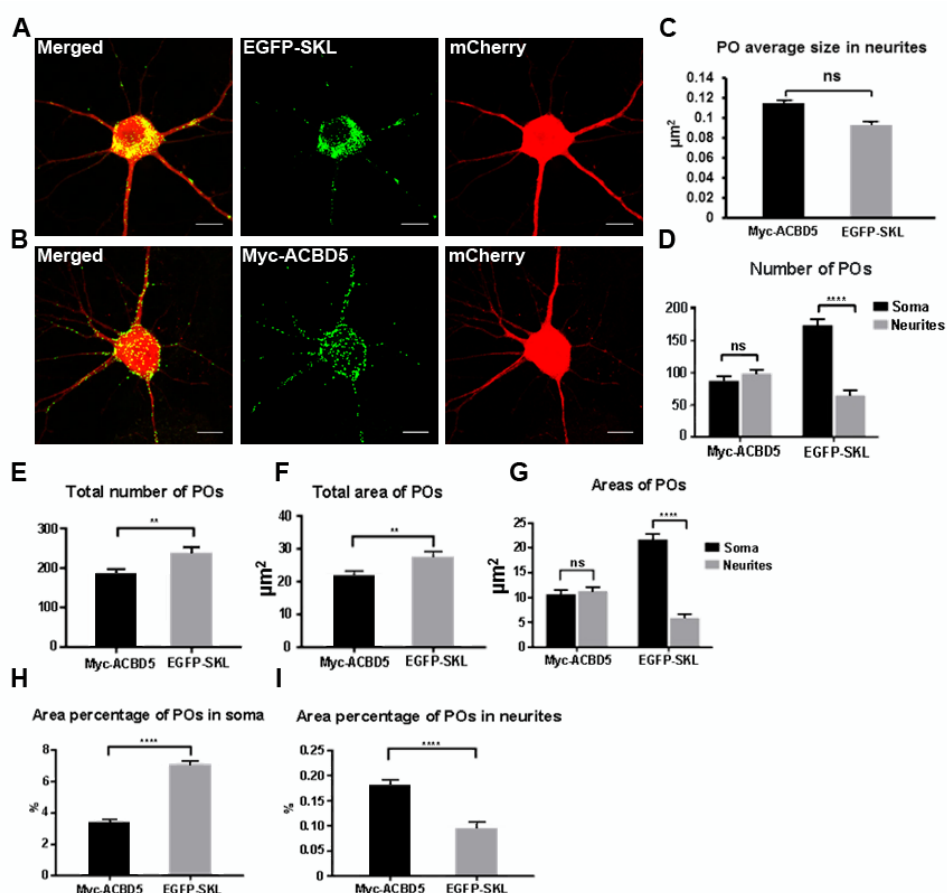
Figure 18. ACBD5 expression redistributes peroxisomes into neurites and the periphery of perikarya

PO morphology and distribution in primary hippocampal neurons in response to the overexpression of myc-ACBD5. (A-B) Confocal images of fixed PO in neurons co-transfected with mCherry and EGFP-SKL or with mCherry and myc-ACBD5 respectively. Scale bars represent 10 μm. (C) Average PO size (μm2) in ACBD5-transfected and control neurons, indicates a similar size of PO marked by EGFP-SKL and myc-ACBD5. (D) Number and (G) area of PO puncta in soma and proximal neurites with about 30 μm distance to the margin of soma, and compared within each group. Data shows that the number and area of PO in the neurites of ACBD5-transfected neurons were increased to a nearly equal level with that of in soma, whereas in control neurons, the PO was always highly enriched in the soma. (E) Total number and (F) area covered by PO in the measured area of transfected neurons, showing a slightly decreased overall PO number and area in the ACBD5-transfected neurons. Comparison of PO area percentage in (H) soma and (I) measured neurite area, indicating a distinct redistribution of PO from soma to neurites in ACBD5-transfected neurons.
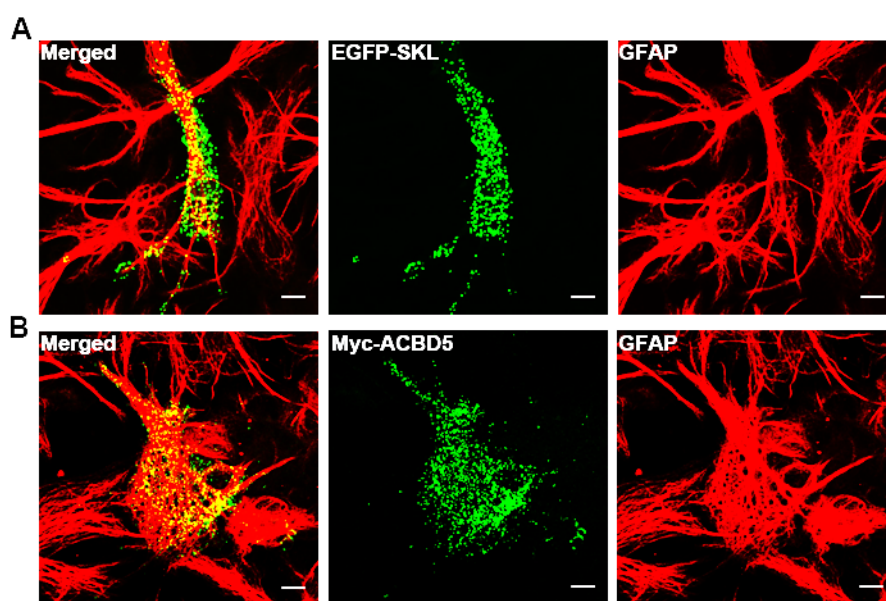
Figure 19. PO distribution in astrocytes after expression of ACBD5

(A-B) Astrocytes marked by GFAP immunostaining from primary neuronal culture transfected with EGFP-SKL or myc-ACBD5. Note that expression of ACBD5 does not change POs distribution in astrocytes. Representative immunofluorescence images presented as maximum intensity projections. Scale bar: 10μm.
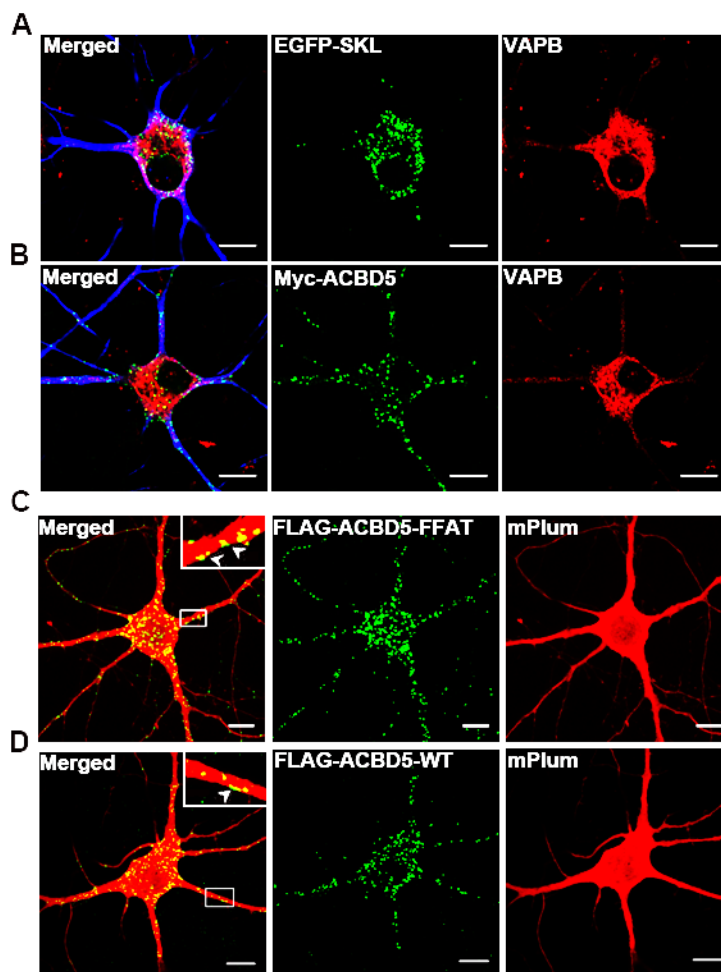
Figure 20. ACBD5-VAPB association in neurons

PO redistribution in response to ACBD5 expression does not depend on interaction with VAPB in neurons. (A-B) Localization of VAPB and EGFP-SKL, myc-ACBD5 in hippocampal neurons, respectively. MAP2-staining (blue in the overlay) was used as an additional dendrite marker of the neurons (scale bar: 10μm). (C-D) PO localization in neurons co-transfected with mPlum and FLAG-ACBD5-WT, FLAG-ACBD5-FFAT respectively, where the ACBD5 FFAT mutant is unable to interact with VAPB. Both proteins induce comparable PO redistribution. Scale bar: 10 μm. Insets: Higher magnification of POs shown in close proximity to plasma membrane indicated by arrowheads of dendrites enclosed by box areas.

6. 8. Close contacts between POs and mitochondria

During the organelle kinetic analysis, an unexpectedly high incidence of PO juxtaposed to mitochondria in the neurites of the hippocampal neurons was observed (Figure 21). Moreover, some POs performed sliding movements along larger, static mitochondrion, but did not migrate beyond the outline of the mitochondrion during the

whole analysis time (Figure 21A). Similar PO movements along mitochondria have been described in the yeast species Schizosaccharomyces pombe (199). Such a phenomenon may indicate a functional interaction between the two organelles, potentially associated with metabolite transfer or signaling events. Hence, whether the PO repositioning in neurites in response to ACBD5 expression might influence the contacts between PO and mitochondria was tested. To this end, the proportions of POs in juxtaposition to mitochondria in the neurites of the hippocampal neurons were determined for the control and ACBD5 groups. Using the live imaging data, the spatial association of the two organelles from the first frame of each dataset in the neurites of the hippocampal neurons was analyzed (Figure 21B, C). In controls, the percentage of PO located juxtaposed to mitochondria was found to be 84.6% - a remarkable value if compared to 20% as described for COS-7 cells (197). In addition, it was observed that most POs remained stable at positions proximity to individual mitochondria. In ACBD5 transfected neurons, the absolute number of POs juxtaposed to mitochondria were slightly increased (Figure 21B). However, no significant change was found in the proportion of PO contacting with mitochondria (Figure 21C), indicating that the PO repositioning had no impact on the interaction between PO and mitochondria.
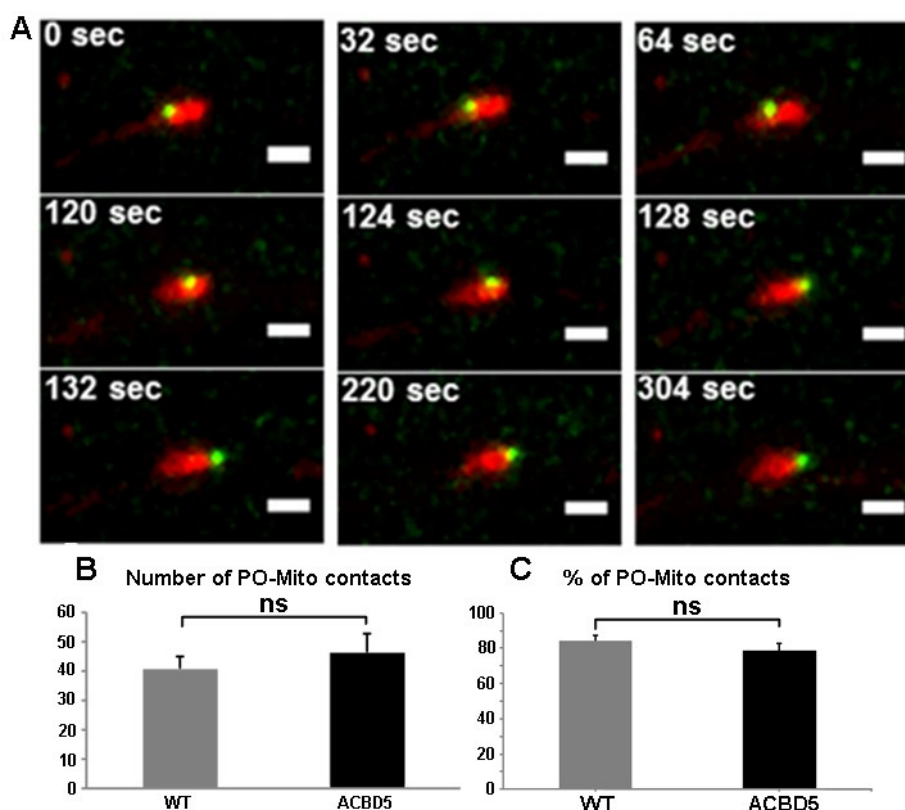
Figure 21. PO-mitochondria contacts in neurites

(A) Live confocal imaging of PO (79) and mitochondria (red) from a minor dendrite. PO and mitochondria were marked by expression of EGFP-SKL and mCherry-Mito. Time-lapse image series were collected and presented from 0 sec to 304 sec, demonstrating a PO swiftly "surfing" from the left edge to the right edge of a mitochondrion within approximately. 8 seconds. Then the PO was arrested at the right edge of the mitochondrion till the end of the recording. Maximum intensity projected from z-stacks. Scale bar: 2μm. (B) Absolute numbers of POs contacting mitochondria in the neurites of WT and ACBD5 groups, which were counted from the first frames of each time-lapse image. (C) The percentages of PO contacting mitochondria in the overall PO population for the two groups. No significant difference was detected either for the absolute number or the percentage of PO-mitochondria contacts suggesting unchanged PO-mitochondria contacts after ACBD5 expression.

Taken together, significant alterations in the motility and location of PO were observed in response to overexpression of this tether protein ACBD5. However, unlike in fibroblasts, interaction with the ER tethering protein VAPB was not found to be responsible for the observed changes of PO motility and distribution. The data indicates that ACBD5 might facilitate interactions with additional protein binding partners, which tether PO to the plasma membrane or other unidentified neuronal compartments in its vicinity.

7 DISCUSSION

In this study, polarized distribution of several organelles and molecular constituents of distinct neuronal compartments and the underlying potential molecular mechanisms were analyzed. Specifically, the distribution of axoaxonic GABAergic synapses and maturation of specialized ER-cisternal organelle (CO) was analyzed in the AIS with different origins (AcD vs. non AcD). The measured number of GABAergic synapses at the AIS *in vivo* indicated a potential homeostatic regulation of inhibitory synapses at the AIS- the site for generating APs as the neuronal output signal. The investigation of CO development in the AIS revealed a maturation time of 2~3 weeks in neuronal cultures and showed no significant difference in regard to various AIS origins. Subsequently, the polarized distribution and spatial relationships of POs and mitochondria were examined in neurites of cultured hippocampal neurons. A major impact of the tethering protein ACBD5 on positioning of neuronal POs was demonstrated for the first time in neurons.

7. 1. Differential distribution of GABAergic synapses at the AIS

It is evident that membrane protein compartmentalization in the AIS is crucial for the normal functioning of each individual neuron since the AIS serves as a key site for action potential (AP) in neurons (20). These AIS-enriched membrane proteins not only include various voltage-gated channels which are key elements for shaping the intrinsic neuronal excitability but also $GABA_A$ receptors ($GABA_AR$). These receptors in the AIS mostly contain α2 subunits and receive GABAergic terminals at the AIS (55). Neurons receive a large number of excitatory or inhibitory synaptic inputs along the somatodendritic domains, and such graded synaptic inputs are integrated at the AIS to fire all-or-none APs (25). Thus, the AIS is a prime compartment for inhibitory synaptic inputs regulating neuronal excitability together with other ion channels in the AIS. In hippocampus, AIS-specific GABAARα2 receive

GABAergic inputs mainly from axoaxonic GABAergic interneuron establishing inhibitory controls along the AIS (200). Inhibitory GABAergic synapses play various important roles in neuronal activities ranging from adjusting single neuron's excitability to neural network synchrony. It is reported that reduced GABAergic innervation at the AIS of cortical layer 2/3 pyramidal neurons appears to be specific

to the disease process of Schizophrenia (201). Indeed, GABAergic synapses work as a brake to AP generation, modulating the AP firing and synaptic strength, which adapt dynamically to the changing neuronal network activities (202). In addition to their effects on the single-cell level, these GABAergic synapses are also involved in the specific neuronal recruitment during different network activities through their inhibitory modulation with precise temporal and spatial controls (203). For instance, in hippocampus, the sparse occurrence of entrained spikes during spontaneously occurring high-frequency network oscillations is established based - among other factors - on the strength of GABAergic perisomatic inhibition (203).

In general, AIS-localized GABAARα2 containing synapses provide a fast synaptic inhibition controls within one millisecond over neuronal excitability of principal neurons in hippocampus and cortex (200). As mentioned previously, the origin of AIS can be either at the soma or at proximal dendrites thus establishing a topological diversity of AIS location. Those neurons with axon-carrying dendrites (AcDs) are characterized by a somatically recorded lower AP voltage threshold when uncaged glutamate is applied to the AcDs (33). Thus, AcDs have been suggested as privileged sites for synaptic excitation supporting facilitated AP generation, linking heterogeneity of AIS origin to distinct electrical properties of the neuron. Although it is still unclear how such heterogeneity of the AIS origin is established, the study of the GABAergic inputs in the AIS may help to explain the distinct electrical properties of AcD vs. non-ACD type of neurons.

To this end, the distribution of GABAergic synapses containing GABAARα2 at the AIS of AcD and nonAcD hippocampal neurons was analyzed on hippocampal sections of Thy1-GFP expressing transgenic mice. Antibodies against GABAARα2 and VGAT (a presynaptic marker for GABAergic synapses), were used to identify synapses that contact the AIS. After surface reconstructions of different fluorescent markers in the selected AIS and its surrounding area, the number of GABAergic synapses was counted and compared. Ultimately, an averaged number of 19 ± 1.17 synapses were found at the AIS of AcD neurons in hippocampus, while 14.8 ± 1.51 synapses were identified at the AIS of nonAcD neurons. However, compared to previous studies on GABAergic terminals at the AIS, these numbers differed – possibly due to variations in experimental approaches and examined brain regions. Specifically, 52 inhibitory inputs determined by the confocal staining of VGAT

apposing to gephyrin, a scaffolding protein for GABAARα2, were found at the AIS of principal cells in the basolateral amygdala (53). At the AIS of neurons in hippocampal slices about 6 - 8 VGAT or GABAARα2 positive synapses were determined at the AIS (204).

Despite such diverse numbers of the synapses at the AIS, the results of this study showed that the number of GABAergic synapses at the AIS of AcD neurons was slightly higher than that of at the AIS of nonAcD neurons. These results support the hypothesis that the distribution of GABAergic synapses at the AIS emerging from dendrites, which are considered more "excitable", may be adapted to this privilege site for synaptic inputs on the axon-carrying dendrites in a homeostatic manner. Similar to this, a recent study shows that cortical layer 5 pyramidal neurons with axons emerging from dendrites (AcD type) are characterized by a reduced dendritic complexity and thinner main apical dendrites associated with decreased synaptic inputs and dendritic capacitance (205). These results suggest that fine-tuned subcellular synaptic compartmentalization may serve as homeostatic regulation of neuronal excitability for the diverse neuronal morphology such as AcD and nonAcD neurons.

In addition to the potential close association of subcellular neuronal compartmentalization and heterogeneity of AIS origin, the investigation of structure and function of the diverse AIS origin is a still ongoing project currently embedded within the collaborative research initiative (SFB1134 A03). According to preliminary data from this project, during the sharp wave-ripple oscillation in hippocampus, AcD neurons preferentially participate in such oscillating neuronal ensembles as compared to no-AcD neurons. In parallel, analysis of the neuronal compartmentalization involved in AIS excitability might also help to explain the different electrical properties of AcD and nonAcD neurons, such as the expression of voltage-gated ion channels in the AIS, GABAARα2 and its associated proteins gephyrin and NF186. The later protein is known to be essential for establishment of GABAergic innervation on the AIS (206). Searching for other potential biomarkers for neurons with different AIS origins would be helpful to facilitate the study of neuron recruitments into neuronal network activities.

7. 2. Late maturation of the CO in the AIS

In the vicinity of the enriched GABAARα2 in the AIS, the cisternal organelle (CO) is another distinct feature of neuronal compartmentalization in the AIS. The CO is composed of stacks of smooth endoplasmic reticulum (ER) cisterns interdigitated by electron-dense plates (47). The CO is located beneath the plasma membrane and in proximity to GABAergic terminals at the AIS. Synaptopodin (SP), an actin-binding protein, colocalizes with the electron-dense plates found in CO as well as in the dendritic spine apparatus (SA). The SA is preferentially located in the neck of mature dendritic spines of cortical and hippocampal neurons and shares many structural similarities with the CO (207). Furthermore, SP is essential for the formation of both CO and SA in the corresponding neuronal subdomains (50) (207).

Functionally, COs are considered as putative intracellular Ca^{2+} store in the AIS. Indeed, a number of receptors and channels relevant proteins for Ca^{2+} storing and releasing have been colocalized with CO. Such colocalized components include sarco/endoplasmic reticulum Ca^{2+} ATPase (SERCA) type Ca^{2+} pump (48), which has also been confirmed in the current study (see Figure 12), inositol 1,4,5-triphosphate receptor 1 (IP3R1), the Ca^{2+} binding protein annexin 6 etc.(194). The regulation of intraneuronal Ca^{2+} concentration is critical for various activities both at the structural and functional level. The structural plasticity of the AIS, for example, has been proposed to be Ca^{2+} dependent, as Ca^{2+} entry influences activity-driven changes in the length and position of the AIS (82). At the functional level, the activity-dependent transient elevations of Ca^{2+} in the AIS also modulate generation and timing of AP (52). In addition, COs are often found in the vicinity of GABAergic synapses established along the AIS, suggesting a role in the regulation of GABAergic synaptic transmissions for the control of AP generation in the AIS (48). Therefore, representing local Ca^{2+}-stores compartments in the AIS, the COs may play an important role in linking structural plasticity to changes in excitability of the AIS. Based on this, it was hypothesized in this study that the CO might be established differentially in AcD vs. nonAcD neurons which have distinct electrophysiological properties (33).

To analyze the development of CO in the AIS, and examine whether there is a differential CO maturation in the AIS of AcD and nonAcD neurons, cultured hippocampal neurons at different stages were immunostained by antibodies against SP. β4-spectrin and MAP2 were co-stained for the morphology of the AIS and

somatodendritic domains of neurons to discriminate AcD and nonAcD neurons in the culture. Confocal images were collected and grouped for COs in the AIS of AcD and nonAcD neurons at DIV7, 14, and 21. The results showed that at the early stage of neuronal development (DIV7), clusters of SP were hardly found in the AIS for both AcD and nonAcD neurons, indicating a late development of CO in the AIS. At DIV14, the expression of SP reached a maximum level in the AIS. The total volume of SP-immunopositive puncta and the volume fraction of SP in the AIS of nonAcD neurons were slightly higher than in the AIS of AcD neurons. At DIV21, both the total volume and the volume fraction of SP puncta in the AIS decreased from their DIV14 maximum in nonAcD neurons. By comparison, AcD neurons did not exhibit such a developmental decrease of SP components. Additionally, at DIV21, the overall AIS volume of AcD neurons was higher than that of nonAcD neurons. In parallel, SP total volume in the AIS of AcD neurons was found slightly higher than that of nonAcD neurons. At the morphological level, maturation of the CO was associated with a transition of small punctate structures to elongated rod-like variants of COs.

With regard to the maturation of the CO, a recent *in vivo* study has addressed this issue in the developing mouse visual cortex (208). Interestingly, the results showed that the expression of SP was mostly absent from the AIS of 7 days old mice whereas the percentage of SP-expressing AIS considerably increased in 15 day old mice. Thus, the relatively late CO maturation in the AIS of cultured hippocampal neurons somehow resembles that of CO in visual cortical neurons. This resemblance implies that the CO maturation may follow a neuron-intrinsic developmental program than external biochemical cues provided by intact neuronal tissue. In principle, such intrinsic developmental features are well known for polarization of axonal and somatodendritic domains in cultured hippocampal neurons (2).

At the statistical level the differences of SP-associated values between AcD and nonAcD neurons failed to reach significance. This indicated that the establishment of the CO may not be related to the heterogeneity of AIS origins during the development. Thus, the volume of COs itself in the AIS might not play a major role in regulating differential AIS excitability. Indeed, there are many other potential links between structural dynamics of AIS and modifications of AIS excitability. Those structural features include not only the AIS length but also AIS distance to soma and the ion channel expression in the AIS (27). For instance, high neuronal activity

induces a distal relocation of the AIS, whereas low activity leads to a proximal AIS relocation (82, 209). Furthermore, previous findings revealed that the SA - an CO equivalent in dendritic spines – increased their size in response to a homeostatic synaptic strengthening (80). In addition, the positioning of SA – entering or leaving spines – has been suggested to play a functional role in synaptic activities (207). In this context, it would be worthwhile to investigate whether the COs also exhibit structural plasticity potentially coupled to functional conditions associated with the aforementioned dynamic changes of the AIS.

7. 3. Close proximity between neuronal PO and ER, mitochondria

Along with the specific potential roles of the CO in the AIS (described above), additional neuronal ER components fulfill a number of important functions in neuronal compartmentalization. Local neuronal ER constituents contribute to other cellular activities, which are equally critical for the normal functioning of neurons. For instance, the interaction of motor protein myosin Va and ER-localized Ca^{2+} channels are required for the axon guidance in the developing spinal cord *in vivo* (210). Also, the interactions with the microtubule cytoskeleton contribute to the maintenance of local neuronal ER morphology (211). Furthermore, interacting with other major neuronal compartments, such as peroxisomes (52) and mitochondria, is vital for those ER binding partners' biogenesis and functioning (98, 212). As described in the introduction previously, the existence of close contacts of ER-PO, ER-mitochondria through ultrastructural studies was revealed in non-neuronal cells (186, 213). These contacts may facilitate the exchange of metabolites and signaling molecules between two or more subcellular compartments or control fission events of POs and mitochondria. With regard to neurons, it is reasonable to postulate that their distinct morphology and cellular polarity require a stringent control of organelle distributions and contacts, such as ER-PO and ER-mitochondria contacts. To date, these organelle contacts have not yet been extensively studied in association with organelle positioning in neurons.

Therefore, to study the impact of organelle contacts on the positioning of organelles in neurons, the spatial relationships of neuronal ER, PO and mitochondria were studied to obtain a first impression of organelle contacts before further investigation of the organelles positioning in neurons. To analyze the spatial relationship of the organelles, two groups of cultured primary hippocampal neurons were co-transfected

by the plasmids encoding: RFP-KDEL(ER marker) and EGFP-SKL (PO marker), mPlum-Mito (mitochondria marker) and EGFP-SKL, respectively. Such labeled ER, PO, and mitochondria were subsequently visualized through high-resolution confocal microscopy under fixed or live conditions. In principle, the confocal images showed high densities of all three organelles in the soma and proximal neurites. As compared with neuronal ER which contains a considerable volume of tubule networks throughout the entire neuron, neuronal POs and mitochondria present quite discrete distributions in neurites. Such densely localized POs and mitochondria in the soma - instead of being distributed homogeneously throughout distal neuronal subdomains - contribute to the polarized distribution of neuronal organelles. However, regarding the investigation of organelle contacts in neurons, the high densities of those major organelles in soma render the analysis of spatial relationships of different organelles difficult. Nevertheless, the relative sparse distribution of POs and mitochondria in axons and dendrites facilitate experimental access to organellar contacts of PO using time-lapse imaging methods.

In recent years, an increasing number of studies focused on organelle contacts with the understanding that organelles are not free-moving but underlie a tightly controlled dynamic in the cytosol. By using simultaneously expressed fluorescent organelle markers, it was reported in a recent study that over 90% of POs are in contact with ER while only around 20% of POs contact mitochondria in COS-7 cells (197). However, in the current high-resolution confocal study, a large majority of neuronal POs was found in close proximity to both ER and mitochondria, which potentially reflects a different mechanism of organelle contact in neurons. In this context, it is of interest to investigate and compare the cellular mechanisms of such organelle distribution and contacts in highly polarized neurons. Of note, to visualize these specific organelle contacts with standard confocal microscopy is quite challenging. Within the limited space of neurites, the analysis of ER and PO/mitochondria contacts is difficult under current experimental conditions due to the major morphological difference between diffuse ER and discrete POs/mitochondria. By comparison, the contacts of POs and mitochondria are relatively discrete. Nevertheless, the resolution of standard confocal microscopy (~100–200 nm) fails to determine whether the two organelles are close enough to have a bona fide contact. Indeed, this would require a resolution of 10 - 40 nm corresponding to the distance between the two apposing organelle membranes (198). In order to obtain a higher resolution of the organelle

contacts in neurites, STED (Stimulated Emission Depletion) confocal microscopy was therefore applied. This approach provided the necessary resolution of ~20nm per pixel. The neuronal cultures expressing soluble ER fluorescent marker were fixed and stained by PEX14 and TOM20 to label POs and mitochondria and analyzed by STED imaging. Of note, deconvoluted STED confocal images displayed close proximity (a distance of ~20nm) between POs and mitochondria, confirming the existence of physical contacts between the two organelles. Taken together, the current study documents that a large proportion of POs and mitochondria are in close proximity to ER in neurites of neurons. Moreover, there is also a considerable proportion of POs that have physical contacts with mitochondria in neurons. Such close organelle contacts may regulate the sparse distribution of POs and mitochondria outside of somatic areas by counteracting the loading of POs and mitochondria to the microtubule-based transport system. This could control the motility of POs and mitochondria moving into the extended network of neuronal processes.

7. 4. Motility of PO and mitochondria in neurites

With regard to the previous section, the investigation of PO motility in neurites appeared to be of significant interest. In principle, contacts of POs and mitochondria, respectively, could interfere with their long-distance motility in neurites (see above). This issue was explored further using high-resolution time-lapse imaging. The motility of POs and mitochondria in neurons co-transected with PO and mitochondria fluorescent markers was recorded for ~8 minutes under live conditions. Subsequently, the kinetic properties of POs and mitochondria were determined from the time-lapse images through kymograph analysis. These properties included the maximum speed (µm/s, maximum instantaneous speed), average speed (µm/s, total traveled distance/recording time), total traveled distance (µm) and net displacement (µm, sum vectors of individual organelle displacements). To categorize the motility of both organelles according to their total traveled distance, the movements of the organelles were classified as either long-range (> 10 µm), short-range (> 5 µm, < 10 µm) or static (< 5 µm).

In principle, as observed from the time-lapse images (Figure 15), POs were moving quite discontinuously and changed directions very frequently within short ranges. Occasionally, POs displayed saltatory movements. In comparison, mitochondria were

moving relatively smooth and unidirectional. Such distinct motility patterns of the two organelles might explain the measured difference of velocities between the organelles. Specifically, the average speed of mitochondria (0.020 µm/s) was found to be higher than that of POs (0.012 µm/s), which could be explained by the discontinuity of PO motility. Yet, the maximum instantaneous speed of POs (0.1 µm/s) was found to be higher than that of mitochondria (0.06 µm/s), which most likely can be attributed to the occasional unique saltatory type of PO movements. In spite of the distinct differences in visual motility and those specific velocities between the two moving organelles, the kymograph analysis revealed that the motility of POs and mitochondria in neurites share major similarities. First, a large proportion of both organelles was static during the analysis time (60% of POs and 75% of mitochondria). Also, similar smaller proportions of short-range (30% of POs and 10% of mitochondria) and long-range (10% of POs and 15% of mitochondria) moving organelles were found for the two organelles. In addition, the total traveled distances of POs and mitochondria were both in the range of ~ 5µm. Such comparable motility of POs and mitochondria implies that both organelles might have similar transport mechanisms. Indeed, Kif5 and Miro1 have been found to be involved in microtubule-based movements of both PO and mitochondria (115, 214). This suggests significant shared molecular composition of their transporting systems. Taken together, both POs and mitochondria appear to be stationary in general with only small proportions performing long-distance movements in neuronal processes. A possible explanation for the high percentage of static POs and mitochondria may be the requirement for local ("static") metabolite exchanges and organelle maintenance in neurons.

7. 5. Decreased PO motility in response to ACBD5 expression

Since only small proportions of neuronal POs and mitochondria showed distinct movements in neurites, it can be reasoned that in neurons a large number of POs and mitochondria maintain close contacts with constituents of neuronal compartments in their vicinities. As one of the most common organelle contacts for POs, ER-PO contacts have been extensively studied and identified recently in non-neuronal cells including COS7 cells and human fibroblasts (165, 166). The newly identified binding complex between ER and POs includes VAPB, an ER-resident vesicle-associated membrane protein, and ACBD5, a PO-resident lipid-transfer-associated membrane protein (173).

Based on these previous findings in non-neuronal cells, the current studies addressed the question whether ACBD5 overexpression also has an impact on motility and distribution of POs in neurons. To this end, the following co-transfection strategy was used in hippocampal neuronal cultures: In the wildtype group, neurons were co-transfected by SKL-EGFP and mPlum-mito to visualize POs and mitochondria, respectively. For ACBD5 group, SKL-EGFP, mPlum-mito, and ACBD5-myc were co-transfected. Subsequently, PO motility was analyzed and compared between the two groups. The reason for using ACBD5-myc construct instead of ACBD5-GFP was the significant morphological difference of GFP signals between ACBD5-GFP and SKL-EGFP in transfected neurons. SKL-EGFP signals usually visualize individual POs more spherically and separately reflecting the expected PO morphology. In contrast, ACBD5-GFP expression in neurons was often displayed as clumps of GFP signals from the local accumulated POs. Therefore, ACBD5-GFP expression was not used for further motility analysis. Instead, SKL-EGFP was co-expressed with ACBD5-myc in ACBD5 group in order to acquire comparable signals of POs for both groups. Thus, the co-transfection efficiency of SKL-EGFP and ACBD5-myc was first examined to test the feasibility of such experimental design. As expected, the percentage of neurons co-expressing both peroxisomal markers (~88%) was sufficient to follow such strategy of motility analysis.

With the method of kymograph analysis, in principle, a decreased motility of POs in hippocampal neurites was shown in response to ACBD5 expression. Specifically, the proportion of static POs was significantly increased as compared to that in the wildtype group (84 % vs. 60 %), along with decreased percentages of POs moving in short-range (30 % vs. 14 %) and long-range (10 % vs. 2 %) distances. In line with this, the average speed decreased from 12 nm/s in the wildtype group to 7.5 nm/s in the ACBD5 group. The total traveled distance was also shortened to 3.6 μm in the ACBD5 group as compared to 5.6 μm in the wildtype group. The specificity of such ACBD5-mediated impairment of PO motility was examined by analysis of simultaneously recorded mitochondria motility. Interestingly, mitochondria motility remained unaltered in response to ACBD5 expression, indicating a PO-specific effect of ACBD5. Such unaffected mitochondria motility also excluded the possibility of a generally compromised organelle transport system resulting from degeneration of neurons during time-lapse imaging.

Furthermore, it was investigated whether the decreased PO-specific motility resulted from an impairment of microtubule-based PO transport system. To this aim, long-range movements of POs were compared between the two groups, since long-range movements critically depend on the integrity of the microtubule-based transport system. No significant changes between the two groups were found, indicating an unaffected microtubule-based PO transport system. Alternatively, it is possible that the decreased PO motility in response to ACBD5 expression is due to reduced numbers of POs loading to the microtubule-based transport system. Furthermore, it can be speculated that an increased number of POs was binding to molecular components of other neuronal compartments and therefore are rather static organelles in neurons overexpressing ACBD5.

Further analysis in the current thesis the directionality of neuronal PO movement was examined. In the wildtype group, POs were frequently observed to move back and forth. Indeed, the net displacement (see Figure 16I) of most POs accumulated to ~0 µm. In addition, no preference of either anterograde or retrograde movement was found. Although in the ACBD5 group, the distribution of PO net displacements was shown a narrower variation around 0 µm, no shift in directionality of moving PO was discovered. Such unchanged directionality of PO motility suggests unaffected affinities of PO to anterograde and retrograde acting motor proteins in the microtubule-driven transport system.

Which other molecular interactions could be responsible for the impaired PO motility? Recently, overexpression of a PO-targeted variant of microtubule adaptor protein MIRO1 increased PO motility in COS-7 cells (214). In addition, increased motility of POs was also noted in human fibroblasts when PO-ER contacts were reduced (186). Thus, the extended network of neuronal ER tubules might act as an organellar scaffold, which retains globular organelles such as POs at defined intracellular locations counteracting the microtubule-based transport system. In this context, the network of neuronal ER interacting could play a regulating role in the maintenance of the polarized organelle distributions in neurons. Specifically, neuronal POs could interact with the ER via the ACBD5-VAPB tethering, which may prevent them from entering the microtubule-based neuronal transport systems.

7. 6. Redistribution of neuronal PO in response to ACBD5 expression

A significant redistribution of POs from the central somatic area to the more distal compartment of neurites was found in response to ACBD5 expression (see Figure 18). As mentioned above, the majority of POs in wildtype neurons are located densely in the somatic area, with only a small proportion of POs scattered in neurites. Interestingly, in the ACBD5 group the proportions of POs were significantly changed with roughly equal numbers of POs in the soma and proximal neurite areas. Moreover, the measured total number and area of POs in individual neurons of ACBD5 group were decreased as compared to that of in wildtype group. Considering the potential trend towards peripheral PO redistribution, those "missing" POs in ACBD5 group might be explained as a certain number of POs redistributed even further into distal neurite areas exceeding the boundaries of analyzed images. Additionally, the redistributed POs often localized preferentially beneath the plasma membrane (PM), both in the soma and neurites. Recently, such PM translocation of PO have also been described in yeast (143), implying that PO-PM binding might be common for organelle interaction of POs. Functionally, PO localization in the vicinity of the plasma membrane might be required for efficient processing of PM lipids.

In contrast to the neuronal redistribution of PO after ACBD5 overexpression, such changes are not seen in a variety of non-neuronal cell lines such as COS-7, HepG2, and human embryonic fibroblasts (186). The primary hippocampal neuronal cultures used in this study were prepared from the dissociated cells of embryonic hippocampi, which contain a proportion of glial cells (astrocytes) in addition to the large majority of hippocampal neurons. Such mixed cultures provide an opportunity to verify the phenomenon of PO redistribution in other primary cells such as astrocytes as a control in this experiment. Therefore, cultures containing astrocytes transfected by SKL-EGFP or ACBD5-myc were fixed and imaged with the same microscopy method. Although a minor trend of PO aggregation in the cytoplasm was found (see Figure 19), an obvious peripheral redistribution of POs into peripheral astrocytic processes was not found. Therefore, the ACBD5-mediated PO redistribution may occur in a cell-type specific manner.

As described previously, ACBD5 was recently identified as an ER-PO binding partner with VAPB, an ER-resident membrane protein in a variety of non-neuronal cells. Accordingly, the most straightforward explanation of PO repositioning would be that more POs with overexpressed ABCD5 were trapped at the local sites of ER

subcompartments containing high concentrations of VAPB. In this context, a potentially upregulated binding of ACBD5-VAPB constituting PO-ER contacts might be responsible for the repositioning of POs into the periphery of neurons. To test such hypothesis, primary hippocampal neurons were transfected with EGFP-SKL and myc-ACBD5 respectively and co-immunostained with antibody against VAPB. VAPB signals resemble a network-like staining pattern characteristic for the ER and concentrate in the somatic and the proximal dendritic area of the hippocampal neurons. In principle, the staining is largely comparable to pattern of other ER-marker - such as RFP-KDEL- but also reveals some distinct focal concentrations, especially in the region surrounding the peri-nuclear Golgi apparatus. In line with this pattern of VABP-immunostaining, VAPB indeed facilitates vesicle trafficking at the ER-Golgi intermediate compartment (ERGIC) in rat hippocampal neurons (215). However, POs were not found to accumulate at such sites with high local VAPB concentrations after ACBD5 expression. Instead, POs were found to juxtapose beneath the cell membrane of the soma and dendrites – areas which were largely devoid of VAPB signals. Therefore, it can be concluded that the ACBD5-VAPB interaction connecting PO to the ER might not be responsible for this subcellular PO redistribution as described above.

To further analyze the effects of PO-ER contacts through ACBD5-VAPB binding in PO redistribution, either wildtype ACBD5 or ACBD5 with a mutated FFAT (2 phenylalanines in an acidic tract) motif were transfected and expressed in the neuronal culture. In principle, FFAT domains can be found in a variety of VAPB interacting proteins and are required for effective binding between VAPB and the interacting proteins (Murphy and Levine 2016). In pull-down experiments, the mutant FFAT of ACBD5 cannot bind to VAPB (186). Thus, the PO distribution in neurons transfected with FLAG-ACBD5–FFAT[mut] and FLAG-ACBD5-WT was compared to evaluate the role of ACBD5-VAPB binding in the observed PO redistribution. Interestingly, similar to wildtype ACBD5 expression, POs were also redistributed towards the PM and distal neurites with FLAG-ACBD5-FFAT[mut] expression. This result indicates that ACBD5-VAPB tethering might not be responsible for the distinct PO redistribution in neurons. Consequently, whether the ER-PO contacts were altered with ACBD5 overexpression along with PO redistribution remains unclear. Instead, some other yet unidentified PO contacts may regulate PO repositioning after ACBD5-overexpression.

7. 7. Dynamic relationship between PO and mitochondria

During the organelle motility analysis, unexpectedly, a large proportion of POs that are static or moving in a short range were localized in vicinity of mitochondria. Moreover, a number of POs performed sliding movements along the surface of relatively large and static mitochondrion. Similar PO movements along the surface of mitochondria have also been described in yeast and were found to be cytoskeleton-independent (199). In addition to these short-range sliding movements, it was observed that most POs remained relative static attached to the proximity to individual mitochondria. Such a phenomenon may indicate some dynamic relationship between the two organelles in neurons. Accordingly, it is tempting to hypothesize that a close functional interaction between POs and mitochondria exists possibly associated with metabolite transfer or signaling events in neurons (135, 216). Second, the motility of neuronal POs might not only depend on the loading to the microtubule-based transport system but also on the interactions with mitochondria through PO-mitochondria bindings.

It is reasonable to examine whether the PO-mitochondria interactions are regulated by ACBD5. To this end, the number and percentage of POs contacting mitochondria in hippocampal neurites were determined for the wildtype and ACBD5 groups. Using the same time-lapse image datasets used for motility analysis, the first frames of each dataset were extracted to analyze the dynamic spatial relationship of the two organelles. As discussed in the previous section, in the control group the proportion of POs located in close proximities to mitochondria was found to be 84.6%. Of note, this percentage is much higher than that previously found in COS-7 cells (20%) (197). In ACBD5 transfected neurons, the number of POs juxtaposed to mitochondria was slightly increased while the percentage of that is decreased slightly. Statistically, however, no significant differences were found between the two groups. This suggests that the PO repositioning in response to ACBD5 may not be primarily attributable to altered interaction between POs and mitochondria. Besides, kymograph analysis showed that motility of mitochondria remained unchanged after ACBD5 expression. Further elucidation of the complex associations between POs and mitochondria in neurons are warranted but not within the scope of the current thesis.

Taken together, significant alterations in the motility and location of POs were observed in response to overexpression of the tether protein ACBD5. However, unlike in fibroblasts (186), interaction with the ER tethering protein VAPB was not found to be responsible for the observed changes of PO motility and distribution. Instead, the current data indicates that ACBD5 might facilitate interactions with additional – yet unknown - protein binding partners. Such unknown binding partners would serve to tether PO to the PM/cortical ER. In addition, such binding to other unidentified neuronal compartments may interfere with loading of POs to the microtubule-based transport system. This latter possibility should preferentially alter fast and long-range movements, which are usually microtubule-based, while slow and short-range movements - usually actin-based-, should not be altered (217). However, according to the observations in the current experiments, short and long-range PO movements were similarly altered by ACBD5 expression. Moreover, there is no bias between retro- and anterograde PO transports in response to ACBD5 expression, which could explain the increased PO localization in the dendritic compartments of the hippocampal neurons. Since proper organelle distribution along the elongated processes is heavily dependent on an efficient transport system, immobilization of POs by organelle tethering would gradually slow down PO transport and consequently increase the number of PO in neurites. Thus, it can be concluded that alteration of organelle tethering might most likely be the molecular cause for the altered PO positioning in the hippocampal cultures, although such novel and specific interaction partners still remain to be identified in future experiments.

Specifically, it remains to be determined why ACBD5 expression in hippocampal neurons does not preferentially interact with VAPB as observed in other cell types (166, 186). In addition to the FFAT binding motif, the ACBD5 amino acid sequence exhibits additional predicted coiled-coil domains which are common protein interaction mediating structures (218). Moreover, VAPB expression has been reported to be quite low in hippocampal neurons as compared to other neuronal cell types like motor neurons (219). Thus, ACBD5 might interact with some other unidentified binding partners in neurons. In this regard, it is tempting to speculate that ACBD5 might serve as a multivalent tether, which connects PO to a variety of different organelles in different cell types. Interestingly, other interactors with VAPB – such as the mitochondrial membrane protein tyrosine phosphatase interacting protein 51 (PTPIP51) - indeed exhibit tissue-specific interactomes (68, 172) thereby

adjusting its protein interaction network to specific functions of a distinct cell type. Likewise, the VAPA/B proteins form tethering complexes with a variety of different proteins binding the ER to mitochondria, endosomes/lysosomes, the Golgi apparatus, POs, lipid droplets, and the PM, thereby forming a flexible organelle interaction network (170). Similarly, ACBD5 might act as a tethering partner which is able to trigger the formation of more than one organelle tethering complex. Finally, post-translational protein phosphorylation, which has been described for ACBD5 (220, 221), might serve to regulate the interaction with the different organelle-specific contacting complexes.

Furthermore, it remains to be investigated why POs might favor different organelle interactions in the hippocampal neurons. In addition to the ER, POs are known to specifically interact with mitochondria at sites of e.g. acyl-CoA synthesis or mitochondria-ER junctions indicating distinct functional relationships at the contact zone (144). In neurons, POs contribute to the maintenance of a defined redox potential and hence exert influence on neuronal firing rates (222). POs intricately cooperate with mitochondria in the regulation of cellular redox homeostasis (132). The currently observed high incidence of PO-mitochondria contacts in neurites of cultured neurons might be associated with the control of ROS (reactive oxygen species) generation. However, future studies are required to test this hypothesis.

In summary, the work described in the present thesis focused on analysis of polarized positioning of neuronal constituents in different compartments, including GABAergic synapses, CO, and POs. The potential correlation between the heterogeneity of neuronal morphology and polarized distribution of subcellular compartments was discussed. The results imply that the differential distribution of inhibitory GABAergic terminals at the AIS - which are highly relevant to control AP generation – could play a role in homeostasis of neuronal excitability potentially relevant for neuronal network function *in vivo*. The AIS-associated GABA-terminals are found in proximity to a distinct type of axonal ER – the so-called CO. The distribution of such CO does correlate with morphological variation of AIS (AcD vs. nonAcD). A tight control in the distribution of other major organelles, such as POs, is equally vital for the normal function of a neuron. Organelle contacts of POs most likely serve as a major factor in regulating their distribution and motility in distinct cell types. Hence, the newly identified PO tether ACBD5 was used to evaluate the impact

of organelle contacts on the positioning of POs in hippocampal neurons. Eventually, the alteration of ACBD5 expression in neurons leads to significant redistribution and decreased motility of POs, strongly suggesting that ACBD5 plays an important role in regulating motility and distribution of neuronal POs.

8 SUMMARY

Neurons are widely known for their distinct structure and function among other mammalian cells. In particular, neurons are well appreciated for their advanced degree of cellular polarity. A variety of well-defined neuronal compartments is indeed characterized by a distinct set of membrane proteins or major organelles. A thorough understanding of the mechanisms underlying the formation and significance of such neuronal polarity has become of particular importance to the field of neuroscience. With the aim to obtain a deeper understanding of neuronal polarity, the following principal aspects of neuronal compartmentalization were studied:

First, using high-resolution confocal microscopy in combination with 3D reconstruction, GABAergic synapses containing $GABA_AR\alpha2$ at the axon initial segment (AIS) were analyzed and compared among hippocampal neurons with variation in their AIS origin (AcD vs. nonAcD). The results show that a larger number of GABAergic synapses is found at the AIS emerging from dendrites (AcD) as compared to the AIS directly emerging from the soma (nonAcD). Previous observations revealed that dendrites that give rise to axons are more excitable than those that do not give rise to an axon. In addition, inhibitory control on action potential firing in the AIS is known to be dependent on AIS-localized GABAergic synapses. The larger number of GABAergic AIS synapses found in the AcD variant could thus contribute to homeostatic regulation of neuronal excitability.

Second, the development of AIS-specific ER (cisternal organelle; CO) was investigated in the AcD vs. nonAcD variant of cultured hippocampal neurons. In principle, the results revealed that the CO in the AIS was barely expressed within the first week (DIV7) but reached its maximum volume rapidly within the second week (DIV14) and attained full maturation after ~3 weeks (DIV21). During DIV14 - DIV21, the CO volume appears to be proportional to the AIS volume. However, the total volume of CO within the AIS was not significantly different when AcD neurons were compared with nonAcD neurons. These results indicate that the CO matures relatively late and is not differentially established in AcD vs nonAcD neurons.

Third, the current thesis provides the first comprehensive analysis on polarized distribution and motility of neuronal peroxisomes (PO) (52). Specifically, the impact of

ACBD5 - a recently identified regulator for PO-ER binding- was examined in cultured hippocampal neurons. A significant redistribution of POs was induced by such ACBD5 overexpression. A considerable proportion of POs in ACBD5-transfected neurons were redistributed into the neurites from the soma and preferentially positioned beneath the plasma membrane both in the soma and neurites. Interestingly, such ACBD5-mediated PO redistribution is neuron-specific since it is absent in co-cultured glial cells (astrocytes). In addition, neuronal PO redistribution was independent of ACBD5 tethering to VAPB – an ER-resident membrane protein. This finding is in contrast to ACBD5-VAPB tethering previously reported in non-neuronal cells. Therefore, the existence of a yet unidentified binding partner for ACBD5 in neuronal POs is postulated.

In addition to the redistribution of neuronal POs in response to ACBD5 expression, a reduced motility of POs was found in neurites after ACBD5 overexpression. With high-resolution time-lapse imaging and kymograph analysis, the proportion of static POs significantly increased in neurites of ACBD5-transfected neurons as compared to those without ACBD5 overexpression (60% vs. 84%). The average speed of POs decreased from 12 nm/s to 7.5 nm/s and the total traveled distance was shortened from 5.6 µm to 3.6 µm. Furthermore, this ACBD5-mediated effect is PO-specific, as a comparative analysis revealed that mitochondria motility is not affected by ACBD5.

Interestingly, a high percentage of POs (~85%) in neurites were found in contact with mitochondria. Time-lapse imaging revealed that a subset of such POs performed sliding movements along the surface of large static individual mitochondria. Such findings strongly suggest a dynamic relationship between POs and mitochondria in neurons.

Taken together, the results suggest that ACBD5, as a PO-resident membrane protein, is involved in the polarized distribution and motility of neuronal PO.

9 BIBLIOGRAPHY

1.   Tahirovic S, Bradke F. Neuronal Polarity. Cold Spring Harbor Perspectives in Biology. 2009;1(3):a001644.
2.   Craig AM, Banker G. Neuronal polarity. Annual review of neuroscience. 1994;17:267-310.
3.   Kollins KM, Davenport RW. Branching morphogenesis in vertebrate neurons. Branching morphogenesis: Springer; 2005. p. 8-65.
4.   van Beuningen SF, Hoogenraad CC. Neuronal polarity: remodeling microtubule organization. Curr Opin Neurobiol. 2016;39:1-7.
5.   Bentley M, Banker G. The cellular mechanisms that maintain neuronal polarity. Nature Reviews Neuroscience. 2016;17:611.
6.   Hoogenraad CC, Bradke F. Control of neuronal polarity and plasticity--a renaissance for microtubules? Trends Cell Biol. 2009;19(12):669-76.
7.   Witte H, Neukirchen D, Bradke F. Microtubule stabilization specifies initial neuronal polarization. J Cell Biol. 2008;180(3):619-32.
8.   Papasozomenos SC, Binder LI. Phosphorylation determines two distinct species of Tau in the central nervous system. Cell motility and the cytoskeleton. 1987;8(3):210-26.
9.   Kapitein LC, Hoogenraad CC. Which way to go? Cytoskeletal organization and polarized transport in neurons. Molecular and cellular neurosciences. 2011;46(1):9-20.
10.   D'Este E, Kamin D, Gottfert F, El-Hady A, Hell SW. STED nanoscopy reveals the ubiquity of subcortical cytoskeleton periodicity in living neurons. Cell Rep. 2015;10(8):1246-51.
11.   Xu K, Zhong G, Zhuang X. Actin, spectrin, and associated proteins form a periodic cytoskeletal structure in axons. Science. 2013;339(6118):452-6.
12.   He J, Zhou R, Wu Z, Carrasco MA, Kurshan PT, Farley JE, et al. Prevalent presence of periodic actin–spectrin-based membrane skeleton in a broad range of neuronal cell types and animal species. Proceedings of the National Academy of Sciences. 2016;113(21):6029-34.
13.   Ganguly A, Tang Y, Wang L, Ladt K, Loi J, Dargent B, et al. A dynamic formin-dependent deep F-actin network in axons. J Cell Biol. 2015:jcb. 201506110.
14.   Baas PW, Deitch JS, Black MM, Banker GA. Polarity orientation of microtubules in hippocampal neurons: uniformity in the axon and nonuniformity in the dendrite. Proceedings of the National Academy of Sciences. 1988;85(21):8335-9.
15.   Gu J, Firestein BL, Zheng JQ. Microtubules in dendritic spine development. Journal of Neuroscience. 2008;28(46):12120-4.
16.   Hu X, Viesselmann C, Nam S, Merriam E, Dent EW. Activity-dependent dynamic microtubule invasion of dendritic spines. Journal of Neuroscience. 2008;28(49):13094-105.
17.   Nirschl JJ, Ghiretti AE, Holzbaur ELF. The impact of cytoskeletal organization on the local regulation of neuronal transport. Nature Reviews Neuroscience. 2017;18:585.
18.   Farías Ginny G, Guardia Carlos M, Britt Dylan J, Guo X, Bonifacino Juan S. Sorting of Dendritic and Axonal Vesicles at the Pre-axonal Exclusion Zone. Cell Reports. 2015.
19.   Britt DJ, Farías GG, Guardia CM, Bonifacino JS. Mechanisms of Polarized Organelle Distribution in Neurons. Frontiers in Cellular Neuroscience. 2016;10(88).
20.   Bender KJ, Trussell LO. The physiology of the axon initial segment. Annual review of neuroscience. 2012;35:249-65.
21.   Song AH, Wang D, Chen G, Li Y, Luo J, Duan S, et al. A selective filter for cytoplasmic transport at the axon initial segment. Cell. 2009;136(6):1148-60.

22. Al-Bassam S, Xu M, Wandless Thomas J, Arnold Don B. Differential Trafficking of Transport Vesicles Contributes to the Localization of Dendritic Proteins. Cell Reports. 2012;2(1):89-100.

23. Watanabe K, Al-Bassam S, Miyazak Y, Wandless TJ, Webster P, Arnold DB. Networks of Polarized Actin Filaments in the Axon Initial Segment Provide a Mechanism for Sorting Axonal and Dendritic Proteins. Cell reports. 2012;2(6):1546-53.

24. Rasband MN. The axon initial segment and the maintenance of neuronal polarity. Nat Rev Neurosci. 2010;11(8):552-62.

25. Yoshimura T, Rasband MN. Axon initial segments: diverse and dynamic neuronal compartments. Current Opinion in Neurobiology. 2014;27:96-102.

26. Jamann N, Jordan M, Engelhardt M. Activity-dependent axonal plasticity in sensory systems. Neuroscience. 2017.

27. Petersen AV, Cotel F, Perrier J-F. Plasticity of the Axon Initial Segment: Fast and Slow Processes with Multiple Functional Roles. The Neuroscientist. 2017;23(4):364-73.

28. Cruz DA, Lovallo EM, Stockton S, Rasband M, Lewis DA. Postnatal Development of Synaptic Structure Proteins in Pyramidal Neuron Axon Initial Segments in Monkey Prefrontal Cortex. The Journal of comparative neurology. 2009;514(4):353-67.

29. Kneynsberg A, Kanaan NM. Aging Does Not Affect Axon Initial Segment Structure and Somatic Localization of Tau Protein in Hippocampal Neurons ofFischer344 Rats. eneuro. 2017.

30. Grubb MS, Burrone J. Activity-dependent relocation of the axon initial segment fine-tunes neuronal excitability. Nature. 2010;465(7301):1070-4.

31. Kuba H. Structural tuning and plasticity of the axon initial segment in auditory neurons. The Journal of Physiology. 2012;590(Pt 22):5571-9.

32. Martina M, Vida I, Jonas P. Distal initiation and active propagation of action potentials in interneuron dendrites. Science. 2000;287(5451):295-300.

33. Thome C, Kelly T, Yanez A, Schultz C, Engelhardt M, Cambridge Sidney B, et al. Axon-Carrying Dendrites Convey Privileged Synaptic Input in Hippocampal Neurons. Neuron. 2014;83(6):1418-30.

34. Kaifosh P, Losonczy A. The Inside Track: Privileged Neural Communication through Axon-Carrying Dendrites. Neuron. 2014;83(6):1231-4.

35. Zhou D, Lambert S, Malen PL, Carpenter S, Boland LM, Bennett V. Ankyrin(G) Is Required for Clustering of Voltage-gated Na Channels at Axon Initial Segments and for Normal Action Potential Firing. The Journal of Cell Biology. 1998;143(5):1295-304.

36. Duflocq A, Le Bras B, Bullier E, Couraud F, Davenne M. Nav1.1 is predominantly expressed in nodes of Ranvier and axon initial segments. Molecular and cellular neurosciences. 2008;39(2):180-92.

37. Leterrier C, Brachet A, Fache MP, Dargent B. Voltage-gated sodium channel organization in neurons: protein interactions and trafficking pathways. Neuroscience letters. 2010;486(2):92-100.

38. Lorincz A, Nusser Z. Molecular identity of dendritic voltage-gated sodium channels. Science. 2010;328(5980):906-9.

39. Boiko T, Van Wart A, Caldwell JH, Levinson SR, Trimmer JS, Matthews G. Functional specialization of the axon initial segment by isoform-specific sodium channel targeting. The Journal of neuroscience : the official journal of the Society for Neuroscience. 2003;23(6):2306-13.

40. Hu W, Tian C, Li T, Yang M, Hou H, Shu Y. Distinct contributions of Na(v)1.6 and Na(v)1.2 in action potential initiation and backpropagation. Nature neuroscience. 2009;12(8):996-1002.

41.   Goldberg EM, Clark BD, Zagha E, Nahmani M, Erisir A, Rudy B. K+ channels at the axon initial segment dampen near-threshold excitability of neocortical fast-spiking GABAergic interneurons. Neuron. 2008;58(3):387-400.

42.   Lorincz A, Nusser Z. Cell-type-dependent molecular composition of the axon initial segment. The Journal of neuroscience : the official journal of the Society for Neuroscience. 2008;28(53):14329-40.

43.   Ogawa Y, Horresh I, Trimmer JS, Bredt DS, Peles E, Rasband MN. Postsynaptic density-93 clusters Kv1 channels at axon initial segments independently of Caspr2. The Journal of neuroscience : the official journal of the Society for Neuroscience. 2008;28(22):5731-9.

44.   D'Este E, Kamin D, Balzarotti F, Hell SW. Ultrastructural anatomy of nodes of Ranvier in the peripheral nervous system as revealed by STED microscopy. Proceedings of the National Academy of Sciences of the United States of America. 2017;114(2):E191-e9.

45.   Leterrier C. The axon initial segment: an updated viewpoint. The Journal of Neuroscience. 2018.

46.   Grubb MS, Burrone J. Building and maintaining the axon initial segment. Current Opinion in Neurobiology. 2010;20(4):481-8.

47.   Peters A, Proskauer CC, Kaiserman-Abramof IR. The small pyramidal neuron of the rat cerebral cortex: the axon hillock and initial segment. The Journal of cell biology. 1968;39(3):604-19.

48.   Benedeczky I, Molnar E, Somogyi P. The cisternal organelle as a Ca(2+)-storing compartment associated with GABAergic synapses in the axon initial segment of hippocampal pyramidal neurones. Experimental brain research. 1994;101(2):216-30.

49.   Antón-Fernández A, Rubio-Garrido P, DeFelipe J, Muñoz A. Selective presence of a giant saccular organelle in the axon initial segment of a subpopulation of layer V pyramidal neurons. Brain Structure and Function. 2015;220(2):869-84.

50.   Bas Orth C, Schultz C, Müller CM, Frotscher M, Deller T. Loss of the cisternal organelle in the axon initial segment of cortical neurons in synaptopodin-deficient mice. The Journal of Comparative Neurology. 2007;504(5):441-9.

51.   Callewaert G, Eilers J, Konnerth A. Axonal calcium entry during fast 'sodium'action potentials in rat cerebellar Purkinje neurones. The Journal of Physiology. 1996;495(3):641-7.

52.   Blackmer T, Kuo SP, Bender KJ, Apostolides PF, Trussell LO. Dendritic calcium channels and their activation by synaptic signals in auditory coincidence detector neurons. Journal of neurophysiology. 2009;102(2):1218-26.

53.   Veres JM, Nagy GA, Vereczki VK, Andrási T, Hájos N. Strategically Positioned Inhibitory Synapses of Axo-axonic Cells Potently Control Principal Neuron Spiking in the Basolateral Amygdala. The Journal of Neuroscience. 2014;34(49):16194-206.

54.   Nusser Z, Sieghart W, Somogyi P. Segregation of different GABAA receptors to synaptic and extrasynaptic membranes of cerebellar granule cells. Journal of Neuroscience. 1998;18(5):1693-703.

55.   Kole MH, Stuart GJ. Signal processing in the axon initial segment. Neuron. 2012;73(2):235-47.

56.   Luscher B, Fuchs T, Kilpatrick Casey L. GABAA Receptor Trafficking-Mediated Plasticity of Inhibitory Synapses. Neuron. 2011;70(3):385-409.

57.   Jean-Marc F, Patrizia P. GABAA receptors and plasticity of inhibitory neurotransmission in the central nervous system. European Journal of Neuroscience. 2014;39(11):1845-65.

58.   Muir J, Kittler J. Plasticity of GABAA receptor diffusion dynamics at the axon initial segment. Frontiers in Cellular Neuroscience. 2014;8.

59.   Franker MAM, Hoogenraad CC. Microtubule-based transport – basic mechanisms, traffic rules and role in neurological pathogenesis. Journal of Cell Science. 2013;126(11):2319-29.

60.   Farías GG, Guardia CM, De Pace R, Britt DJ, Bonifacino JS. BORC/kinesin-1 ensemble drives polarized transport of lysosomes into the axon. Proceedings of the National Academy of Sciences. 2017;114(14):E2955-E64.

61.   Held H. Beiträge zur Structur der Nerverzellen und ihrer Fortsätze. Arch Anat Physiol Anat Abt. 1895;1:396-416.

62.   Baas PW, Lin S. Hooks and comets: The story of microtubule polarity orientation in the neuron. Developmental neurobiology. 2011;71(6):403-18.

63.   Mikhaylova M, Bera S, Kobler O, Frischknecht R, Kreutz MR. A Dendritic Golgi Satellite between ERGIC and Retromer. Cell Rep. 2016;14(2):189-99.

64.   Silverman MA, Kaech S, Jareb M, Burack MA, Vogt L, Sonderegger P, et al. Sorting and directed transport of membrane proteins during development of hippocampal neurons in culture. Proceedings of the National Academy of Sciences of the United States of America. 2001;98(13):7051-7.

65.   Lipka J, Kapitein LC, Jaworski J, Hoogenraad CC. Microtubule-binding protein doublecortin-like kinase 1 (DCLK1) guides kinesin-3-mediated cargo transport to dendrites. The EMBO journal. 2016;35(3):302-18.

66.   González C, Couve A. The axonal endoplasmic reticulum and protein trafficking: Cellular bootlegging south of the soma. Seminars in Cell & Developmental Biology. 2014;27:23-31.

67.   Saheki Y, De Camilli P. Endoplasmic Reticulum-Plasma Membrane Contact Sites. Annual review of biochemistry. 2017;86:659-84.

68.   Brobeil A, Kämmerer F, Tag C, Steger K, Gattenlöhner S, Wimmer M. PTPIP51—A New RelA-tionship with the NFκB Signaling Pathway. Biomolecules. 2015;5(2):485-504.

69.   Ramírez OA, Couve A. The endoplasmic reticulum and protein trafficking in dendrites and axons. Trends in Cell Biology. 2011;21(4):219-27.

70.   Zhang H, Hu J. Shaping the Endoplasmic Reticulum into a Social Network. Trends in Cell Biology. 2016;26(12):934-43.

71.   Krijnse-Locker J, Parton RG, Fuller SD, Griffiths G, Dotti CG. The organization of the endoplasmic reticulum and the intermediate compartment in cultured rat hippocampal neurons. Molecular biology of the cell. 1995;6(10):1315-32.

72.   Renvoise B, Blackstone C. Emerging themes of ER organization in the development and maintenance of axons. Curr Opin Neurobiol. 2010;20(5):531-7.

73.   Horton AC, Ehlers MD. Dual modes of endoplasmic reticulum-to-Golgi transport in dendrites revealed by live-cell imaging. The Journal of neuroscience : the official journal of the Society for Neuroscience. 2003;23(15):6188-99.

74.   Cooney JR, Hurlburt JL, Selig DK, Harris KM, Fiala JC. Endosomal compartments serve multiple hippocampal dendritic spines from a widespread rather than a local store of recycling membrane. Journal of Neuroscience. 2002;22(6):2215-24.

75.   Cui-Wang T, Hanus C, Cui T, Helton T, Bourne J, Watson D, et al. Local Zones of Endoplasmic Reticulum Complexity Confine Cargo in Neuronal Dendrites. Cell. 2012;148(1):309-21.

76.   Spacek J, Harris KM. Three-dimensional organization of smooth endoplasmic reticulum in hippocampal CA1 dendrites and dendritic spines of the immature and mature rat. The Journal of neuroscience : the official journal of the Society for Neuroscience. 1997;17(1):190-203.

77.   Verkhratsky A. Physiology and pathophysiology of the calcium store in the endoplasmic reticulum of neurons. Physiological reviews. 2005;85(1):201-79.

78.   Pfenninger KH. Plasma membrane expansion: a neuron's Herculean task. Nat Rev Neurosci. 2009;10(4):251-61.

79.   Greengard P. The neurobiology of slow synaptic transmission. Science. 2001;294(5544):1024-30.

80.   Vlachos A, Korkotian E, Schonfeld E, Copanaki E, Deller T, Segal M. Synaptopodin regulates plasticity of dendritic spines in hippocampal neurons. The Journal of neuroscience : the official journal of the Society for Neuroscience. 2009;29(4):1017-33.

81.   Lam AKM, Galione A. The endoplasmic reticulum and junctional membrane communication during calcium signaling. Biochimica et Biophysica Acta (BBA) - Molecular Cell Research. 2013;1833(11):2542-59.

82.   Grubb MS, Burrone J. Activity-dependent relocation of the axon initial segment fine-tunes neuronal excitability. Nature. 2010;465(7301):1070.

83.   Holbro N, Grunditz A, Oertner TG. Differential distribution of endoplasmic reticulum controls metabotropic signaling and plasticity at hippocampal synapses. Proceedings of the National Academy of Sciences of the United States of America. 2009;106(35):15055-60.

84.   Borgese N, Francolini M, Snapp E. Endoplasmic reticulum architecture: structures in flux. Curr Opin Cell Biol. 2006;18(4):358-64.

85.   Stefano G, Hawes C, Brandizzi F. ER - the key to the highway. Current opinion in plant biology. 2014;22:30-8.

86.   Valenzuela JI, Jaureguiberry-Bravo M, Couve A. Neuronal protein trafficking: Emerging consequences of endoplasmic reticulum dynamics. Molecular and Cellular Neuroscience. 2011;48(4):269-77.

87.   Kim S, Leal SS, Halevy DB, Gomes CM, Lev S. Structural requirements for VAP-B oligomerization and their implication in amyotrophic lateral sclerosis-associated VAP-B (P56S) neurotoxicity. Journal of Biological Chemistry. 2010;285(18):13839-49.

88.   Kapitein LC, Schlager MA, Kuijpers M, Wulf PS, van Spronsen M, MacKintosh FC, et al. Mixed microtubules steer dynein-driven cargo transport into dendrites. Current biology : CB. 2010;20(4):290-9.

89.   Erdmann R. Assembly, maintenance and dynamics of peroxisomes. Biochimica et Biophysica Acta (BBA) - Molecular Cell Research. 2016;1863(5):787-9.

90.   Waterham HR, Ferdinandusse S, Wanders RJA. Human disorders of peroxisome metabolism and biogenesis. Biochimica et Biophysica Acta (BBA) - Molecular Cell Research. 2016;1863(5):922-33.

91.   Schrader M, Costello JL, Godinho LF, Azadi AS, Islinger M. Proliferation and fission of peroxisomes - An update. Biochimica et biophysica acta. 2016;1863(5):971-83.

92.   Iwata J, Ezaki J, Komatsu M, Yokota S, Ueno T, Tanida I, et al. Excess peroxisomes are degraded by autophagic machinery in mammals. The Journal of biological chemistry. 2006;281(7):4035-41.

93.   Oku M, Sakai Y. Peroxisomes as dynamic organelles: autophagic degradation. The FEBS journal. 2010;277(16):3289-94.

94.   Lazarow PB, Fujiki Y. Biogenesis of peroxisomes. Annual review of cell biology. 1985;1:489-530.

95.   Platta HW, Erdmann R. Peroxisomal dynamics. Trends Cell Biol. 2007;17(10):474-84.

96.   Schrader M, Bonekamp N, Islinger M. Fission and proliferation of peroxisomes. Biochimica et Biophysica Acta (BBA)-Molecular Basis of Disease. 2012;1822(9):1343-57.

97.   Smith JJ, Aitchison JD. Peroxisomes take shape. Nature reviews Molecular cell biology. 2013;14(12):803-17.

98.   Hoepfner D, Schildknegt D, Braakman I, Philippsen P, Tabak HF. Contribution of the endoplasmic reticulum to peroxisome formation. Cell. 2005;122(1):85-95.

99.   van der Zand A, Gent J, Braakman I, Tabak HF. Biochemically distinct vesicles from the endoplasmic reticulum fuse to form peroxisomes. Cell. 2012;149(2):397-409.

100.   Fujiki Y, Okumoto K, Mukai S, Honsho M, Tamura S. Peroxisome biogenesis in mammalian cells. Frontiers in physiology. 2014;5:307.

101.   Hettema EH, Erdmann R, van der Klei I, Veenhuis M. Evolving models for peroxisome biogenesis. Curr Opin Cell Biol. 2014;29:25-30.

102.   Hettema EH, Gould SJ. Organelle formation from scratch. Nature. 2017;542:174.

103.   Wanders RJ. Peroxisomes, lipid metabolism, and peroxisomal disorders. Molecular genetics and metabolism. 2004;83(1-2):16-27.

104.   Ebberink MS, Koster J, Visser G, Spronsen F, Stolte-Dijkstra I, Smit GP, et al. A novel defect of peroxisome division due to a homozygous non-sense mutation in the PEX11beta gene. Journal of medical genetics. 2012;49(5):307-13.

105.   Mignarri A, Vinciguerra C, Giorgio A, Ferdinandusse S, Waterham H, Wanders R, et al. Zellweger Spectrum Disorder with Mild Phenotype Caused by PEX2 Gene Mutations. JIMD reports. 2012;6:43-6.

106.   Thoms S, Gartner J. First PEX11beta patient extends spectrum of peroxisomal biogenesis disorder phenotypes. Journal of medical genetics. 2012;49(5):314-6.

107.   Matsui S, Funahashi M, Honda A, Shimozawa N. Newly identified milder phenotype of peroxisome biogenesis disorder caused by mutated PEX3 gene. Brain & development. 2013;35(9):842-8.

108.   Yakunin E, Moser A, Loeb V, Saada A, Faust P, Crane DI, et al. alpha-Synuclein abnormalities in mouse models of peroxisome biogenesis disorders. Journal of neuroscience research. 2010;88(4):866-76.

109.   Santos MJ, Quintanilla RA, Toro A, Grandy R, Dinamarca MC, Godoy JA, et al. Peroxisomal proliferation protects from β-amyloid neurodegeneration. Journal of Biological Chemistry. 2005;280(49):41057-68.

110.   Beach A, Burstein MT, Richard VR, Leonov A, Levy S, Titorenko VI. Integration of peroxisomes into an endomembrane system that governs cellular aging. Frontiers in physiology. 2012;3:283.

111.   Schrader M, Thiemann M, Fahimi HD. Peroxisomal motility and interaction with microtubules. Microscopy research and technique. 2003;61(2):171-8.

112.   Rapp S, Saffrich R, Anton M, Jakle U, Ansorge W, Gorgas K, et al. Microtubule-based peroxisome movement. Journal of Cell Science. 1996;109(4):837-49.

113.   Wiemer EA, Wenzel T, Deerinck TJ, Ellisman MH, Subramani S. Visualization of the peroxisomal compartment in living mammalian cells: dynamic behavior and association with microtubules. The Journal of cell biology. 1997;136(1):71-80.

114.   Schrader M, King SJ, Stroh TA, Schroer TA. Real time imaging reveals a peroxisomal reticulum in living cells. Journal of Cell Science. 2000;113(20):3663-71.

115.   Kural C, Kim H, Syed S, Goshima G, Gelfand VI, Selvin PR. Kinesin and dynein move a peroxisome in vivo: a tug-of-war or coordinated movement? Science. 2005;308(5727):1469-72.

116.   Neuhaus A, Eggeling C, Erdmann R, Schliebs W. Why do peroxisomes associate with the cytoskeleton? Biochimica et Biophysica Acta (BBA) - Molecular Cell Research. 2016;1863(5):1019-26.

117.   Koch A, Thiemann M, Grabenbauer M, Yoon Y, McNiven MA, Schrader M. The dynamin-like protein DLP1 is involved inperoxisomal fission. Journal of Biological Chemistry. 2002.

118.   Bonekamp NA, Sampaio P, de Abreu FV, Lüers GH, Schrader M. Transient complex interactions of mammalian peroxisomes without exchange of matrix or membrane marker proteins. Traffic (Copenhagen, Denmark). 2012;13(7):960-78.

119.   Kulić IM, Brown AE, Kim H, Kural C, Blehm B, Selvin PR, et al. The role of microtubule movement in bidirectional organelle transport. Proceedings of the National Academy of Sciences. 2008.

120.   Arnold G, Holtzman E. Microperoxisomes in the central nervous system of the postnatal rat. Brain Research. 1978;155(1):1-17.

121.   Kassmann CM, Quintes S, Rietdorf J, Möbius W, Sereda MW, Nientiedt T, et al. A role for myelin-associated peroxisomes in maintaining paranodal loops and axonal integrity. FEBS letters. 2011;585(14):2205-11.

122.   Stamer K, Vogel R, Thies E, Mandelkow E, Mandelkow E-M. Tau blocks traffic of organelles, neurofilaments, and APP vesicles in neurons and enhances oxidative stress. The Journal of cell biology. 2002;156(6):1051-63.

123.   Nguyen T, Bjorkman J, Paton BC, Crane DI. Failure of microtubule-mediated peroxisome division and trafficking in disorders with reduced peroxisome abundance. Journal of cell science. 2006;119(4):636-45.

124.   Waterham HR, Koster J, van Roermund CW, Mooyer PA, Wanders RJ, Leonard JV. A lethal defect of mitochondrial and peroxisomal fission. New England Journal of Medicine. 2007;356(17):1736-41.

125.   Ishihara N, Nomura M, Jofuku A, Kato H, Suzuki SO, Masuda K, et al. Mitochondrial fission factor Drp1 is essential for embryonic development and synapse formation in mice. Nature cell biology. 2009;11(8):958.

126.   Wakabayashi J, Zhang Z, Wakabayashi N, Tamura Y, Fukaya M, Kensler TW, et al. The dynamin-related GTPase Drp1 is required for embryonic and brain development in mice. The Journal of cell biology. 2009;186(6):805-16.

127.   Schrader M, Grille S, Fahimi HD, Islinger M. Peroxisome interactions and cross-talk with other subcellular compartments in animal cells. Sub-cellular biochemistry. 2013;69:1-22.

128.   English AR, Voeltz GK. Endoplasmic reticulum structure and interconnections with other organelles. Cold Spring Harbor Perspectives in Biology. 2013;5(4):a013227.

129.   Helle SC, Kanfer G, Kolar K, Lang A, Michel AH, Kornmann B. Organization and function of membrane contact sites. Biochimica et biophysica acta. 2013;1833(11):2526-41.

130.   Islinger M, Grille S, Fahimi HD, Schrader M. The peroxisome: an update on mysteries. Histochemistry and Cell Biology. 2012;137(5):547-74.

131.   Wanders RJ. Metabolic functions of peroxisomes in health and disease. Biochimie. 2014;98:36-44.

132.   Lismont C, Nordgren M, Van Veldhoven PP, Fransen M. Redox interplay between mitochondria and peroxisomes. Frontiers in cell and developmental biology. 2015;3:35.

133.   Antonenkov VD, Hiltunen JK. Transfer of metabolites across the peroxisomal membrane. Biochimica et Biophysica Acta (BBA)-Molecular Basis of Disease. 2012;1822(9):1374-86.

134.   Neuspiel M, Schauss AC, Braschi E, Zunino R, Rippstein P, Rachubinski RA, et al. Cargo-selected transport from the mitochondria to peroxisomes is mediated by vesicular carriers. Current Biology. 2008;18(2):102-8.

135.   Schrader M. Shared components of mitochondrial and peroxisomal division. Biochimica Et Biophysica Acta (BBA)-Molecular Cell Research. 2006;1763(5-6):531-41.

136.   Camoes F, Bonekamp N, Delille H, Schrader M. Organelle dynamics and dysfunction: a closer link between peroxisomes and mitochondria. Journal of inherited metabolic disease. 2009;32(2):163-80.

137.   Delille HK, Schrader M. Targeting of hFis1 to peroxisomes is mediated by Pex19p. Journal of Biological Chemistry. 2008;283(45):31107-15.

138.   Gandre-Babbe S, van der Bliek AM. The novel tail-anchored membrane protein Mff controls mitochondrial and peroxisomal fission in mammalian cells. Molecular biology of the cell. 2008;19(6):2402-12.

139.   Dixit E, Boulant S, Zhang Y, Lee AS, Odendall C, Shum B, et al. Peroxisomes are signaling platforms for antiviral innate immunity. Cell. 2010;141(4):668-81.

140. Kagan JC. Signaling organelles of the innate immune system. Cell. 2012;151(6):1168-78.

141. Braverman NE, D'agostino MD, MacLean GE. Peroxisome biogenesis disorders: Biological, clinical and pathophysiological perspectives. Developmental disabilities research reviews. 2013;17(3):187-96.

142. McGuinness M, Lu J-F, Zhang H-P, Dong G-X, Heinzer A, Watkins P, et al. Role of ALDP (ABCD1) and mitochondria in X-linked adrenoleukodystrophy. Molecular and cellular biology. 2003;23(2):744-53.

143. Shai N, Yifrach E, van Roermund CWT, Cohen N, Bibi C, Ijlst L, et al. Systematic mapping of contact sites reveals tethers and a function for the peroxisome-mitochondria contact. Nature Communications. 2018;9:1761.

144. Cohen Y, Klug YA, Dimitrov L, Erez Z, Chuartzman SG, Elinger D, et al. Peroxisomes are juxtaposed to strategic sites on mitochondria. Molecular bioSystems. 2014;10(7):1742-8.

145. Ušaj MM, Brložnik M, Kaferle P, Žitnik M, Wolinski H, Leitner F, et al. Genome-wide localization study of yeast Pex11 identifies peroxisome–mitochondria interactions through the ERMES complex. Journal of molecular biology. 2015;427(11):2072-87.

146. Cohen Y, Klug YA, Dimitrov L, Erez Z, Chuartzman SG, Elinger D, et al. Peroxisomes are juxtaposed to strategic sites on mitochondria. Molecular bioSystems. 2014;10(7):1742-8.

147. Shibata Y, Shemesh T, Prinz WA, Palazzo AF, Kozlov MM, Rapoport TA. Mechanisms Determining the Morphology of the Peripheral ER. Cell. 2010;143(5):774-88.

148. Shai N, Schuldiner M, Zalckvar E. No peroxisome is an island — Peroxisome contact sites. Biochimica et Biophysica Acta (BBA) - Molecular Cell Research. 2016;1863(5):1061-9.

149. Thazar-Poulot N, Miquel M, Fobis-Loisy I, Gaude T. Peroxisome extensions deliver the Arabidopsis SDP1 lipase to oil bodies. Proceedings of the National Academy of Sciences. 2015:201403322.

150. Thiemann M, Schrader M, Völkl A, Baumgart E, Fahimi HD. Interaction of peroxisomes with microtubules: In vitro studies using a novel peroxisome-microtubule binding assay. European journal of biochemistry. 2000;267(20):6264-75.

151. Novikoff A, Shin W-Y. The endoplasmic reticulum in the Golgi zone and its relations to microbodies, Golgi apparatus and autophagic vacuoles in rat liver cells. J Microsc. 1964;3:187-206.

152. Zaar K, Völkl A, Fahimi HD. Association of isolated bovine kidney cortex peroxisomes with endoplasmic reticulum. Biochimica et Biophysica Acta (BBA)-Biomembranes. 1987;897(1):135-42.

153. Fahimi H, Baumgart E, Völkl A. Ultrastructural aspects of the biogenesis of peroxisomes in rat liver. Biochimie. 1993;75(3-4):201-8.

154. Grabenbauer M, Sätzler K, Baumgart E, Fahimi HD. Three-dimensional ultrastructural analysis of peroxisomes in HepG2 cells. Cell biochemistry and biophysics. 2000;32(1-3):37-49.

155. Barton KA, Mathur N, Mathur J. Simultaneous live-imaging of peroxisomes and the ER in plant cells suggests contiguity but no luminal continuity between the two organelles. Frontiers in physiology. 2013;4:196.

156. Raychaudhuri S, Prinz WA. Nonvesicular phospholipid transfer between peroxisomes and the endoplasmic reticulum. Proceedings of the National Academy of Sciences of the United States of America. 2008;105(41):15785-90.

157. West M, Zurek N, Hoenger A, Voeltz GK. A 3D analysis of yeast ER structure reveals how ER domains are organized by membrane curvature. The Journal of cell biology. 2011;193(2):333-46.

158.   Yan M, Rachubinski DA, Joshi S, Rachubinski RA, Subramani S. Dysferlin domain-containing proteins, Pex30p and Pex31p, localized to two compartments, control the number and size of oleate-induced peroxisomes in Pichia pastoris. Molecular biology of the cell. 2008;19(3):885-98.

159.   van der Zand A, Braakman I, Tabak HF. Peroxisomal membrane proteins insert into the endoplasmic reticulum. Molecular biology of the cell. 2010;21(12):2057-65.

160.   Schackmann MJA, Ofman R, Dijkstra IME, Wanders RJA, Kemp S. Enzymatic characterization of ELOVL1, a key enzyme in very long-chain fatty acid synthesis. Biochimica et Biophysica Acta (BBA) - Molecular and Cell Biology of Lipids. 2015;1851(2):231-7.

161.   Berendse K, Engelen M, Ferdinandusse S, Majoie CBLM, Waterham HR, Vaz FM, et al. Zellweger spectrum disorders: clinical manifestations in patients surviving into adulthood. Journal of inherited metabolic disease. 2016;39:93-106.

162.   Braverman NE, Moser AB. Functions of plasmalogen lipids in health and disease. Biochimica et biophysica acta. 2012;1822(9):1442-52.

163.   David C, Koch J, Oeljeklaus S, Laernsack A, Melchior S, Wiese S, et al. A combined approach of quantitative interaction proteomics and live-cell imaging reveals a regulatory role for endoplasmic reticulum (ER) reticulon homology proteins in peroxisome biogenesis. Molecular & Cellular Proteomics. 2013;12(9):2408-25.

164.   Knoblach B, Sun X, Coquelle N, Fagarasanu A, Poirier RL, Rachubinski RA. An ER-peroxisome tether exerts peroxisome population control in yeast. The EMBO journal. 2013;32(18):2439-53.

165.   Costello JL, Castro IG, Hacker C, Schrader TA, Metz J, Zeuschner D, et al. ACBD5 and VAPB mediate membrane associations between peroxisomes and the ER. The Journal of Cell Biology. 2017;216(2):331-42.

166.   Hua R, Cheng D, Coyaud É, Freeman S, Di Pietro E, Wang Y, et al. VAPs and ACBD5 tether peroxisomes to the ER for peroxisome maintenance and lipid homeostasis. The Journal of Cell Biology. 2017;216(2):367-77.

167.   Loewen CJ, Roy A, Levine TP. A conserved ER targeting motif in three families of lipid binding proteins and in Opi1p binds VAP. The EMBO journal. 2003;22(9):2025-35.

168.   Wyles JP, Ridgway ND. VAMP-associated protein-A regulates partitioning of oxysterol-binding protein-related protein-9 between the endoplasmic reticulum and Golgi apparatus. Experimental cell research. 2004;297(2):533-47.

169.   Lev S, Halevy DB, Peretti D, Dahan N. The VAP protein family: from cellular functions to motor neuron disease. Trends in cell biology. 2008;18(6):282-90.

170.   Murphy SE, Levine TP. VAP, a versatile access point for the endoplasmic reticulum: review and analysis of FFAT-like motifs in the VAPome. Biochimica et Biophysica Acta (BBA)-Molecular and Cell Biology of Lipids. 2016;1861(8):952-61.

171.   Alpy F, Rousseau A, Schwab Y, Legueux F, Stoll I, Wendling C, et al. STARD3 or STARD3NL and VAP form a novel molecular tether between late endosomes and the ER. J Cell Sci. 2013;126(23):5500-12.

172.   Stoica R, De Vos KJ, Paillusson S, Mueller S, Sancho RM, Lau K-F, et al. ER–mitochondria associations are regulated by the VAPB–PTPIP51 interaction and are disrupted by ALS/FTD-associated TDP-43. Nature communications. 2014;5:3996.

173.   Schuldiner M, Zalckvar E. Incredibly close—A newly identified peroxisome–ER contact site in humans. The Journal of Cell Biology. 2017;216(2):287-9.

174.   Ferdinandusse S, Falkenberg KD, Koster J, Mooyer PA, Jones R, van Roermund CW, et al. ACBD5 deficiency causes a defect in peroxisomal very long-chain fatty acid metabolism. Journal of medical genetics. 2017;54(5):330-7.

175.   F. P, J. ME, F. RC, S. S, G. A, A. OB, et al. A mutation in the acyl-coenzyme A binding domain-containing protein 5 gene (ACBD5) identified in autosomal dominant thrombocytopenia. Journal of Thrombosis and Haemostasis. 2010;8(9):2085-7.

176.   Faergeman NJ, Knudsen J. Role of long-chain fatty acyl-CoA esters in the regulation of metabolism and in cell signalling. Biochemical Journal. 1997;323(1):1-12.

177.   Kragelund BB, Knudsen J, Poulsen FM. Acyl-coenzyme A binding protein (ACBP). Biochimica et Biophysica Acta (BBA)-Molecular and Cell Biology of Lipids. 1999;1441(2):150-61.

178.   Soupene E, Serikov V, Kuypers FA. Characterization of an acyl-coenzyme A binding protein predominantly expressed in human primitive progenitor cells. Journal of lipid research. 2008;49(5):1103-12.

179.   Nazarko TY, Ozeki K, Till A, Ramakrishnan G, Lotfi P, Yan M, et al. Peroxisomal Atg37 binds Atg30 or palmitoyl-CoA to regulate phagophore formation during pexophagy. J Cell Biol. 2014;204(4):541-57.

180.   Islinger M, Lüers GH, Li KW, Loos M, Völkl A. Rat Liver Peroxisomes after Fibrate Treatment A SURVEY USING QUANTITATIVE MASS SPECTROMETRY. Journal of Biological Chemistry. 2007;282(32):23055-69.

181.   Wiese S, Gronemeyer T, Ofman R, Kunze M, Grou CP, Almeida JA, et al. Proteomics characterization of mouse kidney peroxisomes by tandem mass spectrometry and protein correlation profiling. Molecular & Cellular Proteomics. 2007;6(12):2045-57.

182.   Delille HK, Guimaraes SC, Borta H, Lüers GH, Fransen M, Schrader M. Pex11pβ-mediated growth and division of mammalian peroxisomes follows a maturation pathway. J Cell Sci. 2010;123(16):2750-62.

183.   Oeljeklaus S, Schummer A, Mastalski T, Platta HW, Warscheid B. Regulation of peroxisome dynamics by phosphorylation. Biochimica et Biophysica Acta (BBA) - Molecular Cell Research. 2016;1863(5):1027-37.

184.   Abu-Safieh L, Alrashed M, Anazi S, Alkuraya H, Khan AO, Al-Owain M, et al. Autozygome-guided exome sequencing in retinal dystrophy patients reveals pathogenetic mutations and novel candidate disease genes. Genome research. 2012:gr. 144105.112.

185.   Yagita Y, Shinohara K, Abe Y, Nakagawa K, Al-Owain M, Alkuraya FS, et al. Deficiency of a Retinal Dystrophy Protein, Acyl-CoA Binding Domain-containing 5 (ACBD5), Impairs Peroxisomal beta-Oxidation of Very-long-chain Fatty Acids. The Journal of biological chemistry. 2017;292(2):691-705.

186.   Costello JL, Castro IG, Hacker C, Schrader TA, Metz J, Zeuschner D, et al. ACBD5 and VAPB mediate membrane associations between peroxisomes and the ER. J Cell Biol. 2017:jcb. 201607055.

187.   Olenych SG, Claxton NS, Ottenberg GK, Davidson MW. The fluorescent protein color palette. Current protocols in cell biology. 2007;36(1):21.5. 1-.5. 34.

188.   Kaech S, Banker G. Culturing hippocampal neurons. Nature Protocols. 2006;1:2406.

189.   Cho D-H, Kim YS, Jo DS, Choe S-K, Jo E-K. Pexophagy: Molecular Mechanisms and Implications for Health and Diseases. Molecules and Cells. 2018;41(1):55-64.

190.   Sun M, Bernard LP, Dibona VL, Wu Q, Zhang H. Calcium phosphate transfection of primary hippocampal neurons. Journal of visualized experiments: JoVE. 2013(81).

191.   Frangi AF, Niessen WJ, Vincken KL, Viergever MA, editors. Multiscale vessel enhancement filtering. International Conference on Medical Image Computing and Computer-Assisted Intervention; 1998: Springer.

192.   Canny J. A computational approach to edge detection. IEEE Transactions on pattern analysis and machine intelligence. 1986(6):679-98.

193.   Lindeberg T. Scale-space theory: A basic tool for analyzing structures at different scales. Journal of applied statistics. 1994;21(1-2):225-70.

194.   Sánchez-Ponce D, DeFelipe J, Garrido JJ, Muñoz A. In vitro maturation of the cisternal organelle in the hippocampal neuron's axon initial segment. Molecular and Cellular Neuroscience. 2011;48(1):104-16.

195.   Schrader M, Godinho LF, Costello JL, Islinger M. The different facets of organelle interplay-an overview of organelle interactions. Frontiers in cell and developmental biology. 2015;3:56.

196.   Stefan CJ, Trimble WS, Grinstein S, Drin G, Reinisch K, De Camilli P, et al. Membrane dynamics and organelle biogenesis—lipid pipelines and vesicular carriers. BMC Biology. 2017;15:102.

197.   Valm AM, Cohen S, Legant WR, Melunis J, Hershberg U, Wait E, et al. Applying systems-level spectral imaging and analysis to reveal the organelle interactome. Nature. 2017;546(7656):162.

198.   Eisenberg-Bord M, Shai N, Schuldiner M, Bohnert M. A tether is a tether is a tether: tethering at membrane contact sites. Developmental cell. 2016;39(4):395-409.

199.   Jourdain I, Sontam D, Johnson C, Dillies C, Hyams JS. Dynamin-dependent biogenesis, cell cycle regulation and mitochondrial association of peroxisomes in fission yeast. Traffic (Copenhagen, Denmark). 2008;9(3):353-65.

200.   Pelkey KA, Chittajallu R, Craig MT, Tricoire L, Wester JC, McBain CJ. Hippocampal GABAergic inhibitory interneurons. Physiological reviews. 2017;97(4):1619-747.

201.   Lewis DA. The chandelier neuron in schizophrenia. Developmental neurobiology. 2011;71(1):118-27.

202.   Viney TJ, Lasztoczi B, Katona L, Crump MG, Tukker JJ, Klausberger T, et al. Network state-dependent inhibition of identified hippocampal CA3 axo-axonic cells in vivo. Nature neuroscience. 2013;16(12):1802.

203.   Bähner F, Weiss EK, Birke G, Maier N, Schmitz D, Rudolph U, et al. Cellular correlate of assembly formation in oscillating hippocampal networks in vitro. Proceedings of the National Academy of Sciences. 2011;108(35):E607-E16.

204.   Wefelmeyer W, Cattaert D, Burrone J. Activity-dependent mismatch between axo-axonic synapses and the axon initial segment controls neuronal output. Proceedings of the National Academy of Sciences of the United States of America. 2015;112(31):9757-62.

205.   Hamada MS, Goethals S, de Vries SI, Brette R, Kole MHP. Covariation of axon initial segment location and dendritic tree normalizes the somatic action potential. Proceedings of the National Academy of Sciences. 2016.

206.   Kriebel M, Metzger J, Trinks S, Chugh D, Harvey RJ, Harvey K, et al. The Cell Adhesion Molecule Neurofascin Stabilizes Axo-axonic GABAergic Terminals at the Axon Initial Segment. Journal of Biological Chemistry. 2011;286(27):24385-93.

207.   Jedlicka P, Vlachos A, Schwarzacher SW, Deller T. A role for the spine apparatus in LTP and spatial learning. Behavioural brain research. 2008;192(1):12-9.

208.   Schlüter A, Del Turco D, Deller T, Gutzmann A, Schultz C, Engelhardt M. Structural Plasticity of Synaptopodin in the Axon Initial Segment during Visual Cortex Development. Cerebral Cortex. 2017;27(9):4662-75.

209.   Chand AN, Galliano E. A distinct subtype of dopaminergic interneuron displays inverted structural plasticity at the axon initial segment. 2015;35(4):1573-90.

210.   Wada F, Nakata A, Tatsu Y, Ooashi N, Fukuda T, Nabetani T, et al. Myosin Va and Endoplasmic Reticulum Calcium Channel Complex Regulates Membrane Export during Axon Guidance. Cell Reports. 2016;15(6):1329-44.

211.   Gurel Pinar S, Hatch Anna L, Higgs Henry N. Connecting the Cytoskeleton to the Endoplasmic Reticulum and Golgi. Current Biology. 2014;24(14):R660-R72.

212.   Csordás G, Weaver D, Hajnóczky G. Endoplasmic Reticular–Mitochondrial Contactology: Structure and Signaling Functions. Trends in Cell Biology. 2018.

213.   Horner SM, Wilkins C, Badil S, Iskarpatyoti J, Gale M, Jr. Proteomic analysis of mitochondrial-associated ER membranes (MAM) during RNA virus infection reveals dynamic changes in protein and organelle trafficking. PLoS One. 2015;10(3):e0117963.

214.   Castro IG, Richards DM, Metz J. A role for Mitochondrial Rho GTPase 1 (MIRO1) in motility and membrane dynamics of peroxisomes. 2018;19(3):229-42.

215.   Kuijpers M, Yu KL, Teuling E, Akhmanova A, Jaarsma D, Hoogenraad CC. The ALS8 protein VAPB interacts with the ER–Golgi recycling protein YIF1A and regulates membrane delivery into dendrites. The EMBO journal. 2013;32(14):2056-72.

216.   Schrader M, Costello J, Godinho LF, Islinger M. Peroxisome-mitochondria interplay and disease. Journal of inherited metabolic disease. 2015;38(4):681-702.

217.   Lin C, Schuster M, Guimaraes SC, Ashwin P, Schrader M, Metz J, et al. Active diffusion and microtubule-based transport oppose myosin forces to position organelles in cells. Nature communications. 2016;7:11814.

218.   Woolfson DN, Bartlett GJ, Bruning M, Thomson AR. New currency for old rope: from coiled-coil assemblies to α-helical barrels. Current opinion in structural biology. 2012;22(4):432-41.

219.   Teuling E, Ahmed S, Haasdijk E, Demmers J, Steinmetz MO, Akhmanova A, et al. Motor neuron disease-associated mutant vesicle-associated membrane protein-associated protein (VAP) B recruits wild-type VAPs into endoplasmic reticulum-derived tubular aggregates. Journal of Neuroscience. 2007;27(36):9801-15.

220.   Villén J, Beausoleil SA, Gerber SA, Gygi SP. Large-scale phosphorylation analysis of mouse liver. Proceedings of the National Academy of Sciences. 2007;104(5):1488-93.

221.   Huttlin EL, Jedrychowski MP, Elias JE, Goswami T, Rad R, Beausoleil SA, et al. A tissue-specific atlas of mouse protein phosphorylation and expression. Cell. 2010;143(7):1174-89.

222.   Diano S, Liu ZW, Jeong JK, Dietrich MO, Ruan HB, Kim E, et al. Peroxisome proliferation-associated control of reactive oxygen species sets melanocortin tone and feeding in diet-induced obesity. Nature medicine. 2011;17(9):1121-7.

10 APPENDIX

10. 1. Equipment

Fume hood·········EN14175, LABORA GmbH

Water bath·········SMB20, Medingen

Thermo Mixer·········comfort, 50 ml, Eppendorf

pH meter·········PB-11, Sartorius

Cell culture hood·········KS12, Thermo Electron Corp.

Centrifugation·········centrigue 5804, Eppendorf

Vortexer·········Vortex GENIE, Scientific Industries

Cell culture Incubator ·········HERA Cell150, Thermo Scientific

Sterilizer ········· Rotilabo®-Syringe filter, CME, Sterile, pore size 0.22µm, Ø outer 33mm, Roth

Dissection equipment sets·········FST by DUMONT, SWITZERLAND

Cryostat·········HM550, Microm

Microscopes

Dissecting microscope·········OPTICA

Phase contrast microscope amounted with fluorescence lamp········· Nikon ECLIPSE TS100

Confocal laser scanning microscopes

Nikon C1plus (Nikon Instruments Europe, Düsseldorf, Germany)

Laser lines: 488 nm, 548 nm, 642 nm

Objectives: Nikon Plan Apo VC 20×/0.75 NA, Nikon Plan Apo VC 60×/1.4 NA oil; Nikon Plan Apo VC 100×/1.45 NA oil

Leica SP5 MP (Leica Microsystems CMS GmbH, Mannheim, Germany)

Laser lines: Ar-Laser; DPSS; HeNe

Objectives: 5x/0.15 NA; 10x/0.30 NA; 20x/0.7 NA; 25x/0.95 NA water; 40x/1,3 NA oil; 63x/1,1 NA glycerol

10. 2. Softwares

Fiji········ ImageJ, written by J. Rietdorf and A. Seitz; v2.0.0-rc-61/1.51n/Java1.8.0_66, 64 bit

AutoQuant X3® model and Imaris® software········v9.2, Bitplane, USA

SigmaPlot········v12.3, Systat Software Inc.

Adobe Photoshop CS4········Adobe System, Adobe Inc.

Endnote® X7········Thompson Reuters, New York, USA

10. 3. Chemicals and other consumables

HCl········37%, Art-Nr. 7476.2, Carl Roth GmbH

Ethanol········≥99.5%, Art-Nr. 5054.3, Roth

Isoflurane········CDS019936, Aldrich

PEI········ Polyethyleniminie, branched, 408727, Sigma

Neurobasal Media········Neurobasal™ Medium, 21103049, Gibco

B27········B27™ Supplement (50×), serum free, Gibco

Pen/Strep········P0781, Sigma

Glutamax········GlutaMax™ Supplement, 350500038, Glibo

Papain········PAP, Worthington Biochemical Corporation

Horse serum·········16050122, Gibco™

BSA·········P06-1395500, PAN™ BIOTECH

Trypan blue·········T8154, Sigma

$CaCl_2$ ·········A3652.0500, Applichem

NaCl ·········278, Baker Analyzed

KCl ·········67811, Merck

Glucose ·········G8270-100g, Sigma

HEPES·········A1069.0500, Applichem

Triton® ×100·········3051.4, Roth

Embedding media for Immunofluorescence staining ·········Roti®-Mount FluorCare, Roth

Embedding media for slicing frozen tissue·········Tissue Tek® O.C.T. Compound, SAKURA FINETEK USA INC.

1.5 # coverslips ········· CS-12R15, Warner Instruments, LLC

24-well plate·········REF 83.3920, SARSTEDT

Ø35mm image chamber········· μ-Dish ^{35mm} Grid-500, ibidi®

40 μm cell strainer ·········REF352340, BD Falcon

10. 4. Self-written codes with macro language in ImageJ

10. 4. 1. Measurement of cisternal organelle in the AIS

```
macro "SP-counting in AIS"{

//make sure each z-stack saved in individual folders

targetfolder = getDirectory("Choose a Directory");
```

```
general_targetfolder = getDirectory("Choose another Directory to save for data
collection");

open("");

stackname = getTitle();

//green, red, blue channels are assigned to Image 1, 2, 3.

run("Split Channels");

selectImage(1);

stacknameG = getTitle();

run("8-bit");

selectImage(2);

stacknameR = getTitle();

run("8-bit");

selectImage(3);

stacknameB = getTitle();

run("8-bit");

// generate AIS area from red channel.

selectWindow(stacknameR);

run("Z Project...", "projection=[Max Intensity]");

MIP_R = getTitle();

// image pre-processing

selectWindow(MIP_R);

run("Enhance Contrast...", "saturated=0.4");
```

```
run("Despeckle");

setTool("polyline");

//creat AIS line selection

waitForUser("Please draw a line along axon initial segment");

roiManager("Add");

//Straighten AIS area

selectWindow(MIP_R);

roiManager("Select", 0);

run("Straighten...", "line=80 process");

run("Enhance Contrast...", "saturated=0.4");

//Thresholding with "Huang" for area outline

setAutoThreshold("Huang dark");

waitForUser("Confirm the thresholding value");

run("Convert to Mask");

setTool("oval");

waitForUser("Please clear out irrelevent signal from red channel");

run("Convert to Mask");

Straighten_AIS = getTitle();

//AIS area defining

selectWindow(Straighten_AIS);

run("Create Selection");

roiManager("Add");
```

```
roiManager("Select", 1);

//measure AIS area

run("Set Measurements...", "area bounding limit redirect=None decimal=3");

run("Measure");

waitForUser("Entry the AIS para. into exl.");

//close windows no longer in use.

selectWindow("Results");

saveAs("Results", targetfolder + stackname + "_AISarea.xls");

run("Close");

selectWindow(Straighten_AIS);

saveAs("jpeg", targetfolder + "Straighten_AIS.jpg" );

close();

selectWindow(MIP_R);

saveAs("jpeg", targetfolder + "MIP in red channel.jpg" );

close();

// generate synpo area from green channel.

selectWindow(stacknameG);

run("Z Project...", "projection=[Max Intensity]");

MIP_G = getTitle();

 //image pre-processing

selectWindow(MIP_G);

//run("Brightness/Contrast...");
```

```
//waitForUser("Adjust brightness/contrast");

setAutoThreshold("Otsu dark");

waitForUser("Confirm the thresholding value");

run("Convert to Mask");

run("Watershed");

//Straightening sp area

roiManager("Select", 0);

run("Straighten...", "line=80 process");

Straighten_SP = getTitle();

selectWindow(Straighten_SP);

//sp punctae in AIS selection for particle analyzing

//setAutoThreshold("Otsu dark");

//run("Convert to Mask");

//run("Watershed");

run("Make Binary");

setTool("oval");

waitForUser("Please remove irrelevent particles from green channel");

run("Make Binary");

run("Set Measurements...", "area limit redirect=None decimal=3");

run("Analyze Particles...", "size=0.01-Infinity show=[Bare Outlines] display exclude
clear include summarize in_situ");

waitForUser("Entry the SP para. into exl");
```

```
selectWindow("Summary");

saveAs("text", general_targetfolder + stackname + "_Summary.xls");

run("Close");

if (nResults > 0 ) {

selectWindow("Results");

saveAs("Results", targetfolder + "Results_SP.xls");

run("Close");

}

selectWindow(Straighten_SP);

saveAs("jpeg", targetfolder + "Straighten_SP.jpg" );

close();

selectWindow(MIP_G);

saveAs("jpeg", targetfolder + "MIP in green channel.jpg" );

close();

selectWindow(stacknameG);

close();

selectWindow(stacknameR);

close();

selectWindow(stacknameB);

close();

roiManager("Save", targetfolder +"ROI.zip");

roiManager("reset");
```

10. 4. 2. Measurement of PO distribution in neurons

```
macro "PO-counting in neuron"{

//make sure each z-stack saved in single folder

open("", "color_mode=Grayscale quiet rois_import=[ROI manager] split_channels
        view=Hyperstack stack_order=XYCZT");

targetfolder = getDirectory("Choose a Directory");

//green, red, blue channels are assigned to Image 1, 2, 3.

selectImage(1);

stacknameG = getTitle();

run("8-bit");

selectImage(3);

stacknameB = getTitle();

run("8-bit");

selectImage(2);

stacknameR = getTitle();

run("8-bit");

// generate soma and neurits area from red channel.

//run("3D Viewer");

//call("ij3d.ImageJ3DViewer.setCoordinateSystem", "false");

//call("ij3d.ImageJ3DViewer.add", stacknameR, "None", stacknameR, "0", "true",
        "false", "false", "2", "0");

selectWindow(stacknameR);
```

```
run("Brightness/Contrast...");

waitForUser("Adjust brightness for a better structure view");

run("Despeckle", "stack");

run("3D Viewer");

call("ij3d.ImageJ3DViewer.setCoordinateSystem", "false");

call("ij3d.ImageJ3DViewer.add", stacknameR, "None", stacknameR, "0", "true",
        "false", "false", "2", "0");

selectWindow(stacknameR);

run("Z Project...", "projection=[Max Intensity]");

MIP_R = getTitle();

run("Duplicate...", " ");

MIP_dup = getTitle();

selectWindow(MIP_R);

setTool("polygon");

waitForUser("Please select soma area with reference of 3d viewer");

roiManager("Add");

run("Threshold...");

setThreshold(50, 255);

setOption("BlackBackground", true);

run("Convert to Mask");

run("Dilate");

setTool("polygon");
```

```
waitForUser("Please clear out irrelevent signal from red channel");

run("Convert to Mask");

run("Create Selection");

roiManager("Add");

selectWindow(MIP_dup);

saveAs("jpeg", targetfolder + "MIP in red channel binary.jpg" );

close();

selectWindow(MIP_R);

saveAs("jpeg", targetfolder + "MIP in red channel.jpg" );

close();

call("ij3d.ImageJ3DViewer.close");

selectWindow("B&C");

run("Close");

// analysis peros in green channel.

//soma area first.

selectWindow(stacknameG);

roiManager("Select", 0);

run("Duplicate...", "duplicate");

GsomaDuplicate = getTitle();

setBackgroundColor(0, 0, 0);

run("Clear Outside", "stack");

run("Z Project...", "projection=[Max Intensity]");
```

```
GsomaMIP = getTitle();

run("Subtract Background...", "rolling=5");

run("Enhance Contrast...", "saturated=0.4");

run("Despeckle");

setAutoThreshold("Default dark");

run("Convert to Mask");

run("Watershed");

run("Set Measurements...", "area mean standard min perimeter limit display
        redirect=[GsomaMIP] decimal=3");

run("Analyze Particles...", "size=0.03-10 show=[Bare Outlines] display exclude clear
        include summarize in_situ");

selectWindow(GsomaMIP);

saveAs("jpeg", targetfolder + "Gsoma_choosen_peros_outlines.jpg" );

close();

selectWindow(GsomaDuplicate);

close();

selectWindow("Results");

saveAs("Results", targetfolder + "GsomaResults.xls");

selectWindow("Results");

run("Close");

selectWindow("Threshold");

run("Close");
```

```
//then neurits area.

selectWindow(stacknameG);

roiManager("Select", 1);

run("Duplicate...", "duplicate");

GneuritsDulicate = getTitle();

selectWindow(GneuritsDulicate);

roiManager("Select", 0);

run("Clear", "stack");

roiManager("Select", 1);

setBackgroundColor(0, 0, 0);

run("Clear Outside", "stack");

run("Z Project...", "projection=[Max Intensity]");

MIP_Gneurits = getTitle();

run("Subtract Background...", "rolling=5");

run("Enhance Contrast...", "saturated=0.4");

run("Despeckle");

setAutoThreshold("Default dark");

run("Convert to Mask");

run("Watershed");

run("Set Measurements...", "area mean standard min perimeter limit display
        redirect=[MIP_Gneurits] decimal=3");
```

```
run("Analyze Particles...", "size=0.03-10 show=[Bare Outlines] display exclude clear
        include summarize in_situ");

selectWindow(MIP_Gneurits);

saveAs("jpeg", targetfolder + "Gneurits_choosen_peros_outlines.jpg" );

close();

selectWindow("Results");

saveAs("Results", targetfolder + "GneuritsResults.xls");

run("Close");

//finish analysis in green channel, close windows.

selectWindow(GneuritsDulicate);

close();

//start analyzing peros in blue channels.

selectWindow(stacknameB);

setTool("polygon");

waitForUser("Please clear out irrelevent signal from the image before
        measurement");

selectWindow(stacknameB);

roiManager("Select", 0);

run("Duplicate...", "duplicate");

BsomaDuplicate = getTitle();

setBackgroundColor(0, 0, 0);

run("Clear Outside", "stack");
```

```
run("Z Project...", "projection=[Max Intensity]");

BsomaMIP = getTitle();

run("Subtract Background...", "rolling=5");

run("Enhance Contrast...", "saturated=0.4");

run("Despeckle");

setAutoThreshold("Default dark");

run("Convert to Mask");

run("Watershed");

run("Set Measurements...", "area mean standard min perimeter limit display
        redirect=[BsomaMIP] decimal=3");

run("Analyze Particles...", "size=0.03-10 show=[Bare Outlines] display exclude clear
        include summarize in_situ");

selectWindow(BsomaMIP);

saveAs("jpeg", targetfolder + "Bsoma_choosen_peros_outlines.jpg" );

close();

selectWindow(BsomaDuplicate);

close();

selectWindow("Results");

saveAs("Results", targetfolder + "BsomaResults.xls");

selectWindow("Results");

run("Close");

//Then neurits area in blue channel.
```

```
selectWindow(stacknameB);

roiManager("Select", 1);

run("Duplicate...", "duplicate");

BneuritsDulicate = getTitle();

selectWindow(BneuritsDulicate);

roiManager("Select", 0);

run("Clear", "stack");

roiManager("Select", 1);

setBackgroundColor(0, 0, 0);

run("Clear Outside", "stack");

run("Z Project...", "projection=[Max Intensity]");

MIP_Bneurits = getTitle();

run("Subtract Background...", "rolling=5");

run("Enhance Contrast...", "saturated=0.4");

run("Despeckle");

setAutoThreshold("Default dark");

run("Convert to Mask");

run("Watershed");

run("Set Measurements...", "area mean standard min perimeter limit display
        redirect=[MIP_Bneurits] decimal=3");

run("Analyze Particles...", "size=0.03-10 show=[Bare Outlines] display exclude clear
        include summarize in_situ");
```

```
selectWindow(MIP_Bneurits);

saveAs("jpeg", targetfolder + "Bneurits_choosen_peros_outlines.jpg" );

close();

selectWindow("Results");

saveAs("Results", targetfolder + "BneuritsResults.xls");

run("Close");

//finish analysis in blue channel, close windows.

selectWindow(BneuritsDulicate);

close();

//analysis completed, close all windows, save summary in another folder.

roiManager("Save", targetfolder +"ROI.zip");

roiManager("reset");

general_targetfolder = getDirectory("Choose another Directory to save summary");

selectWindow("Summary");

saveAs("text", general_targetfolder + stacknameR + "_Summary.xls");

run("Close");

selectWindow(stacknameG);

close();

selectWindow(stacknameR);

close();

selectWindow(stacknameB);

close(); }
```

CURRICULUM VITAE

Personal Information

Name: Yunhong

Family name: Wang

Date of birth: May 11th, 1988

Nationality: China

Address: Pettenkofer str.19, 68169, Mannheim, Germany

Education

Since 09/2014   Doctoral student at Medical Faculty Mannheim, Heidelberg University

09/2012 – 08/2013   Master student at Medical Faculty Mannheim, Heidelberg University, Master of Science in Medical Physics

09/2009 – 06/2012   Master student at Anhui Medical University, Hefei, China, Master of Science in Neurobiology

09/2004 – 06/2009   Bachelor student at Anhui Medical University, Hefei, China, Bachelor of Medicine in Clinical Medicine

ACKNOWLEDGEMENT